NASA Contractor Report 4635

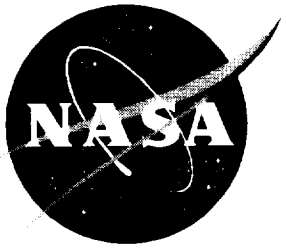

Transonic Navier-Stokes Calculations About a 65° Delta Wing

W. Kelly Londenberg
ViGYAN, Inc. • Hampton, Virginia

National Aeronautics and Space Administration
Langley Research Center • Hampton, Virginia 23681-0001

Prepared for Langley Research Center
under Contract NAS1-18585

November 1994

This publication is available from the following sources:

NASA Center for AeroSpace Information
800 Elkridge Landing Road
Linthicum Heights, MD 21090-2934
(301) 621-0390

National Technical Information Service (NTIS)
5285 Port Royal Road
Springfield, VA 22161-2171
(703) 487-4650

Transonic Navier-Stokes Calculations About A 65° Delta Wing

W. Kelly Londenberg
ViGYAN, Inc.

Summary

A computational study has been conducted in which the CFL3D Navier-Stokes solver coupled with an algebraic and an one-equation nonequilibrium turbulence model has been used to predict the flow over a 65° delta wing at transonic conditions for Reynolds numbers ranging from 6×10^6 to 120×10^6 based on mean aerodynamic chord. Solutions obtained indicated that the computational method when used with the one-equation turbulence model predicts results that compare well with experiment for attached flow conditions. Comparisons with experimental pressures at separated conditions show that the computational method, even though primary flowfield features are predicted well, does not predict secondary flow features.

Introduction

The flow over low-aspect ratio wings exhibit some very interesting flow features. The flow around the forebody, strake and highly swept leading-edges of fighter aircraft such as the F-18[1] and the F-106B[2] separates at moderate to high angles-of-attack. The resulting free shear layer rolls up in a spiral fashion to form the leading-edge vortex. Locally high velocities are induced by the vortex in the flow field that in turn creates a low pressure region near the vehicle surface. This suction peak located on the wing surface under the vortex core results in additional lift that is known as "vortex lift". Vortices from the forebody, strake and the wing leading-edge create a very complex flow field for fighter type configurations while for a sharp edge delta wing planform only a single primary vortex forms. However, this flow field is not as simple as it may seem. An adverse lateral pressure gradient exists outboard of the minimum pressure region created by the primary vortex. This gradient results in a secondary separation creating another vortex, weaker than the primary, turning in the opposite sense of the first. When the secondary vortex is relatively strong (high angles-of-attack), an adverse lateral pressure gradient now exists inboard of the secondary

vortex resulting in a third separation and a tertiary vortex. (Hoeijmakers gives an excellent overview of the related physics of vortical flowfields in references 3 and 4.)

Aerodynamic benefits can be obtained from vortical flow when the wing vortex is somewhat controlled[5,6,7,8]. In the applications presented in these references, a vortex is induced by fixing the separation point along the sharp leading-edge of a leading-edge flap or "vortex flap". The vortex forms on this flap resulting in a beneficial force vector that can be resolved into thrust and lift components. A naturally occurring, uncontrolled, vortex may result in adverse effects due to asymmetric separation along the forebody, strake or wing leading-edge[9]. These effects can cause buffet or a loss of stability and control, and depend on how early or late the flow separates. Flow separation around a rounded leading-edge is a flow phenomenon that is very dependent on Reynolds number and, since boundary layer transitional data is not a linear function of Reynolds number, this information can not be accurately predicted by standard (low Reynolds number) wind tunnel testing. The capability to accurately predict this separation is gaining significance in the design of some current configurations such as the High Speed Civil Transport (HSCT) which will consist of a highly swept wing with a round leading-edge.

Numerous experimental as well as numerical studies have been conducted to gain an understanding of this flow field. Quite a few of these studies have been done using a delta wing planform since, as stated above, this simple geometric shape can produce the desired complex vortical flow field. (See references 10 and 11 for experimental work and references 12 - 26 for computational studies.) The experimental studies were all conducted at sub-scale Reynolds number conditions so the numerical studies concentrated on geometries with sharp leading-edges. These studies, most either Euler or laminar Navier-Stokes solutions, predicted the primary vortex trajectory and strength well while not capturing the secondary vortex. This is expected since correctly capturing the secondary vortex depends upon capturing the secondary separation, a viscous phenomenon, while for a sharp leading-edge the primary vortex forms as a result of the geometrical discontinuity at the wing leading-edge. A few researchers have conducted numerical studies on rounded leading-edge geometries. Hsu and Liu[24] and Hsu, Hartwich and Liu[25] showed computations that compared well with experiment for laminar, incompressible conditions. Rizzi and Purcell[13] and Muller and Rizzi[14] showed laminar Navier-Stokes solutions that compared well with experiment for predic-

tion of the primary vortex at transonic conditions but failed to completely capture the secondary vortex. Hilgenstock[12] and Hilgenstock and Vollmers[21] made fully turbulent Navier-Stokes calculations using an algebraic turbulence model at transonic and moderately low Reynolds number. Their prediction of the primary vortex compared well with experiment while the secondary separation was not predicted.

Recently an experimental investigation of the flow over a 65° delta wing was conducted in the National Transonic Facility (NTF) at the NASA Langley Research Center[27]. Pressure data is available from this wind tunnel test at transonic conditions for Reynolds number of up 120 million, based on mean aerodynamic chord. This data was obtained for a variety of leading-edge radii ranging from sharp to fairly blunt. This test was conducted to establish a high Reynolds number database so that the effect of leading-edge shape on leading-edge flow separation could be analyzed both numerically and experimentally.

This paper will document a study in which the CFL3D Navier-Stokes code[28] was evaluated for the prediction of the flow over the NTF delta wing with a medium and a round radius leading-edge. These calculations were made for low to high Reynolds number at transonic conditions

Symbols

b	span
c	chord
C_p	pressure coefficient
M	freestream Mach number
NASA	National Aeronautics and Space Administration
Rn	Reynolds number (based on mean aerodynamic chord)
i	grid coordinate in the axial direction
j	grid coordinate in the span-wise direction
k	grid coordinate in the normal direction
x	axial dimension, inches
y	span-wise dimension, inches

z	normal dimension, inches
y^+	law-of-the-wall coordinate
α	angle of attack, degrees
Λ	sweep angle, degrees

Subscripts:

LE	Leading-edge
MAC	Mean Aerodynamic Chord
r	root
w	wing
∞	denotes conditions at infinity

Experimental Study

An experimental investigation was conducted in the National Transonic Facility (NTF) at the NASA Langley Research Center in which pressure coefficients were obtained for a delta wing model with a series of leading-edge radii. The NTF delta wing model is an analytically defined flat plate delta wing with a leading-edge sweep of 65°, 12 inch semi-span and 25.734 inch root chord (figure 1). This model was designed such that the leading-edge portion could be interchanged. Data was obtained for four leading-edge shapes in this test. These shapes varied from sharp to blunt and are analytically defined. Figure 2 shows the relative radii of the four leading-edge shapes. Data were obtained for each leading-edge radius for Reynolds number of 6×10^6 to 120×10^6, based on mean aerodynamic chord at freestream Mach numbers of 0.40 to 0.90. All experimental data was obtained at free-transition conditions. Angle-of-attack ranged from 0° to 26°. The wind tunnel test data is reported in Reference 27.

For the present study, analyses were preformed for the wing with the medium and round leading-edge radius. The leading-edge shape is defined by

$$z = a\sqrt{x} + bx + cx^2 + dx^3 \quad (1)$$

where $a = 0.34897572$, $b = 0.29224873$, $c = -0.28382228$, and $d = 0.06227092$ for the medium radius leading-edge and $a = 0.4935262$, $b = 0.08004809$, $c = -0.19719469$, and $d = 0.04632388$ for the round leading-edge radius. The radius for each of these leading-edges non-dimensionalized by the mean aerodynamic chord is 0.15% and 0.30% for the medium and round leading-edges, respectively. The trailing-edge closure can also be defined analytically by

$$z = bx + cx^2 + dx^3 \quad (2)$$

where $b = 0.510024$, $c = -0.19819009$, and $d = 0.02567154$ and is the same for each of the leading-edge shapes. The sting cover faring is defined by

$$z = a\sqrt{x} + bx + cx^2 + dx^3 \quad (3)$$

where $a = 0.30946082$, $b = 0.33279823$, $c = -0.04163681$, and $d = 0.00150729$

Computational Method

The computational method used in this study is the CFL3D, version three, Navier-Stokes code[28]. This code, developed at NASA Langley, solves the thin-layer approximations to the three-dimensional, time-dependent, compressible Navier-Stokes equations. A second-order accurate upwind-biased spatial differencing scheme is utilized for solving these equations. Convergence acceleration is obtained using the full approximation scheme multigrid algorithm and Roe's flux-difference splitting scheme to determine fluxes on cell faces. The Baldwin-Lomax algebraic turbulence model[29] and the Spalart-Allmaras one-equation turbulence model[30] were used to solve for the turbulent viscosity and are incorporated into the laminar Navier-Stokes equations. The details of the numerical method as well as of each turbulence model are presented in the respective references.

Grid Generation

The grid generated about the delta wing geometry was created using the GRIDGEN grid generation package[31]. A nine block grid was created about the experimental geometry including the sting and the sting/wing fairing (see figure 3 for schematic of the block layout). The resulting mesh had nearly 900,000

grid points. Clustering normal to all surfaces was set to $1\times10^{-6}\,c_r$. This spacing was selected to ensure y^+ values at first grid line off the surface of 1, based upon flat plate boundary layer theory, for the $Rn = 120\times10^6$ case. All outer boundaries were set $20c_r$ away from the geometry surfaces. Details of the surface grid as well as a crossflow grid plane are shown in figures 4 and 5. This gird was developed utilizing the arbitrary patching logic in CFL3D as is evident in these figures.

Results

Grid Resolution

The effect of mesh density on the computed pressure coefficients was investigated by analyzing solutions on suscessively coarser grids. Each coarser grid was developed by eliminating every other point in each of the three coordinate directions. The resulting pressure distributions revealed that, while the upper surface results varied, the calculated lower surface pressure coefficients were insensitive to mesh density (figure 6). Proceeding on this information, a new volume grid was developed in which grid points in the streamwise direction were removed from several of the lower surface blocks and were added to the leading-edge block in the radial direction. The number of grid points around the leading-edge was increased from 49 to 73 in an attempt to better resolve the separation line. The total mesh size was kept fairly constant by deleting the grid points from the lower surface. The resulting pressure distribution exhibited in figures 7.a - 7.c shows that refinement of the leading-edge in the radial direction has little effect on the calculations. Since solutions using this grid did not utilize significantly more computer resources while yielding slightly better results it was selected to replace the original baseline grid (see table 1 for a listing of the original and refined grid dimensions). A successive coarsening of this grid yielded solutions that showed the upper surface pressure were not grid converged (figure 8). Refinement of the grid in the streamwise direction in the leading-edge block by doubling the number of grid points in the i direction and refinement of block 1,of block 7, and of block 5 by doubling the number of j grid points in each of these blocks showed little to no effect on the calculated upper surface pressures (figure 9). This tends to indicate that the new baseline grid is grid converged in the radial and streamwise directions (see figure 10 for the convergence histories plotted for each of these grid refinement solutions). Solution analysis shows that

the maximum y^+ value utilizing the new baseline grid at the conditions that this grid resolution study has been made (M = 0.85, α = 16.37°, and $Rn = 6\times10^6$) were not greater than 1.60 with an average of 0.30 and standard deviation of 0.18 indicating that the grid is sufficiently clustered to the surface in the normal direction. (A listing of the maximum and average with the corresponding standard deviation of y^+ for all solutions obtained utilizing this refined grid is presented in table 2.)

Turbulence Model Comparison

Comparisons of pressure coefficient predictions obtained using the Baldwin-Lomax turbulence model with those obtained using the Spalart-Allmaras turbulence model are presented in figures 11.a - 11.c. Pressures predicted by either of the models compared very well with experiment for the attached flow case (α = 7.15°). There is slight if any difference between the predicted pressure coefficients except near the trailing-edge (figure 11.a). Here the solution obtained using the Spalart-Allmaras turbulence model exhibits pressure distributions that more closely follow the experimental pressure distribution. Comparison of predicted pressures using both turbulence models with experiment is nearly as good for the case with slight flow separation at the leading-edge of the wing (α = 12.3°). Pressures obtained using both models show evidence of a delayed leading-edge separation (figure 11.b, x/c_r = 0.20). The location of the experimental primary vortex pressure peak is predicted equally as well using either turbulence model however the primary vortex suction peak is predicted better using the Baldwin-Lomax turbulence model (sixty and eighty per cent root chord). The onset of leading-edge separation is also not predicted for the fully separated case (α = 16.37°) by either of the turbulence models as shown by the prediction of the formation of the pressure suction peak aft of experiment as indicated by the delay in the formation of the computed pressure peak (figure 11.c, x/c_r = 0.20). The solutions obtained using the Spalart-Allmaras turbulence model better predicts the magnitude of the suction peak although the crossflow shock wave (defined by $(\Delta c_p)/(\Delta(y/(b/2))) \geq 8$ outboard of the primary suction peak) evident in the experimental pressures aft of 60% root chord (approximately 65% semi-span) is not predicted. Pressure coefficients predicted with the Baldwin-Lomax turbulence model compared very poorly with experiment at 80% root chord. Investigation of this solution further showed that the pressure coefficients predicted aft of the 80% root chord location were oscillating (figure 12). Since this behavior was only observed with use of the

Baldwin-Lomax turbulence model the Spalart-Allmaras turbulence model was selected for the remainder of this study.

Solution Analysis

Predicted pressure coefficients compared with experiment are shown in figures 11.a - 11.c and in figures 13.a - 15.c for the medium leading-edge geometry and in figures 16.a - 19.c for the round leading-edge geometry. The pressures predicted using the Spalart-Allmaras turbulence model compare well with experiment for the attached flow case (low angles-of-attack) for all Reynolds numbers computed. As angle-of-attack is increased the flow separates near the apex of the wing in the experiment resulting in a pronounced suction peak indicating a leading-edge vortex (e.g., figure 11.b, $x/c_r = 0.40$, $y/(b/2) = 0.80$). The vortex is predicted in the calculations but the location of the formation of the suction peak is predicted aft of the experimental location. A secondary separation is evident in the experimental pressures as indicated by the formation of an additional suction peak outboard of the main suction peak at the highest angle-of-attack analyzed at eighty per cent root chord, eighty per cent semi-span for the medium radius leading-edge geometry (see figures 11.c, 13.c, 14.c and 15.c) and at $x/c_r = 0.60$, $y/(b/2) = 0.80$ for the round radius leading-edge geometry (see figures 16.c, 17.c, 18.c and 19.c). This separation is not predicted using the computational method as shown by the surface streamlines plotted in figures 20.a - 21.d. In these plots, a separation line is indicated by the streamlines coalescing to a line while an attachment line is a line from which the streamlines are flowing out. As can be seen in the streamline plots the computational method is predicting only a single separation and corresponding attachment line.

Experimental pressure distributions show little effect of Reynolds number for both leading-edge shapes, particularly at low angles-of-attack where the flow is attached. The Navier-Stokes code generally predicts the experimental trend of Reynolds number on pressure distributions (figures 22.a - 23.f) with the exception of the $Rn = 48\times10^6$ for the medium leading-edge geometry with $\alpha = 12^\circ$. Here, experiment is showing an attachment line (the increase in pressure inboard of the suction peak) that is much nearer to the leading-edge than for the other Reynolds numbers analyzed (figure 22.c, $x/c_r = 0.40$) as well as a lower suction peak for the $Rn = 48\times10^6$ data (figure 22.c, $x/c_r = 0.60$). The computational method predicts neither flow feature for the $Rn = 48\times10^6$ case (figure 22.d). Further analysis of the experimental data presented in Reference 27 for the medium radius leading-edge geometry reveals that the trend exhibited

in the experimental pressures for α = 12.03° is entirely a Reynolds number effect, an effect that the Navier-Stokes code utilized in this study did not predict (compare figures 22.c and 22.d). Also evident in the experimental pressure distributions for $Rn = 48\times10^6$ is the formation of a dual leading-edge vortex as indicated by the dual pressure peaks of near equal magnitude (figure 21.c, x/c_r = 0.40, $y/(b/2) \geq 0.80$). These pressure peaks are not as prominent in the pressure distributions for $Rn = 6\times10^6$ or $Rn = 84\times10^6$. The dual vortices are not predicted by the computational method. A crossflow shock wave (defined by $(\Delta c_p)/(\Delta(y/(b/2))) \geq 8$ outboard of the primary pressure peak) is evident in the experimental pressures (e.g., figure 16.c, x/c_r = 0.60, $y/(b/2) \approx 0.65$). This flow phenomena is not predicted by the Navier-Stokes code. Lower surface pressure coefficients were predicted very well at all angles-of-attack and Reynolds numbers indicating that the angle-of-attack was correctly modeled in the calculations.

Comparison with data derived from an empirical relationship presented in reference 32 shows that the predicted sweep and angle-of-attack of the vortex core agree very well with experimentally derived values (table 3). Predicted values were obtained by locating the vortex in the flowfield by identifying the minimum total pressure above the boundary layer over the wing at stations along the chord of the wing. Examination of the minimum pressure coefficient at x/c_r = 0.60 in the footpath of the vortex core (figures 24 and 25) shows that the experimental level is generally under-predicted. The experimental trends are not predicted for either of the leading-edge radii analyzed with the predicted data showing very little effect of Reynolds number. (Note that the Reynolds number effect on the medium radius leading-edge for values between $Rn = 6\times10^6$ and $Rn = 84\times10^6$, as discussed above, is again evident in the experimental data (figure 24, α = 12°)).

Concluding Remarks

This study has "indicated" several conclusions regarding the use of Navier-Stokes methods with turbulence modeling to predict the flow over a highly swept wing. Among these is that, at attached flow conditions, the predictions of the Navier-Stokes method employed agree very well with experiment. However, when the flow is fully separated comparisons with experimental data are not as good. This is a result of several factors, individually or combined. The first of these is that the solutions were computed for

fully turbulent flow conditions while experimental data was obtained for free transition conditions. Further complicating matters, this data was obtained in the National Transonic Facility in which there are no means presently available to obtain flow visualization data that could indicate where transition was occurring in the experiment. This lack of experimental information could be offset with the development of some affordable means to calculate transition locations that can be coupled with current Navier-Stokes solvers.

Comparison of experimental data with Navier-Stokes solutions are also degraded due to the computational method not predicting any of the secondary flow features apparent in the experimental pressure distributions. The location of the primary separation and attachment are predicted well although the streamwise location of leading-edge separation is not. The location of the primary vortex suction peak is predicted well thus indicating that the computational method is modeling the overall flowfield physics correctly, which is as expected. The Navier-Stokes code does not predict the secondary flow features such as the dual leading-edge vortices and the crossflow shock wave. These features could be captured in several ways. One of these is through grid enhancement in the region of the vortex. Increasing grid density in this region should allow for better resolution of the vortical flowfield. However, in a design environment these flow features are often not known *a priori*. Therefore for a computational method to be a useful design tool some means of adapting the grid to the vortex is required. Another method by which the vortical flow could be better resolved is through better turbulence modeling techniques. The current nonequilibrium turbulence model utilized in this study predicts primary separation and attachment well as well as lower surface pressures for all cases analyzed. This model has difficulties in predicting secondary flow features for the geometry analyzed.

This study has shown that the CFL3D Navier-Stokes code coupled with the Spalart-Allmaras one-equation nonequilibrium turbulence model can predict the primary flow features of a highly swept wing in a transonic flowfield as well as first order Reynolds number effects. However, absolute pressure distribution levels are not predicted, a consequence of the theory not predicting any of the secondary flow features. With this in mind, this computational method can be used to predict first order effects on the flowfield.

Acknowledgments

This research was sponsored, in part, by the National Aeronautics and Space Administration under Contract NAS1-19672. The author acknowledges the assistance provide by Dr. Chivey Wu of California State University, Los Angeles in the initial grid generation for this project. The assistance provided by Dr. Christopher Rumsey of NASA Langley Research Center, Dr. Robert Biedron of Analytical Services and Material, Inc., and Sherri Krist of ViGYAN, Inc. in the operation of the CFL3D and the associated turbulence models was invaluable. The discussions with and suggestions from Gary Erickson of NASA Langley Research Center and William Milholen,II of North Carolina State University pertaining to interpreting and presenting both the experimental data and computational results were greatly appreciated. Computations were partially preformed on the National Aerodynamic Simulation Facility and this support is gratefully acknowledged.

References

1)Del Frate, John H., Fischer, David F., and Zuniga, Fanny A., "In-Flight Flow Visualization and Pressure Measurements at Low Speeds on the F-18 High Alpha Research Vehicle," AGARD-CP-494, Paper 13, October 1990.

2)Lamar, John E., "In-Flight and Wind Tunnel Leading-Edge Vortex Study On The F-106B Airplane," NASA CP-2416, Vol.1, October 1985, pp. 187-201.

3)Hoeijmakers, H.W.M., "Numerical Simulation Of Vortical Flow," *Von Karman Institute for Fluid Dynamics Introduction to Vortex Dynamics, Volume 2*, May 1986.

4)Hoeijmakers, H.W.M., "Modeling and Numerical Simulation of Vortex Flow in Aerodynamics," AGARD-CP-494, Paper 1, October1990

5)Hallissy, James B., Frink, Neal T., and Huffman, Jarrett K., "Aerodyamic Testing and Analysis of Vortex Flap Configuration For The 5-Percent Scale F-106B," NASA CP-2418, October 1985, pp. 227-248.

6)Finely, Dennis B., and Schoonover, W.Elliott, Jr., "Design and Wind Tunnel Evaluation of Vortex Flaps For The F-16XL," NASA CP-2418, October 1985, pp. 249-276.

7)Schoonover, W. Elliott, JR., and Smith, Frank R., "Design and Wind Tunnel Evaluation of Vortex Flaps For The USAF AFTI/F-111," NASA CP-2418, October 1985, pp. 277-300.

8)Londenberg, William Kelly, "The Effect of Upper Surface Vortex Flap Planform and Deflection on a 60° Delta Wing," Master Thesis, The University of Texas At Arlington, August 1991.

9)Erickson, Gary E., *Wind tunnel Investigation of Vortex Flows on F/A-18 Configuration at Subsonic Through Transonic Speeds*, NASA TP-3111, 1991.

10)Elsenaar, A, and Hoeijmakers, H.W.M., "An Experimental Study of the Flow over a Sharp-Edged Delta Wing at Subsonic and Transonic Speeds," AGARD-CP-494, Paper 15, October 1990.

11)Hirdes, R.H.C.M., "US/European Vortex Flow Experiment Test Report of Wind Tunnel Measurements on the 65 Degree Wing in the NLR Wind Tunnel HST," NLR TR-85046 L, May 1985.

12)Hilgenstock, A., "Validation of Transonic Turbulent Flow Past Delta Wing Configurations," *The Aeronautical Journal*, Vol. 95, Number 947, August/September 1991, pp. 219-230.

13)Rizzi, Arthur, and Purcell, Charles J., "Comparison of Euler and Navier-Stokes Solutions For Vortex Flow Over A Delta Wing," *A Collection of Technical Papers - AIAA 5th Applied Aerodynamics Conference, August 17-19, 1987*, pp. 154-163. (Available as AIAA-87-2347)

14)Muller, B., and Rizzi, A., "Navier-Stokes Computations of Transonic Vortices Over a Round Leading-Edge Delta Wing," AIAA-87-1227, June 1987.

15)Kandil, Osama A, Kandil, Hamdy A., and Liu, C.H., "Shock-Vortex Interaction Over A 65-Degre Delta Wing In Transonic Flow," AIAA-93-2973, July 1993.

16)Hoeijmakers, H.W.M., and van den Berg, J.I., "Application Of an Euler-Equation Method to a Sharp-Edged Delta-Wing Configuration With Vortex Flow," *A Collection of Technical Papers - AIAA 9th Applied Aerodynamics Conference, Volume 2, September 23-25, 1991,* pp. 838-850. (Available as AIAA-91-3310)

17)Williams, B.R., Kordulla, W., Borsi, M., and Hoeijmakers, H.W.M., "Comparison of Solution of Various Euler Solvers and One Navier-Stokes Solver for the FLow about a Sharp-Edged Cropped Delta Wing," AGARD-CP-494, Paper 2, October 1990.

18)Borsi, M., Formaggia, L., Hettena, E., Santillan, S., Selmin, V., and Tarditi, S., "Vortical Flow Simulation by Using Structured and Unstructured Grids," AGARD-CP-494, Paper 3, October 1990.

19)van den Berg, J.I., Hoeijmakers, H.W.M., and Jacobs, J.M.J.W., "Analysis of Results of an Euler-Equation Method Applied to Leading-Edge Vortex Flow," AGARD-CP-494, Paper 4, October 1990.

20)Houtman, E.M., and Bannink, W.J., "Experimental and Numerical Investigation of the Vortex Flow over a Delta Wing at Transonic Speed," AGARD-CP-494, Paper 5, October 1990.

21)Hilgenstock, A., and Vollmers, H., "On the Simulation of Compressible Turbulent Flows Past Delta Wing, Delta Wing-Body, and Delta Wing-Canard," AGARD-CP-494, Paper 7, October 1990.

22)Kaynak, U., Tu, E., Dindar, M., and Barlas, R., "Nonequilibrium Turbulence Modeling Effects on Transonic Vortical Flows about Delta Wings," AGARD-CP-494, Paper 11, October 1990.

23)Ekaterinaris, John A., Coutley, Raymond L., Schiff, Lewis B., and Platzer, Max F., "Numerical Investigation of the Flow Over a Double Delta Wing at High Incidence," AIAA-91-0753, January 1991.

24)Hsu, C.-H., and Liu, C.H., "Navier-Stokes Computation of Flow Around a Round-Edged Double-Delta Wing," *AIAA Journal,* Vol. 28, No. 6, June 1990, pp. 961-968.

25)Hsu, C.-H., Hartwich, P. -M., and Liu, C.H., "Computation of Vortical Interaction for a Sharp-Edged Double-Delta Wing," *Journal of Aircraft,* Vol. 25, No. 5, May 1988, pp. 442-447.

26)Hsu, C.-H., Hartwich, P. -M., and Liu, C.H., "Incompressible Navier-Stokes Computations for a Round-Edged Double-Delta Wing," *Journal of Aircraft,* Vol. 25, No. 8, August 1988, pp. 675-676.

27)Chu, Juilo, and Luckring, James M., "Experimental Surface Pressure Data Obtained on a 65°-Swept Leading-edge Delta Wing over a Reynolds Number and Mach Number Range - Parts I-IV," NASA TM-4645, 1995.

28)Thomas, J.L., Taylor, S.L., and Anderson, W.K., "Navier-Stokes Computations of Vortical Flows Over Low Aspect Ratio Wings," AIAA-87-0207, 1987.

29)Baldwin, B.S., and Lomax, H., "Thin-Layer Approximation and Algebraic Models for Separated Turbulent Flows," AIAA-78-257, 1978.

30)Spalart, P.R., and Allmaras, S.R., "A One-Equation Turbulence Model For Aerodynamic Flows," AIAA-92-0439, 1992.

31)Steinbrenner, John P., Chawner, John R., and Fouts, Chris L., "The GRIDGEN 3D Multiple Block Grid Generator System", WRDC-TR-90-3022 Vols. I and II, July 1990.

32)Erickson, Gary E., "Flow Studies of Slender Wing Vortices," AIAA-80-1423, 1980.

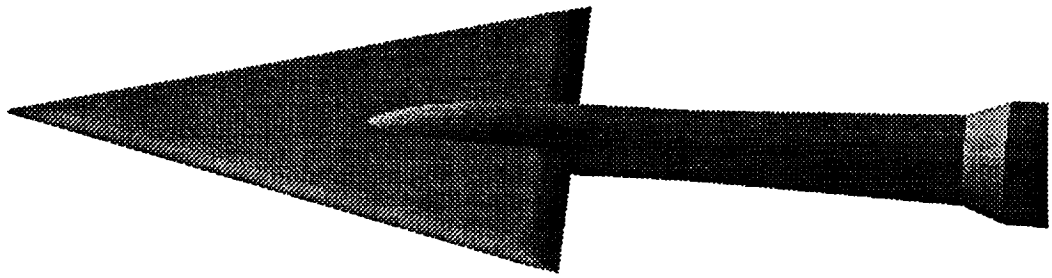

Figure 1. The NTF 65° Delta Wing.

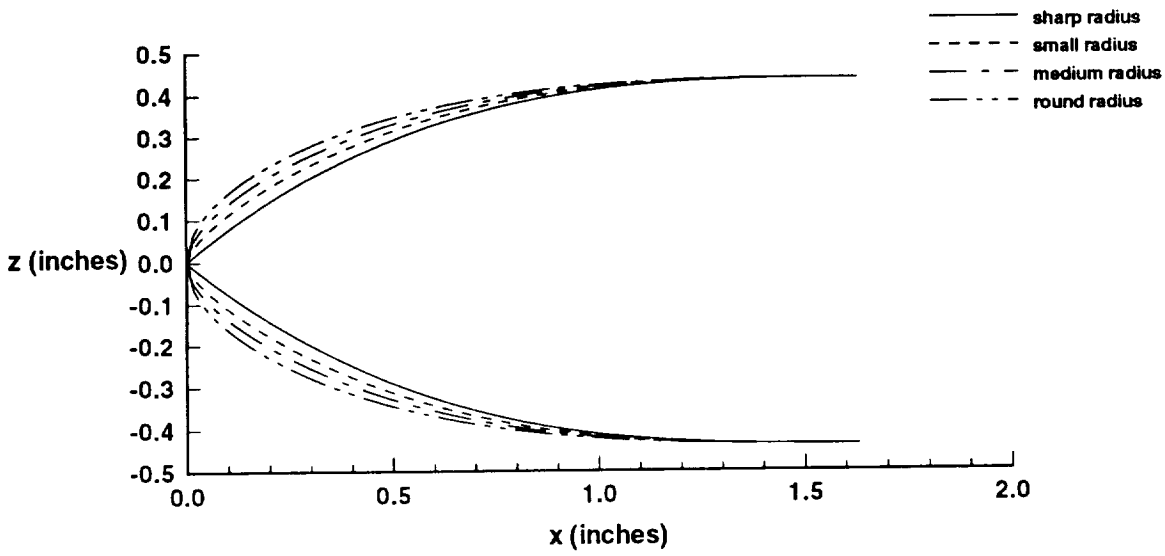

Figure 2. Variation of Leading-Edge Radii.

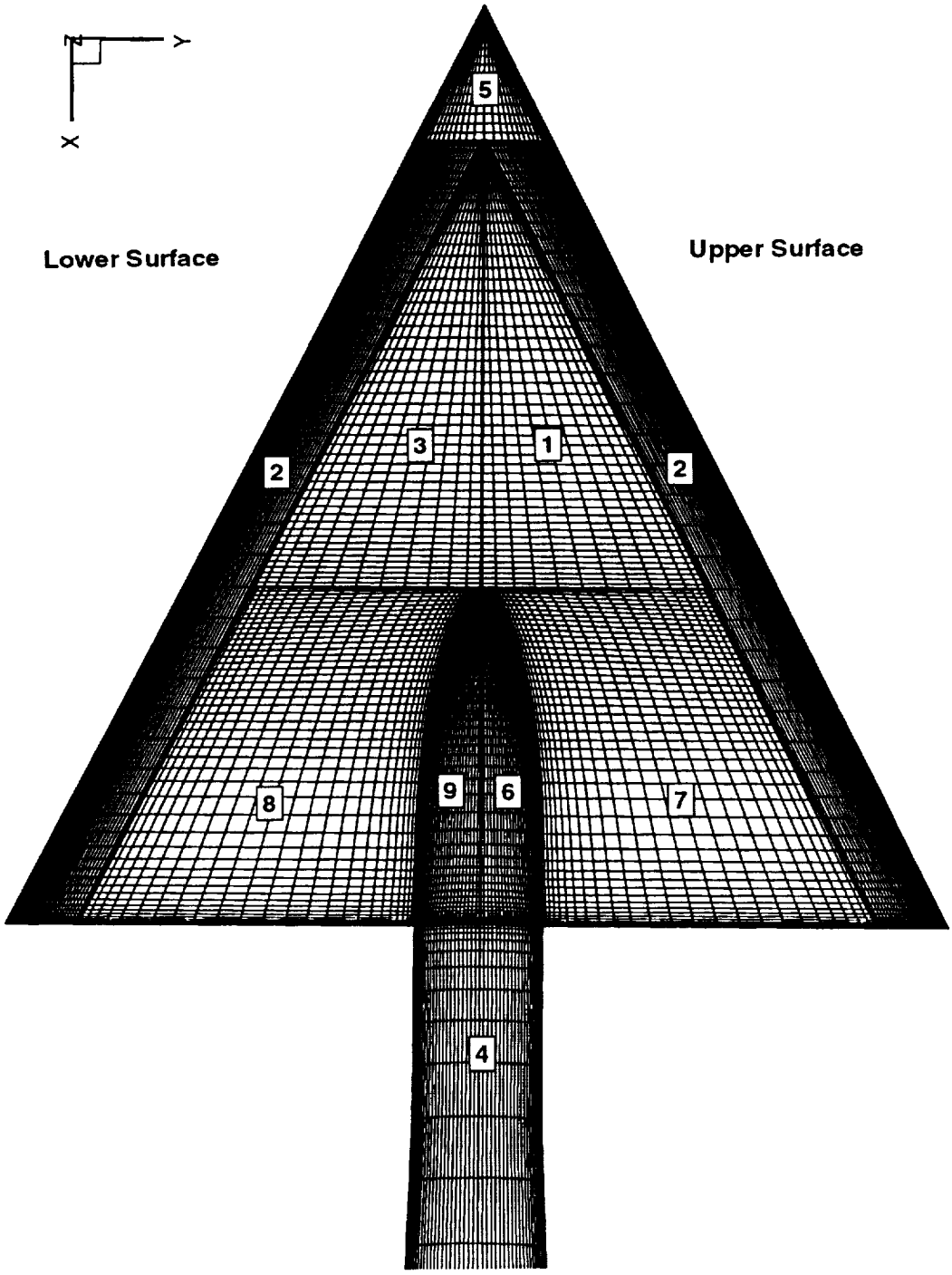

Figure 3. Schematic of block layout.

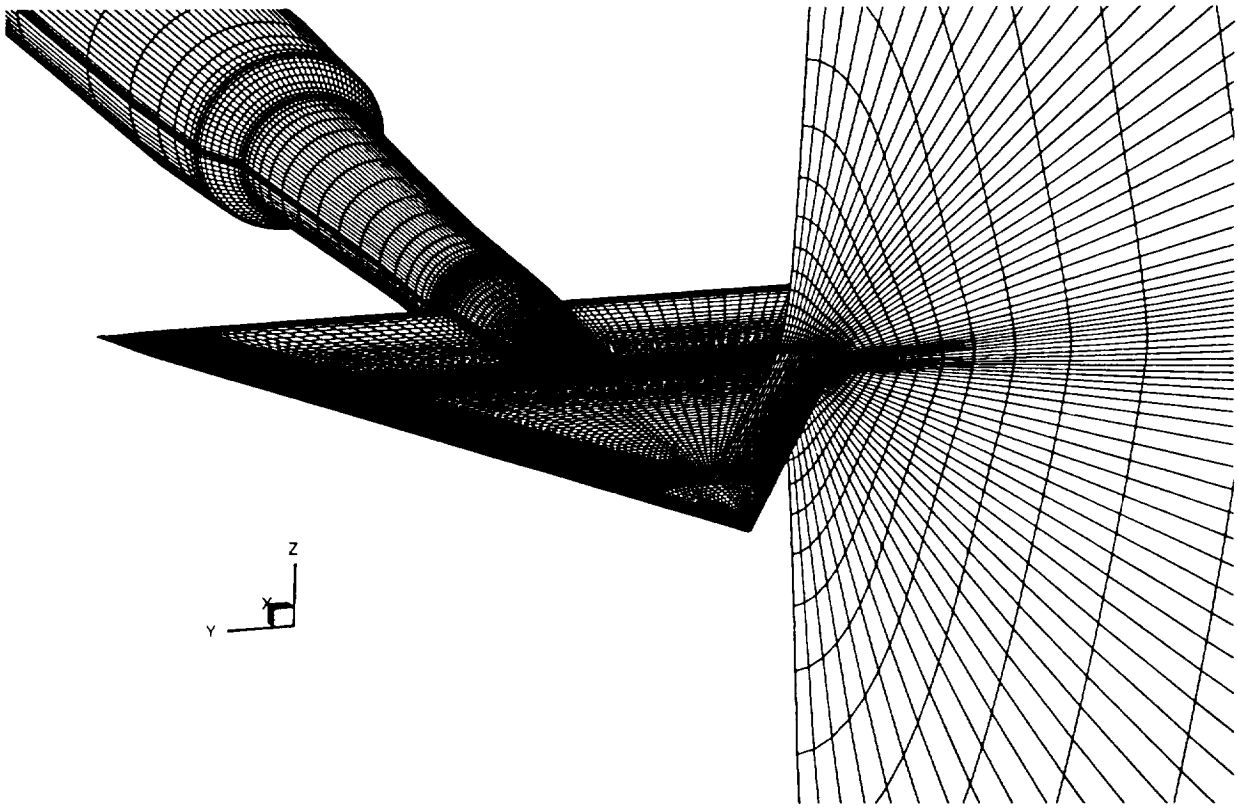

Figure 4. Head-on view of computational grid.

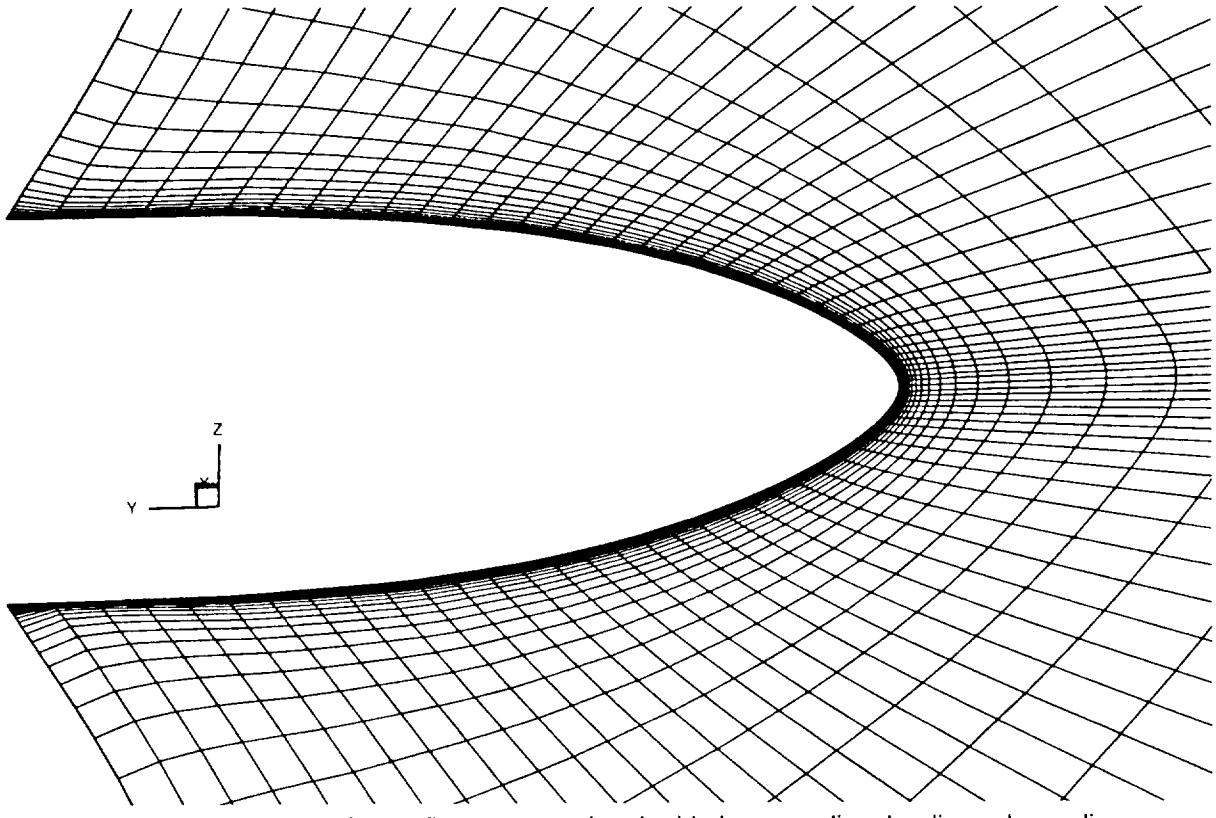

Figure 5. Close-up of crossflow computational grid plane, medium leading-edge radius.

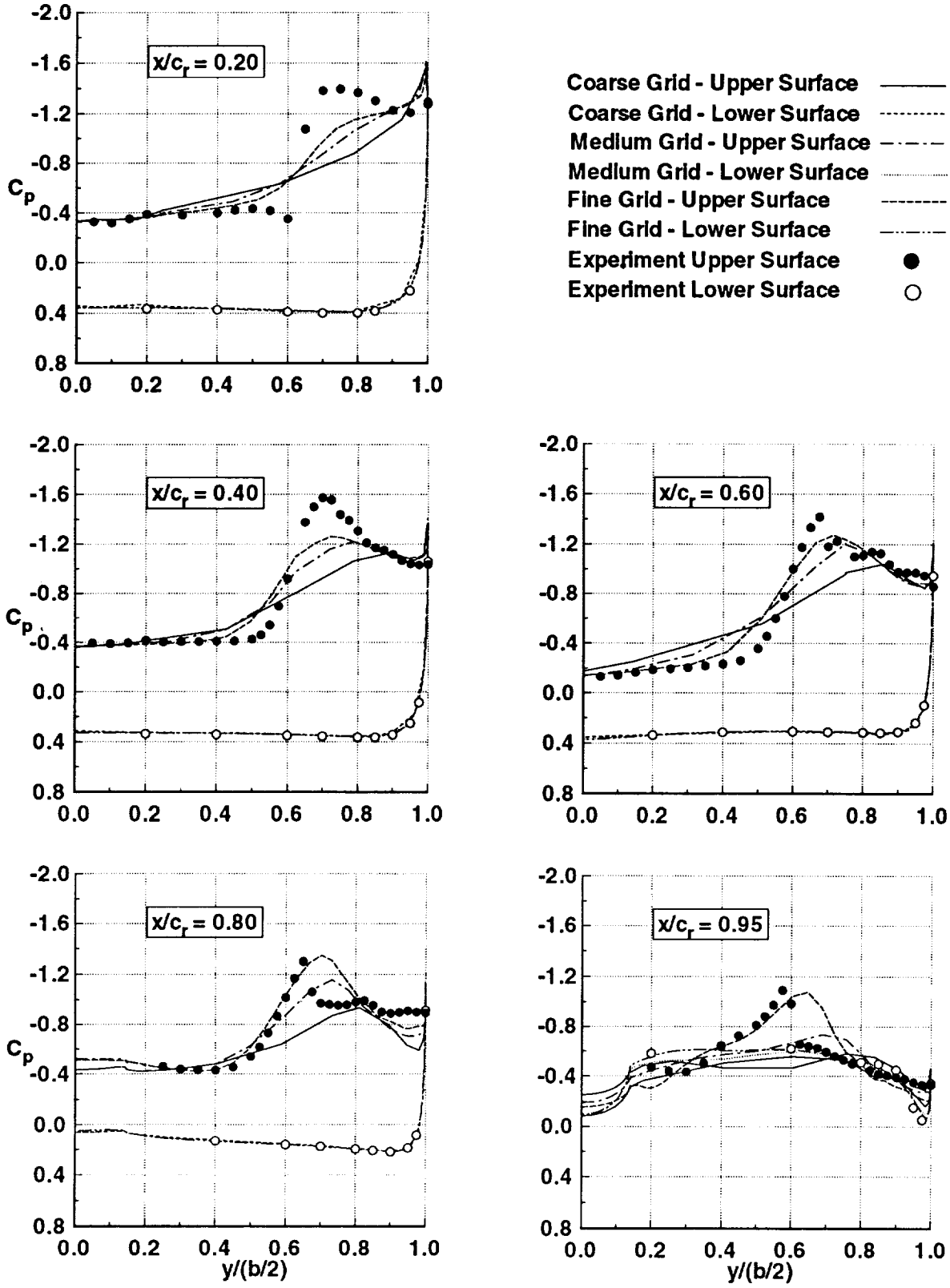

Figure 6. Lower surface pressure coefficients show no dependence on mesh density: Medium leading-edge radius, Spalart-Allmaras turbulence model, $M_\infty = 0.85$, $\alpha = 16.37°$, $Rn = 6 \times 10^6$.

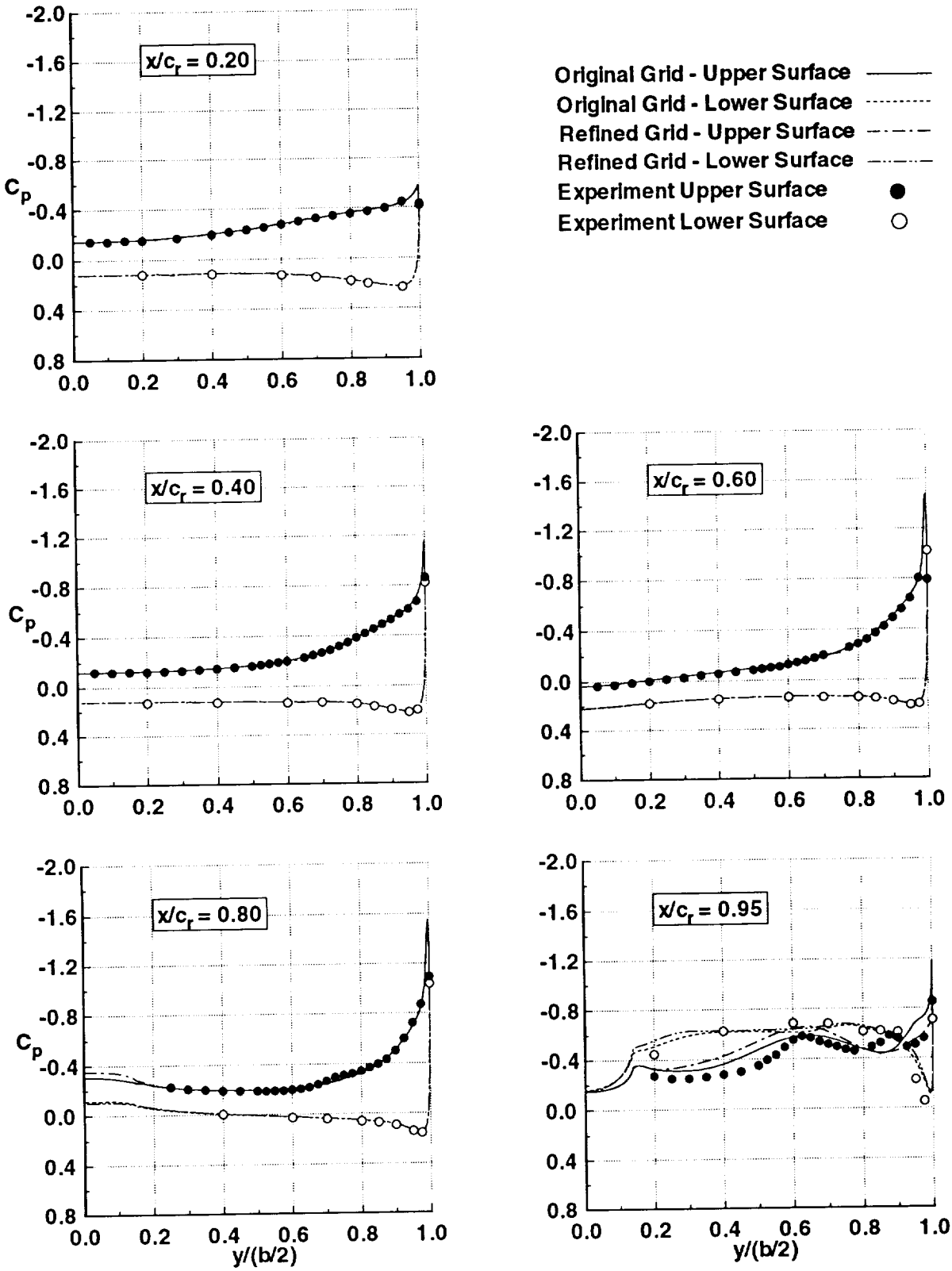

Figure 7.a. Refinement of leading-edge block shows little effect on pressure coefficients: Medium leading-edge radius, Spalart-Allmaras turbulence model, $M_\infty = 0.85$, $\alpha = 7.15^\circ$, $Rn = 6 \times 10^6$.

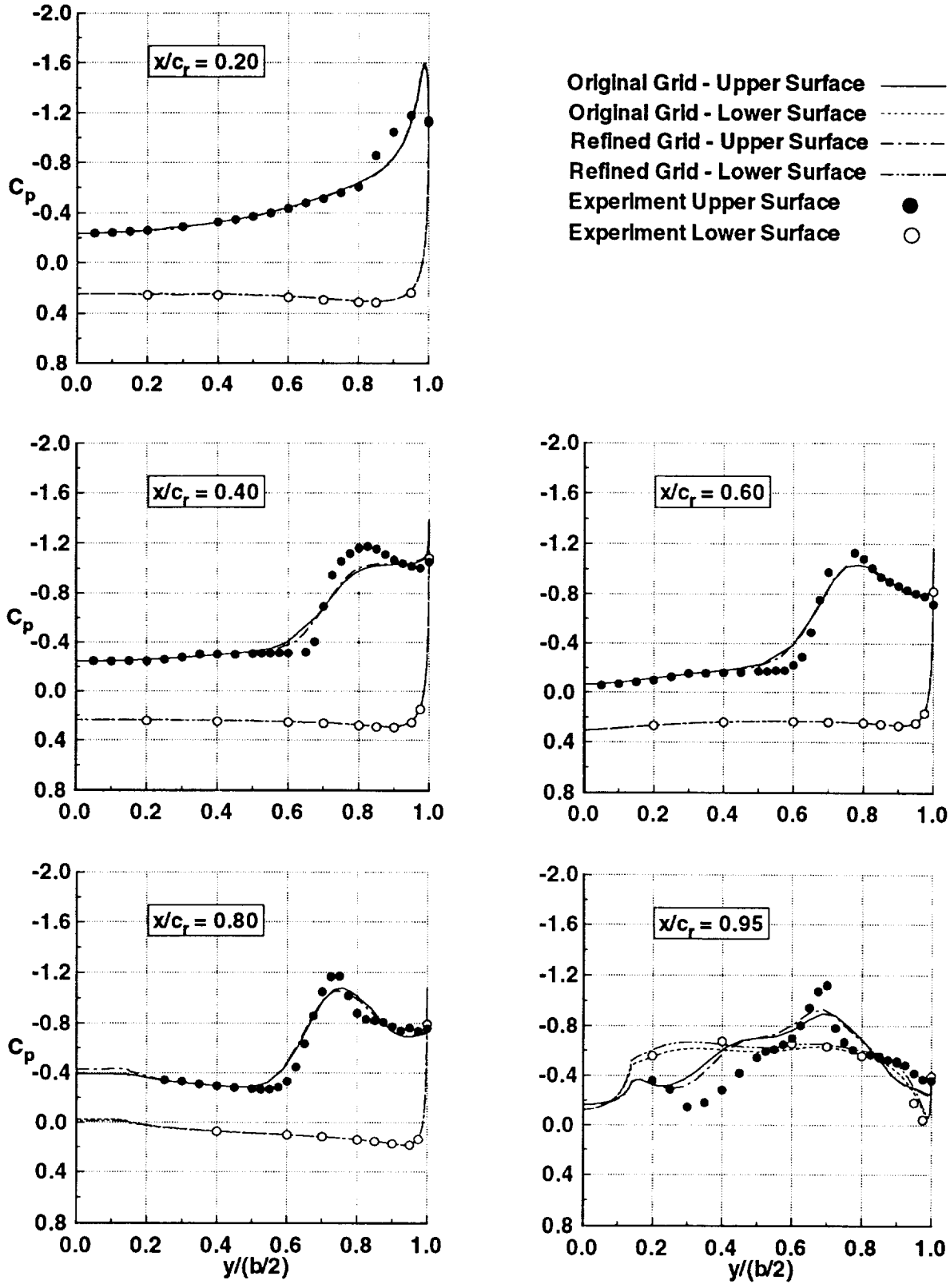

Figure 7.b. Refinement of leading-edge block shows little effect on pressure coefficients: Medium leading-edge radius, Spalart-Allmaras turbulence model, $M_\infty = 0.85$, $\alpha = 12.3^\circ$, $Rn = 6 \times 10^6$.

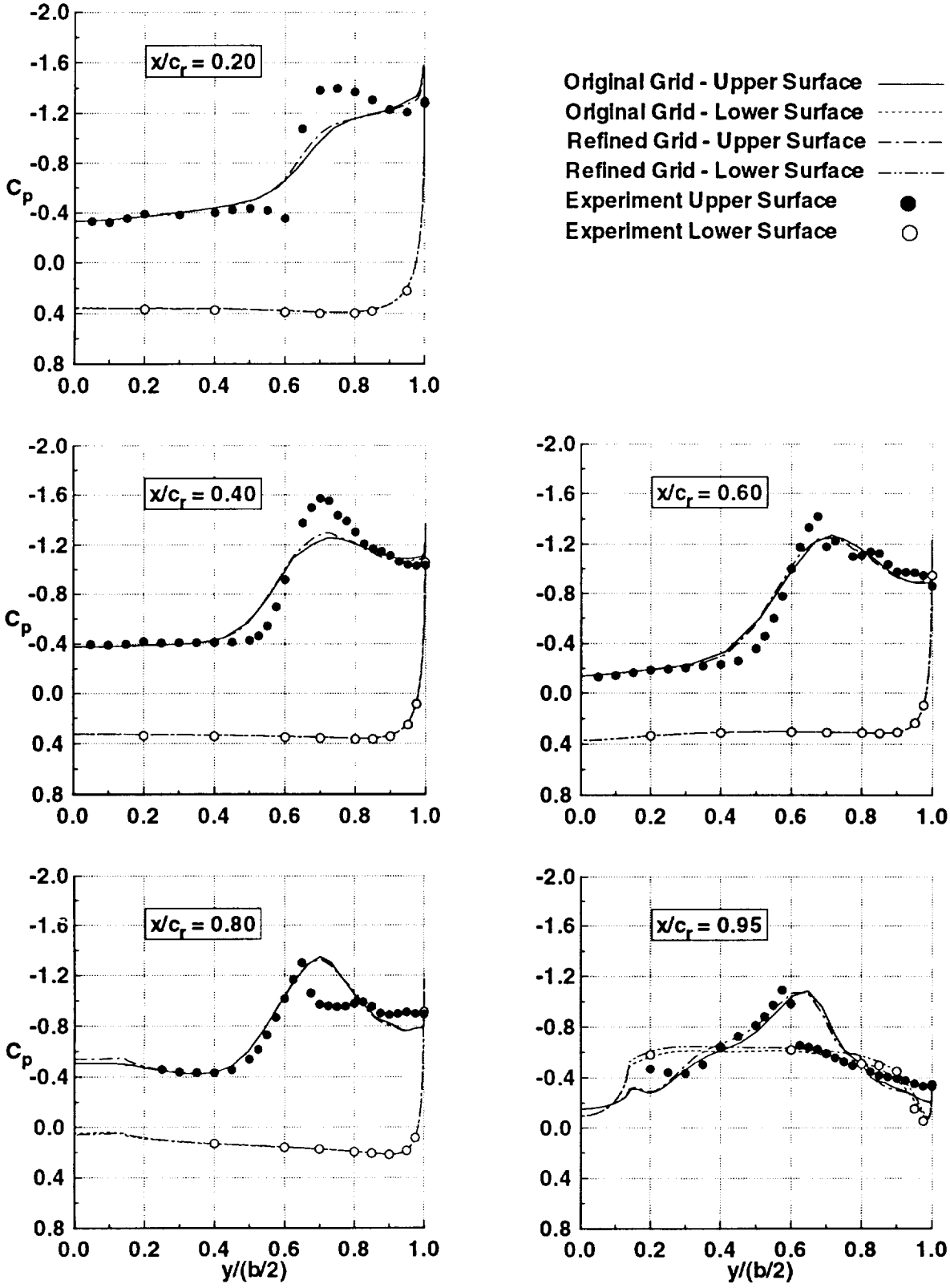

Figure 7.c. Refinement of leading-edge block shows little effect on pressure coefficients: Medium leading-edge radius, Spalart-Allmaras turbulence model, $M_\infty = 0.85$, $\alpha = 16.37^\circ$, $Rn = 6 \times 10^6$.

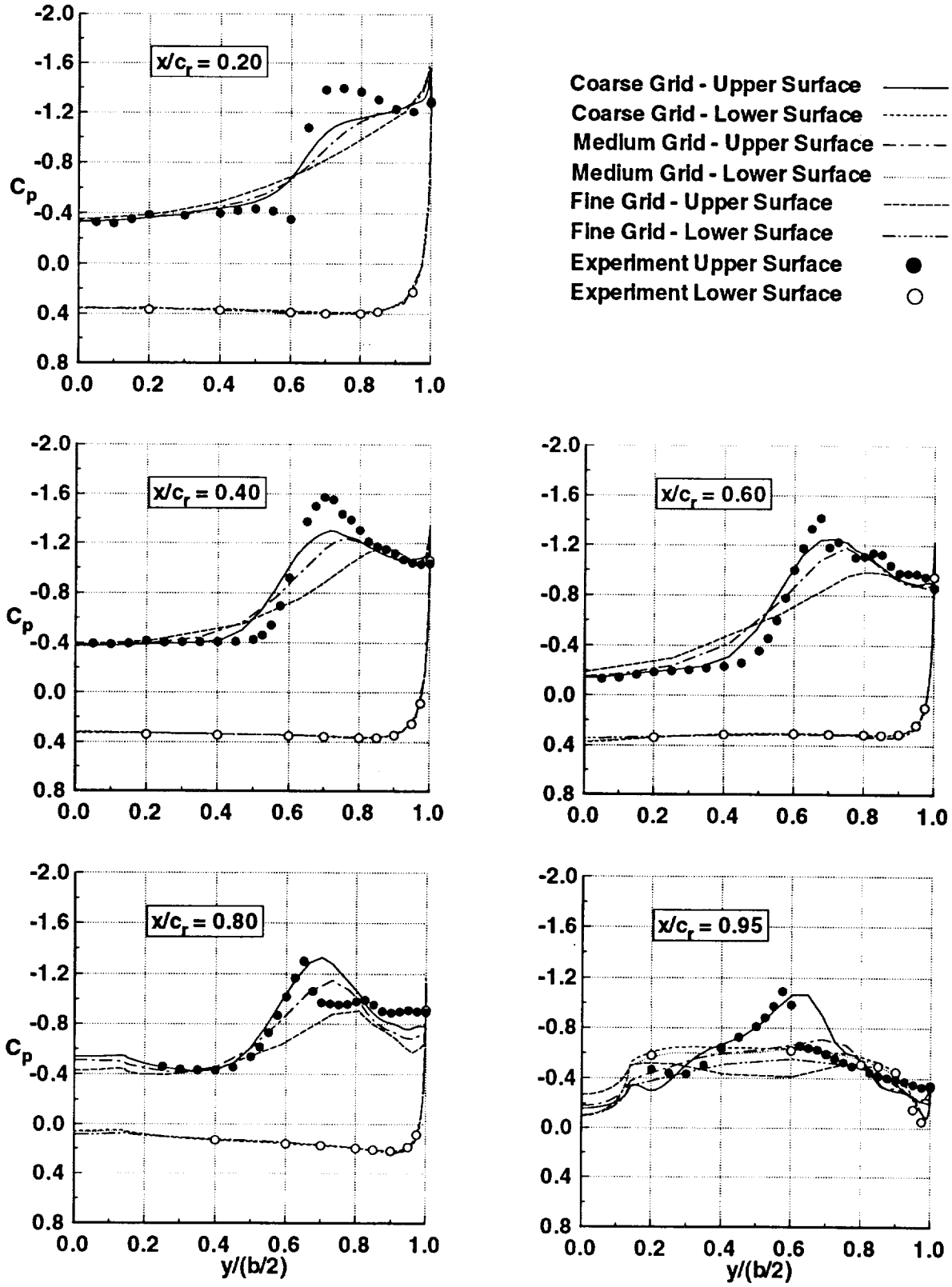

Figure 8. Refined grid upper surface pressures are not grid converged: Medium leading-edge radius, Spalart-Allmaras turbulence model, $M_\infty = 0.85$, $\alpha = 16.37^\circ$, $Rn = 6 \times 10^6$.

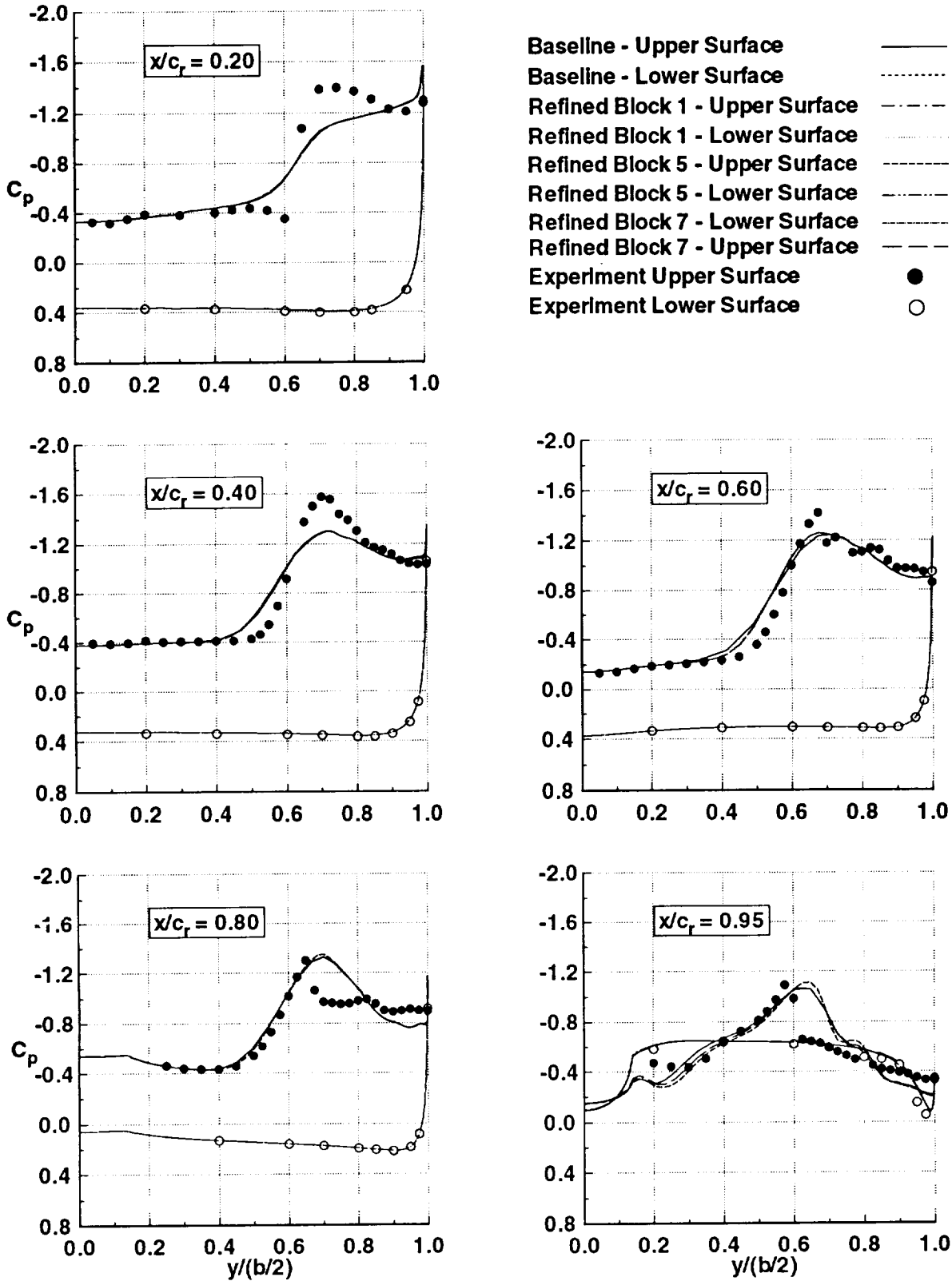

Figure 9. Upper surface pressure distributions show little effect due to upper surface grid refinement: Medium leading-edge radius, Spalart-Allmaras turbulence model, $M_\infty = 0.85$, $\alpha = 16.37^\circ$, $Rn = 6 \times 10^6$.

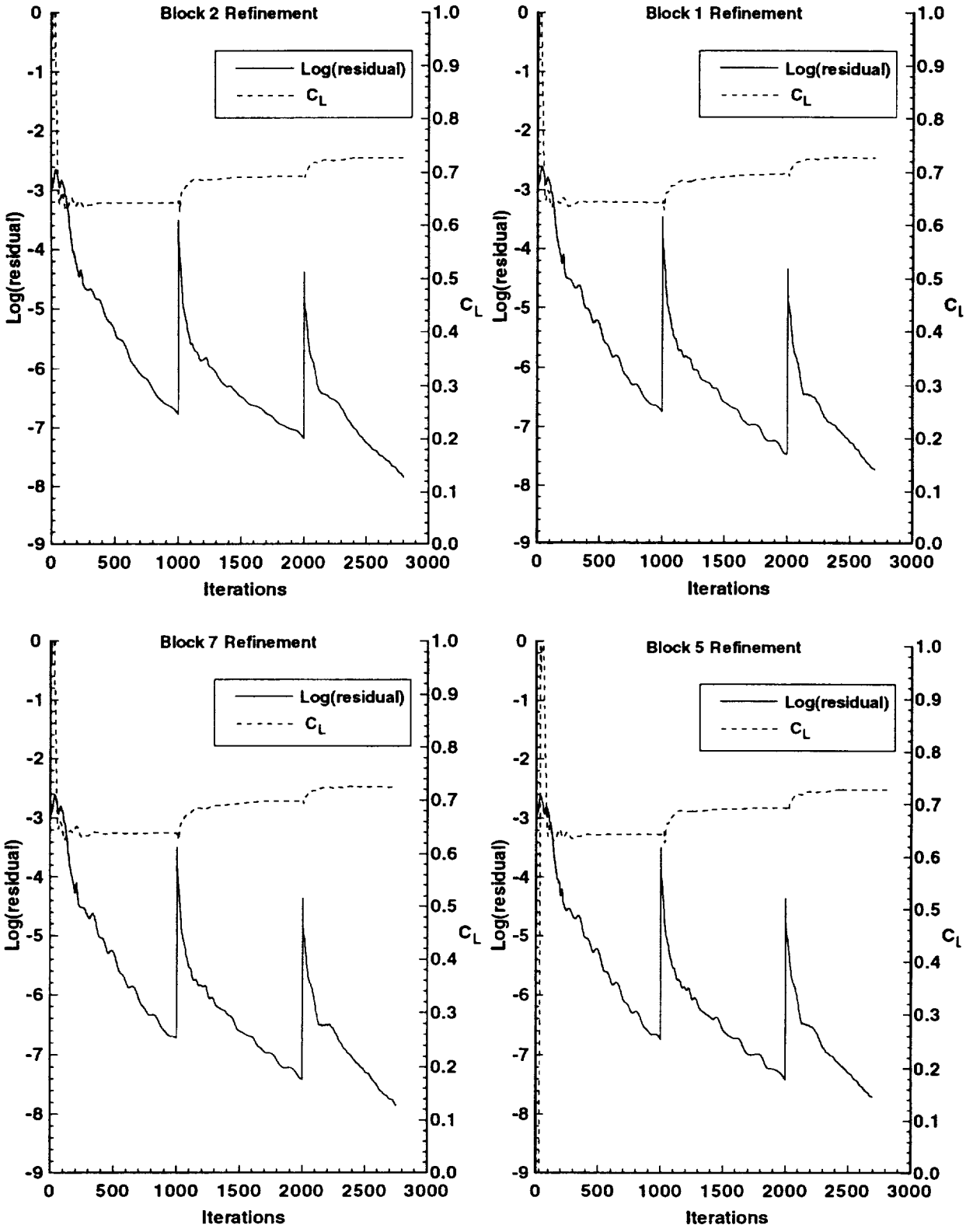

Figure 10. Convergence histories for gird refinement, medium leading-edge radius, Spalart-Allmaras turbulence model, $M_\infty = 0.85$, $\alpha = 16.37^\circ$, $Rn = 6\times10^6$.

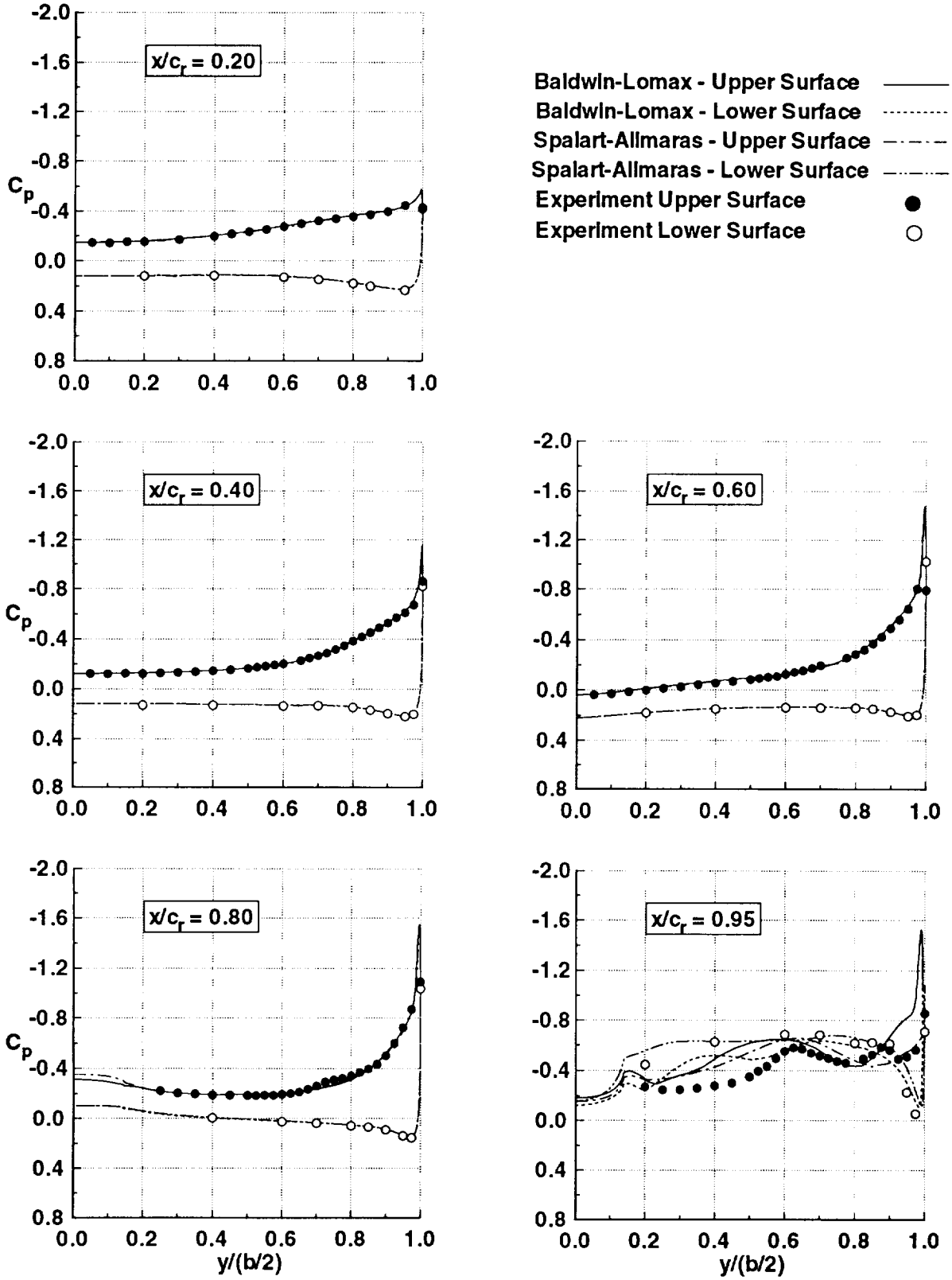

Figure 11.a. Turbulence model comparisons: Medium leading-edge radius, $M_\infty = 0.85$, $\alpha = 7.15^\circ$, $Rn = 6 \times 10^6$.

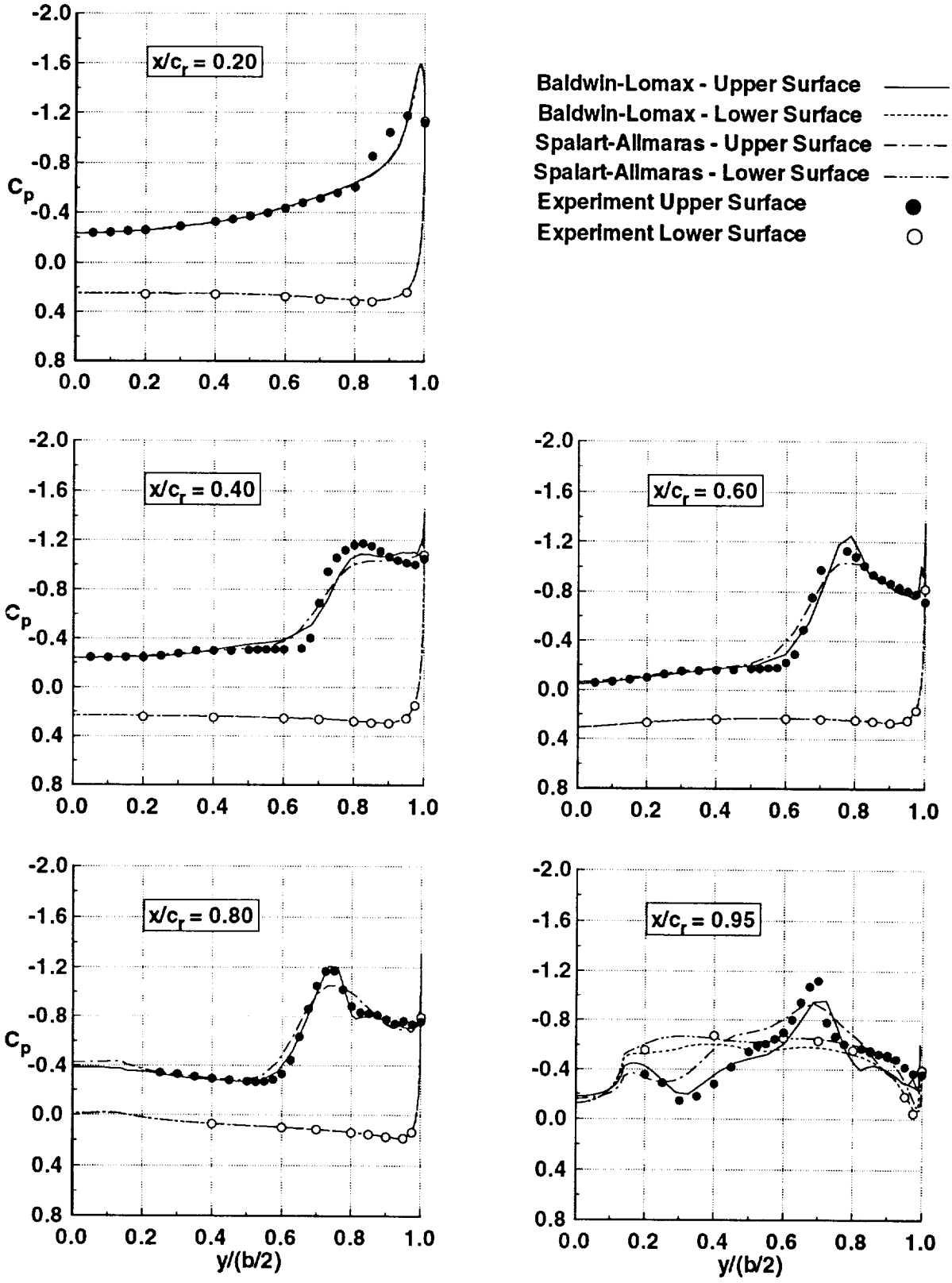

Figure 11.b. Turbulence model comparisons: Medium leading-edge radius, $M_\infty = 0.85$, $\alpha = 12.3^\circ$, $Rn = 6 \times 10^6$.

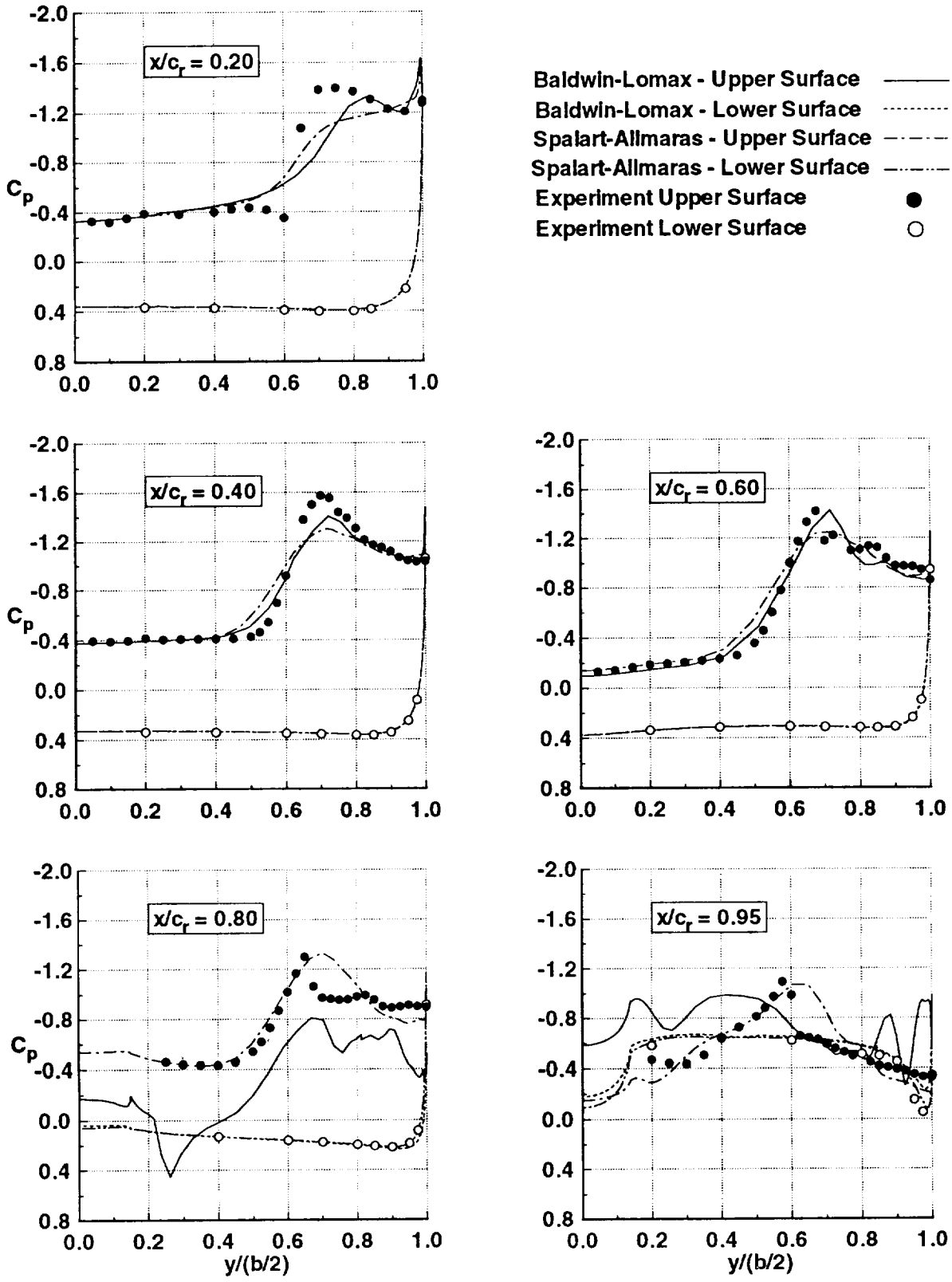

Figure 11.c. Turbulence model comparisons: Medium leading-edge radius, $M_\infty = 0.85$, $\alpha = 16.37^\circ$, $Rn = 6 \times 10^6$.

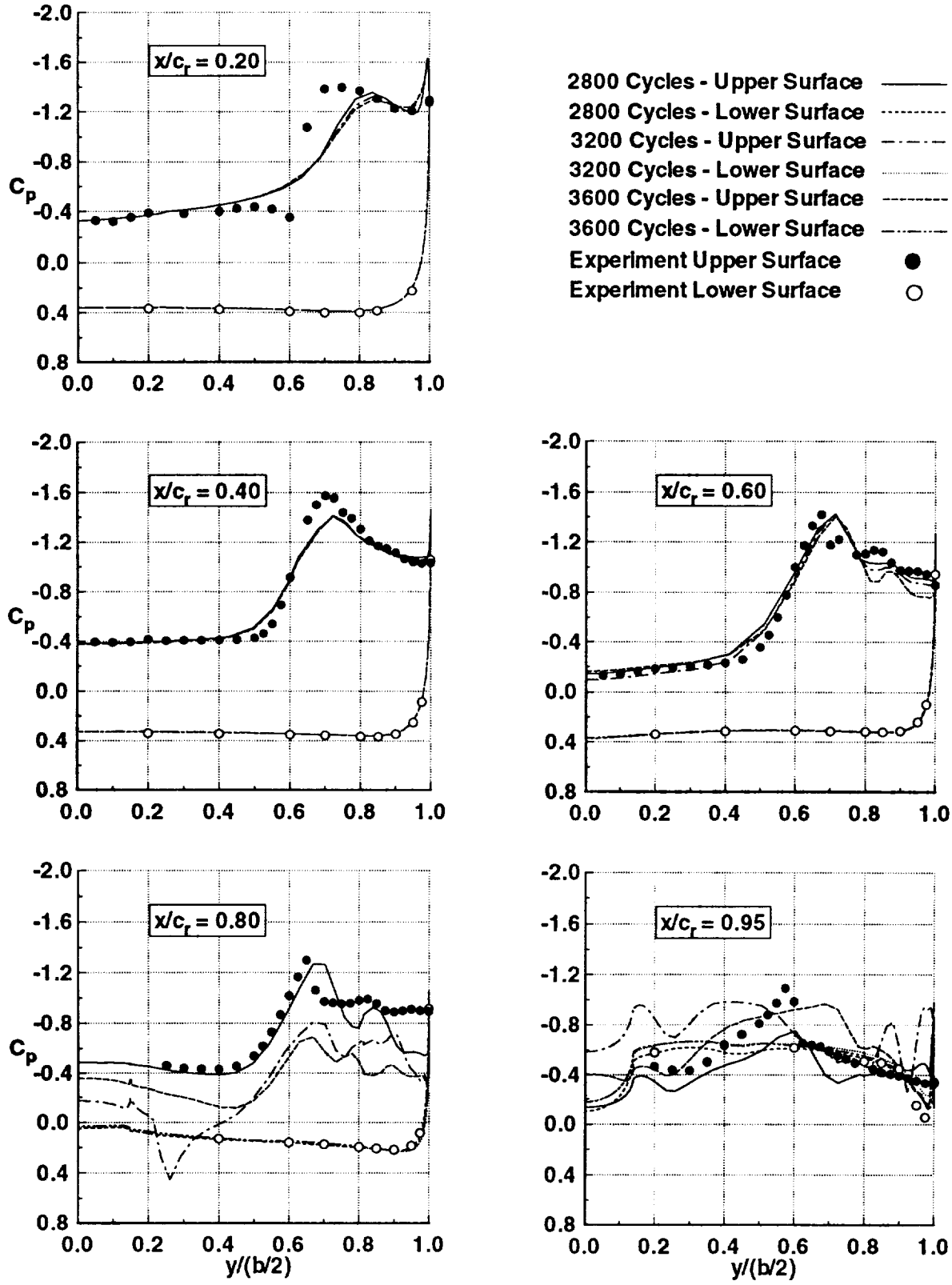

Figure 12. Baldwin-Lomax Turbulence model predicts oscillating pressures: Medium leading-edge radius, $M_\infty = 0.85$, $\alpha = 16.37°$, $Rn = 6 \times 10^6$.

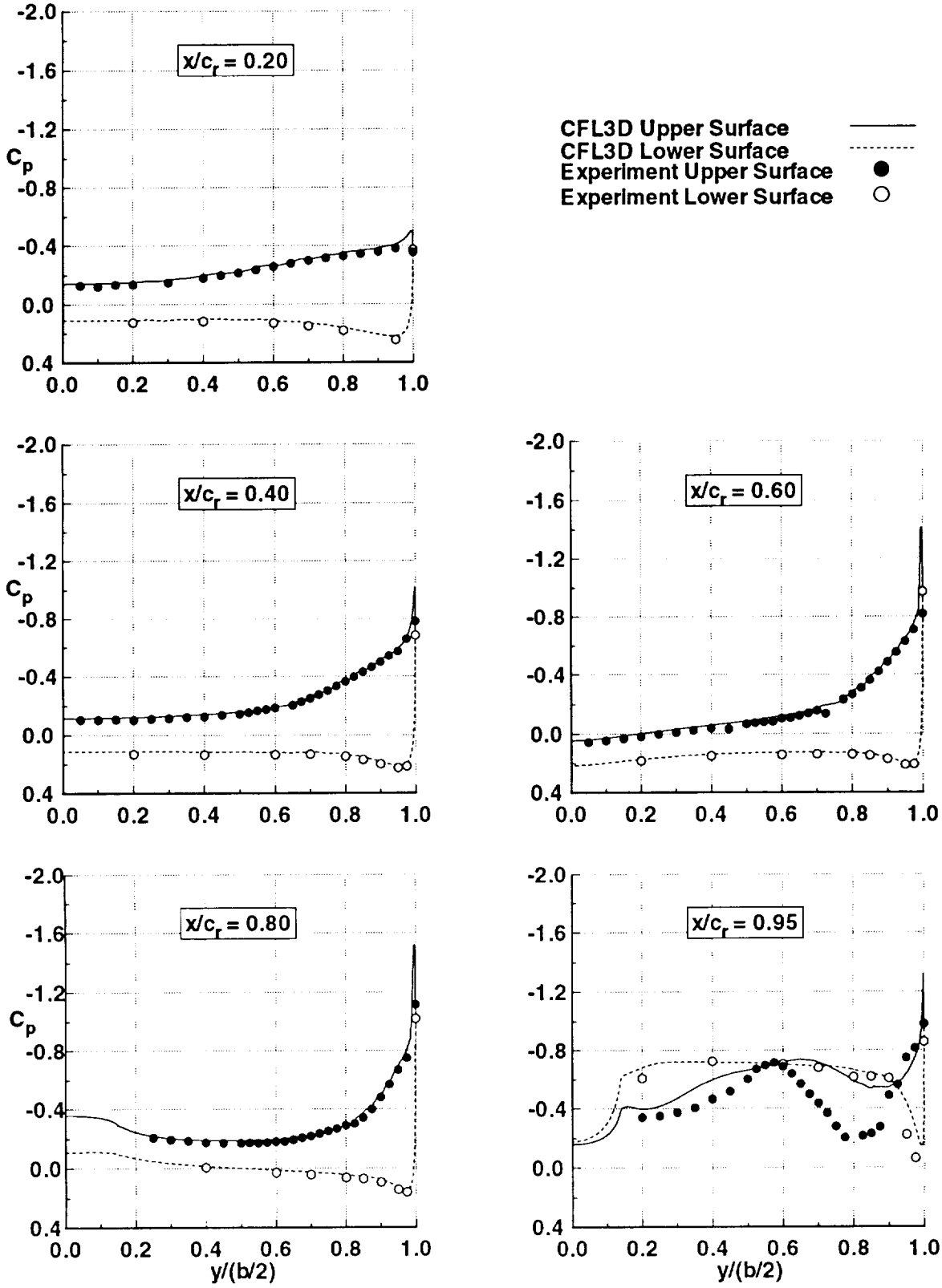

Figure 13.a. Medium leading-edge radius pressure coefficients, Spalart-Allmaras turbulence model, $M_\infty = 0.85$, $\alpha = 6.8^\circ$, $Rn = 48 \times 10^6$.

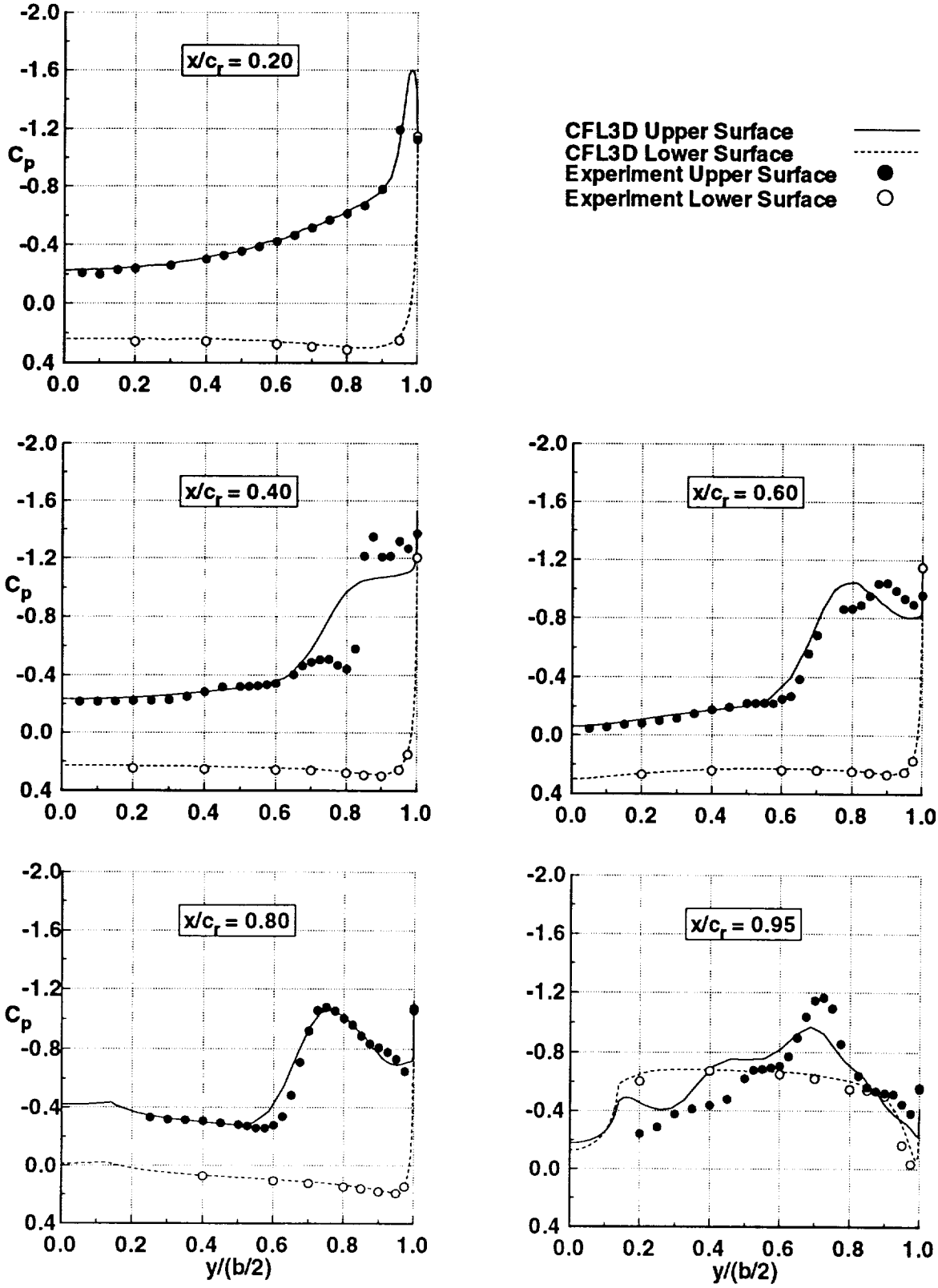

Figure 13.b. Medium leading-edge radius pressure coefficients, Spalart-Allmaras turbulence model, $M_\infty = 0.85$, $\alpha = 12.03^\circ$, $Rn = 48 \times 10^6$.

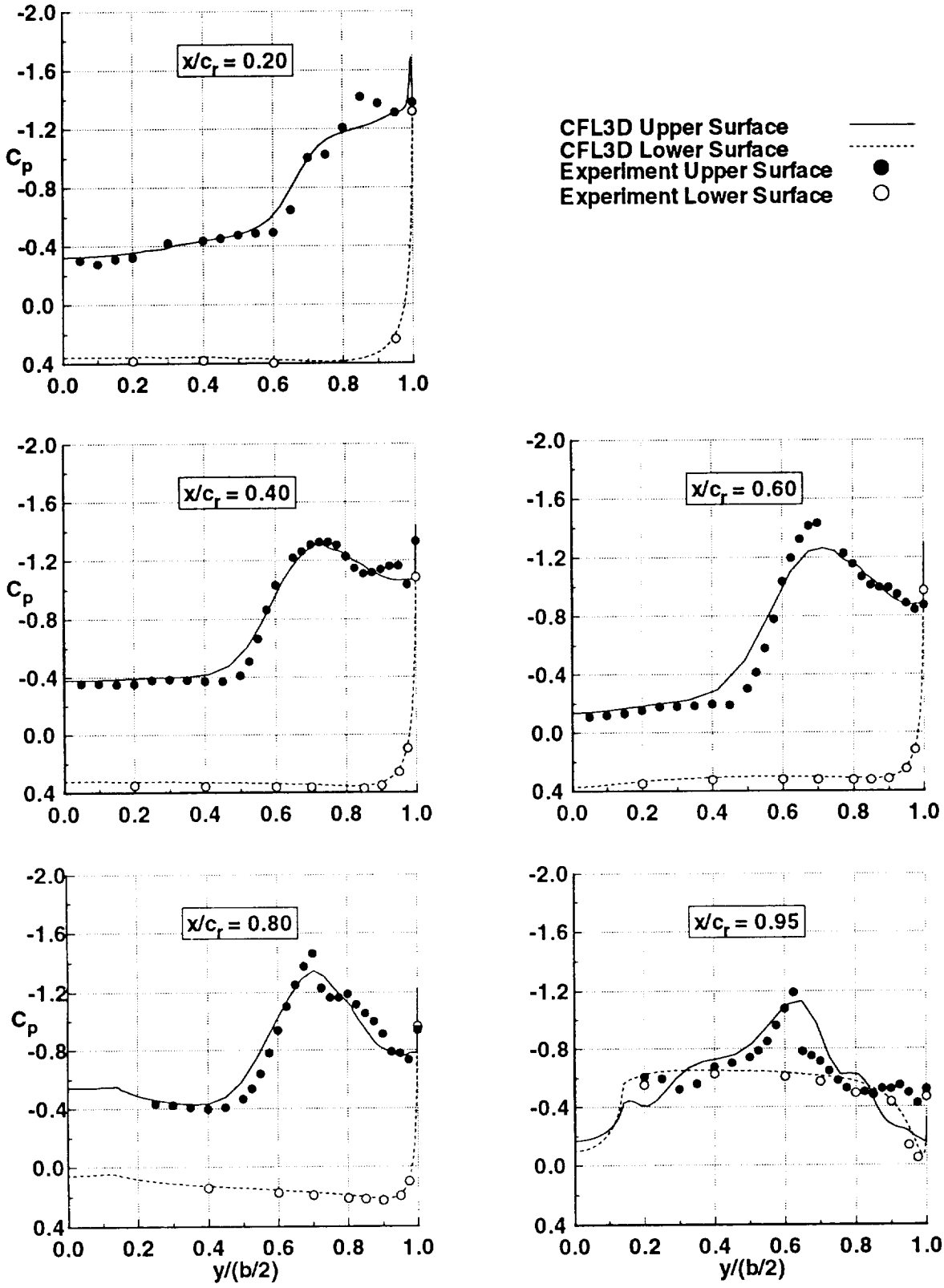

Figure 13.c. Medium leading-edge radius pressure coefficients, Spalart-Allmaras turbulence model, $M_\infty = 0.85$, $\alpha = 16.25^\circ$, $Rn = 48 \times 10^6$.

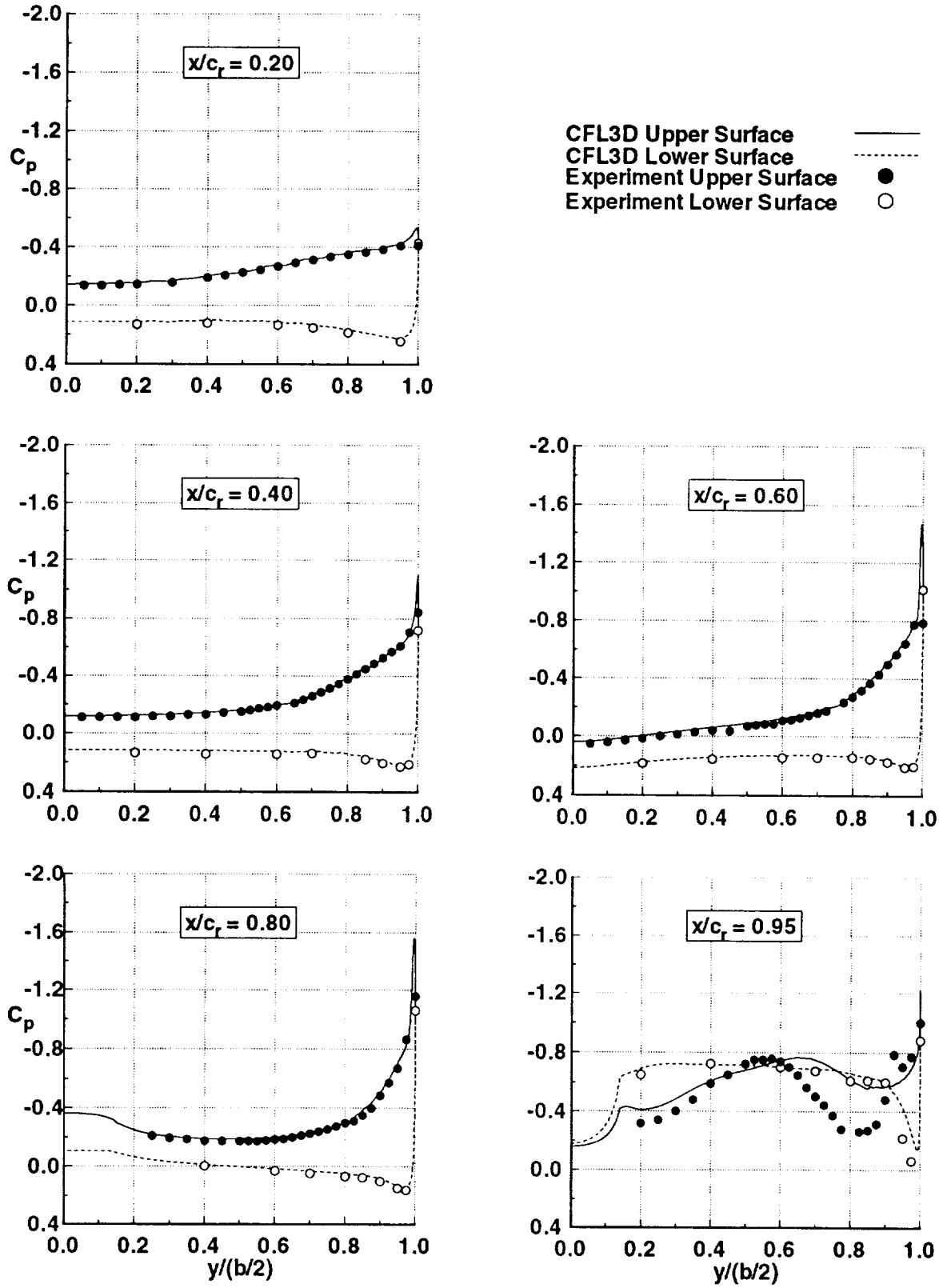

Figure 14.a. Medium leading-edge radius pressure coefficients, Spalart-Allmaras turbulence model, $M_\infty = 0.85$, $\alpha = 6.99^\circ$, $Rn = 84 \times 10^6$.

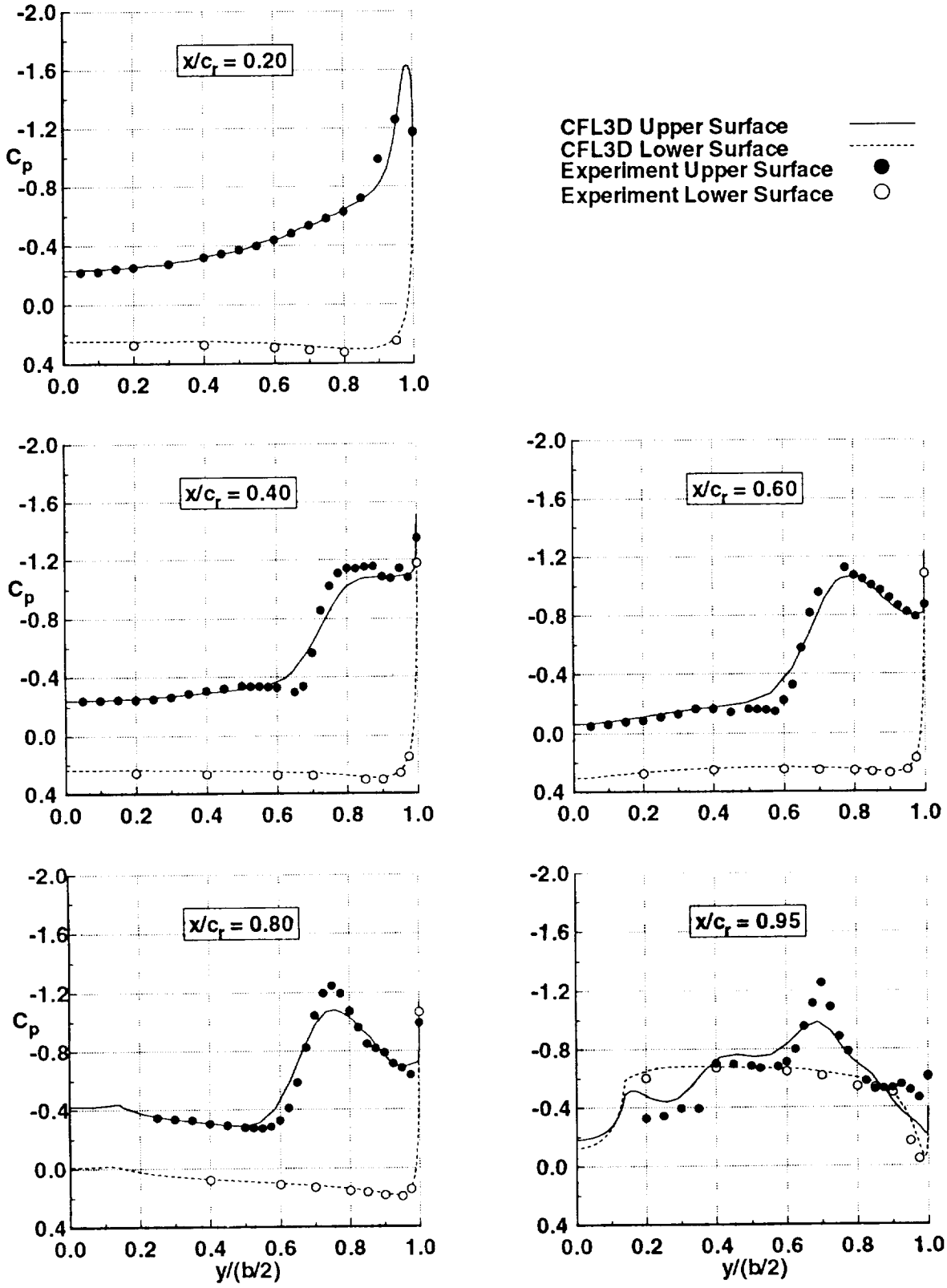

Figure 14.b. Medium leading-edge radius pressure coefficients, Spalart-Allmaras turbulence model, $M_\infty = 0.85$, $\alpha = 12.31^\circ$, $Rn = 84 \times 10^6$.

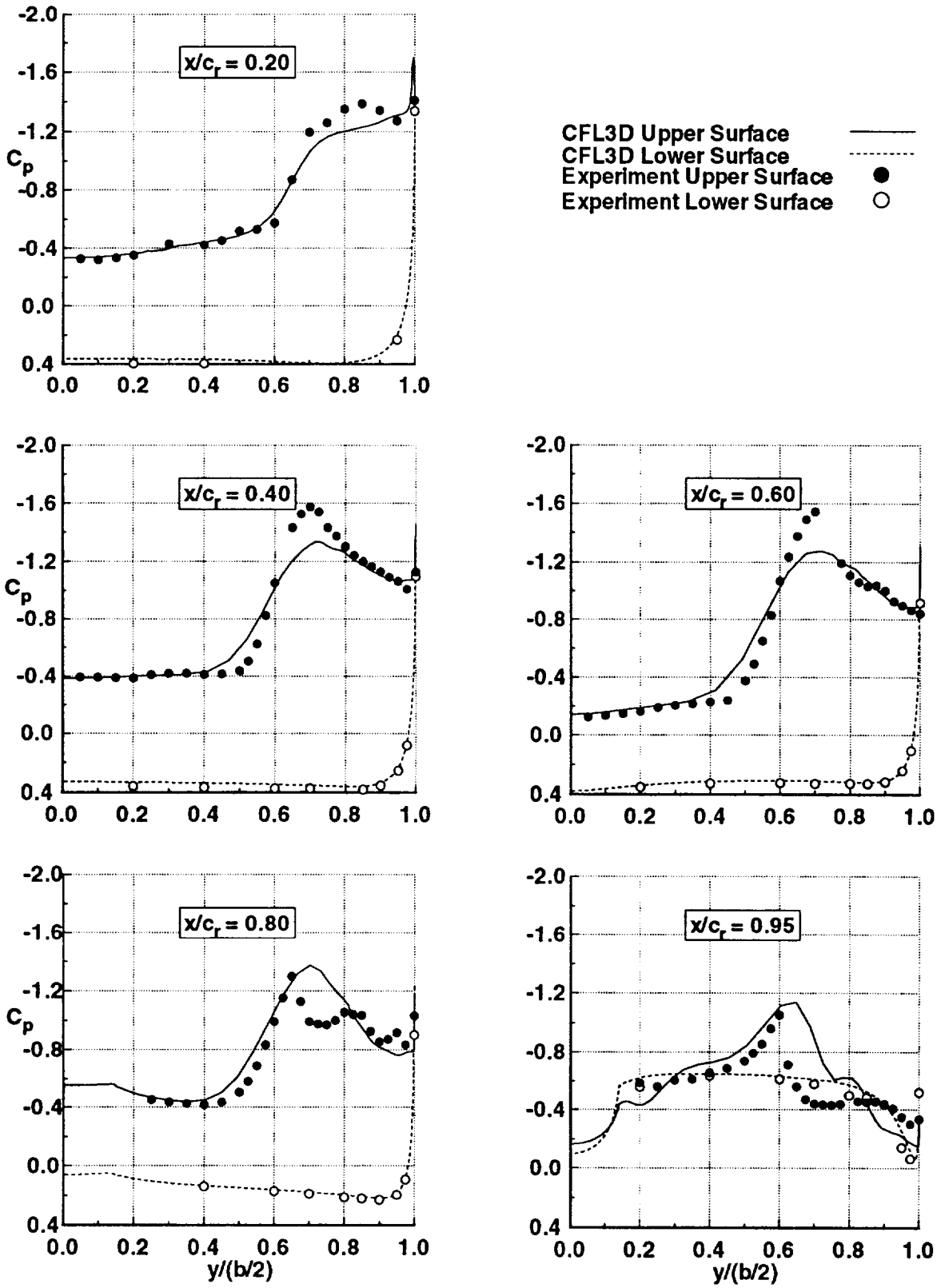

Figure 14.c. Medium leading-edge radius pressure coefficients, Spalart-Allmaras turbulence model, $M_\infty = 0.85$, $\alpha = 16.59^\circ$, Rn = 84×10^6.

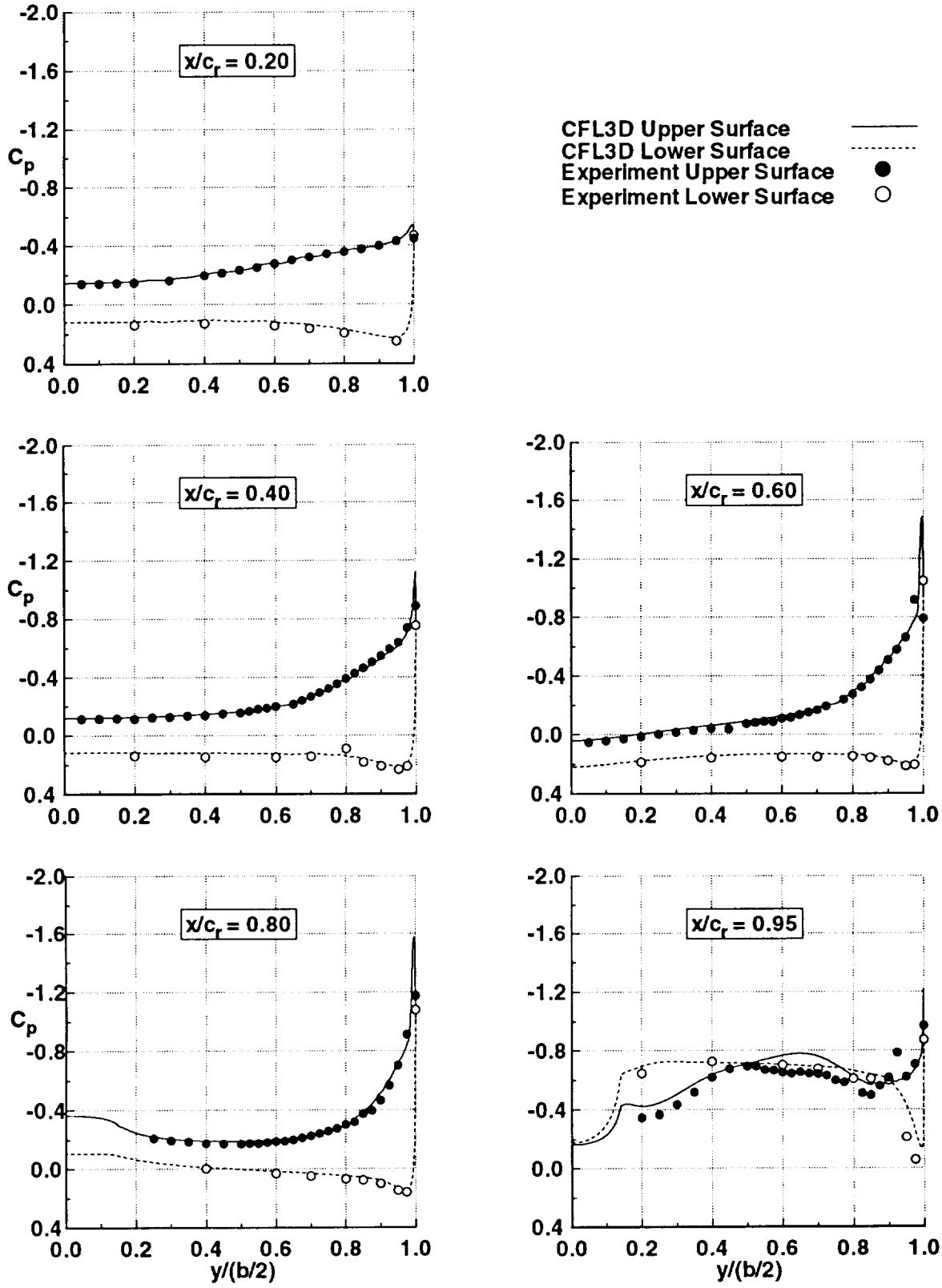

Figure 15.a. Medium leading-edge radius pressure coefficients, Spalart-Allmaras turbulence model, $M_\infty = 0.85$, $\alpha = 7.03^\circ$, $Rn = 120 \times 10^6$.

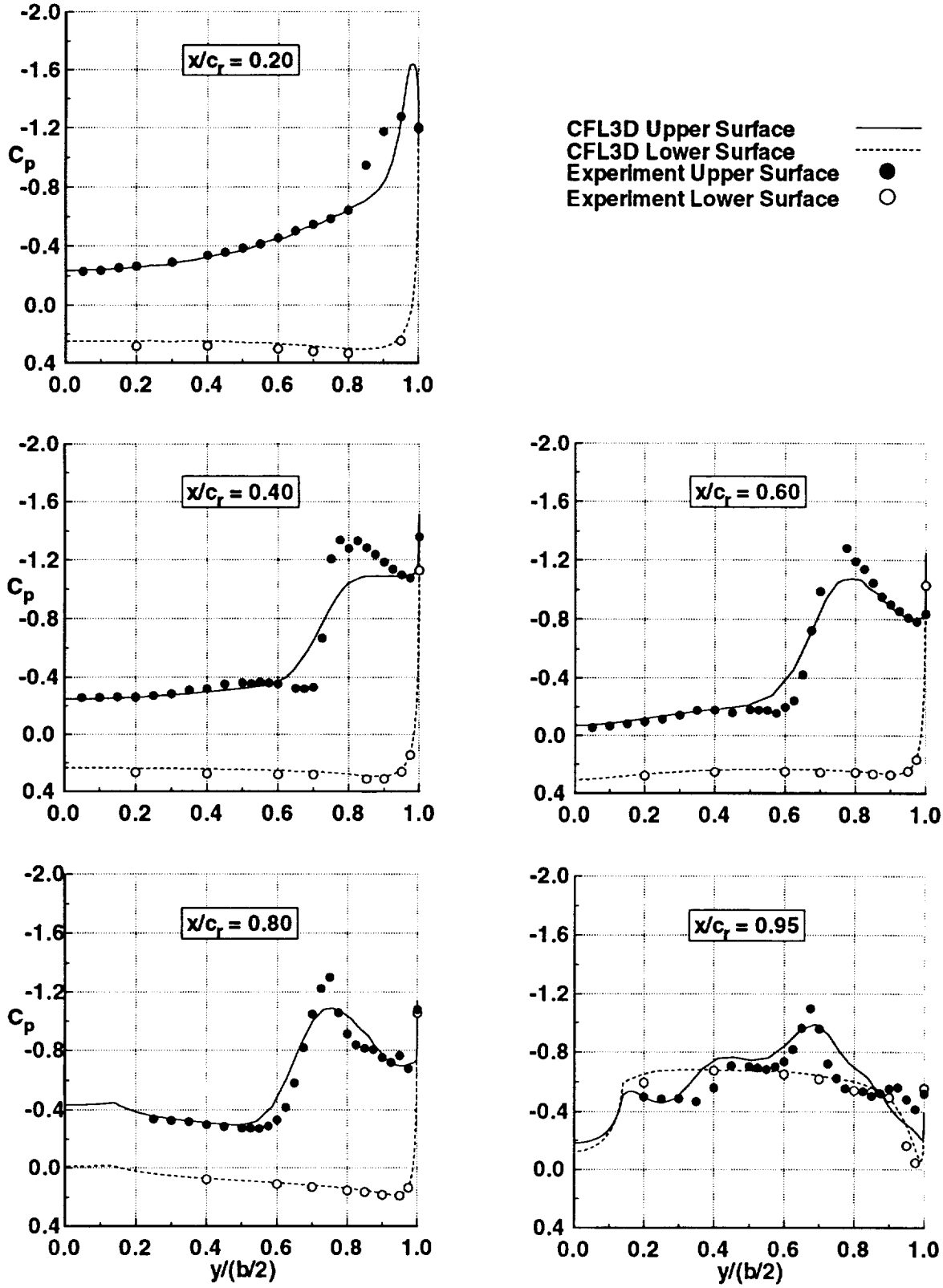

Figure 15.b. Medium leading-edge radius pressure coefficients, Spalart-Allmaras turbulence model, $M_\infty = 0.85$, $\alpha = 12.44^\circ$, $Rn = 120 \times 10^6$.

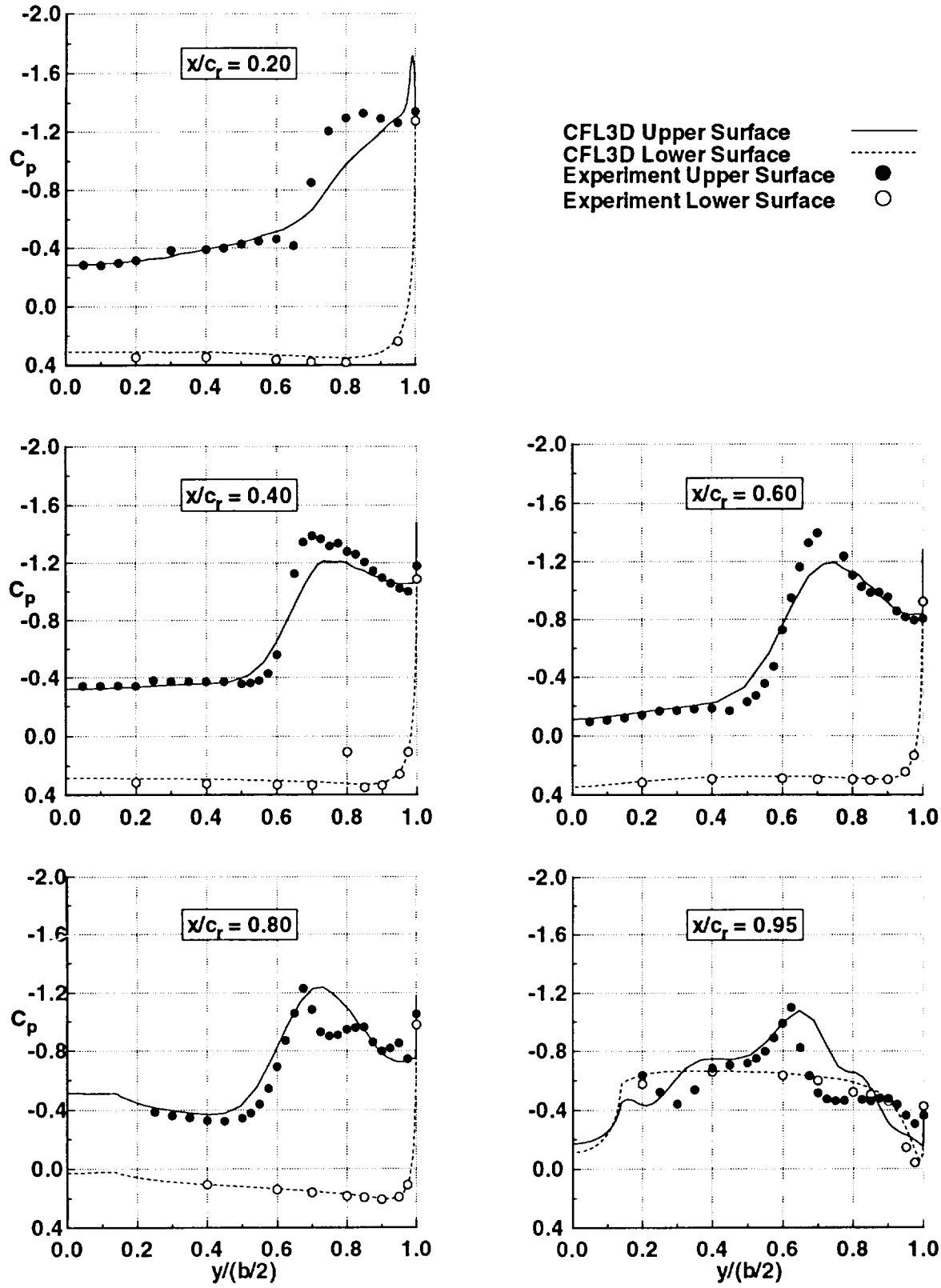

Figure 15.c. Medium leading-edge radius pressure coefficients, Spalart-Allmaras turbulence model, $M_\infty = 0.85$, $\alpha = 14.63^\circ$, $Rn = 120 \times 10^6$.

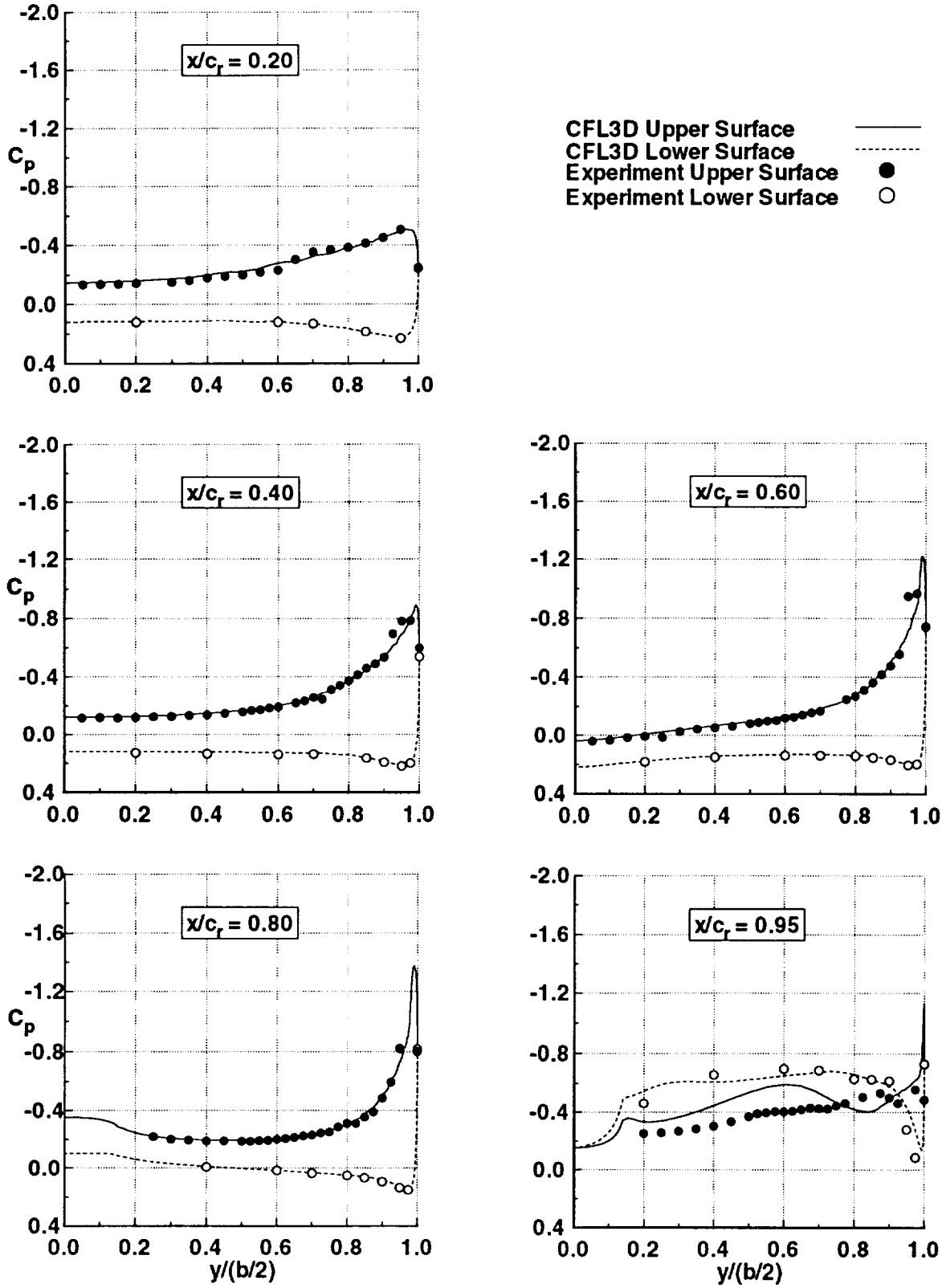

Figure 16.a. Round leading-edge radius pressure coefficients, Spalart-Allmaras turbulence model, $M_\infty = 0.85$, $\alpha = 7.14^\circ$, $Rn = 6 \times 10^6$.

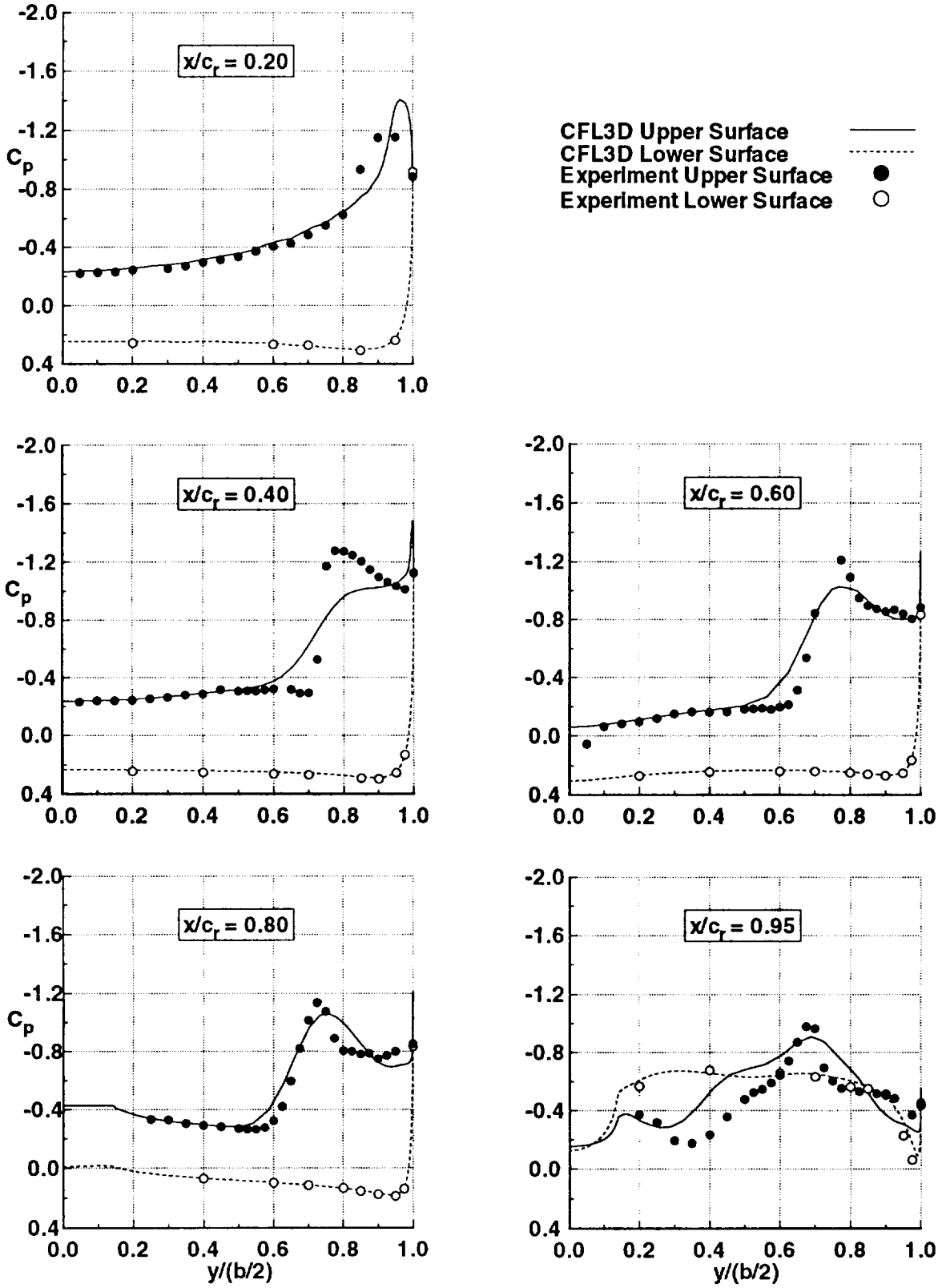

Figure 16.b. Round leading-edge radius pressure coefficients, Spalart-Allmaras turbulence model, $M_\infty = 0.85$, $\alpha = 12.28^\circ$, $Rn = 6 \times 10^6$.

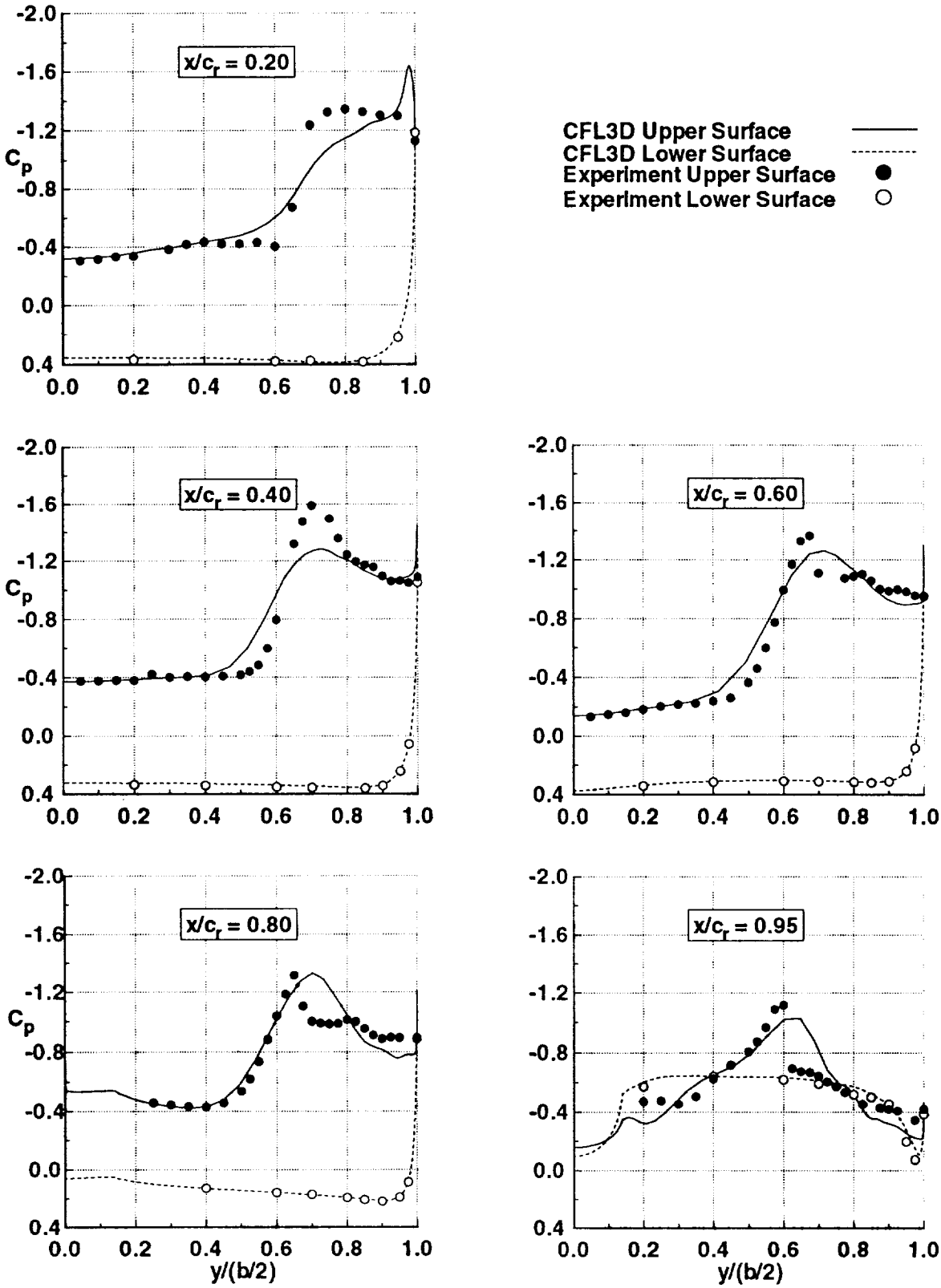

Figure 16.c. Round leading-edge radius pressure coefficients, Spalart-Allmaras turbulence model, $M_\infty = 0.85$, $\alpha = 16.37°$, $Rn = 6 \times 10^6$.

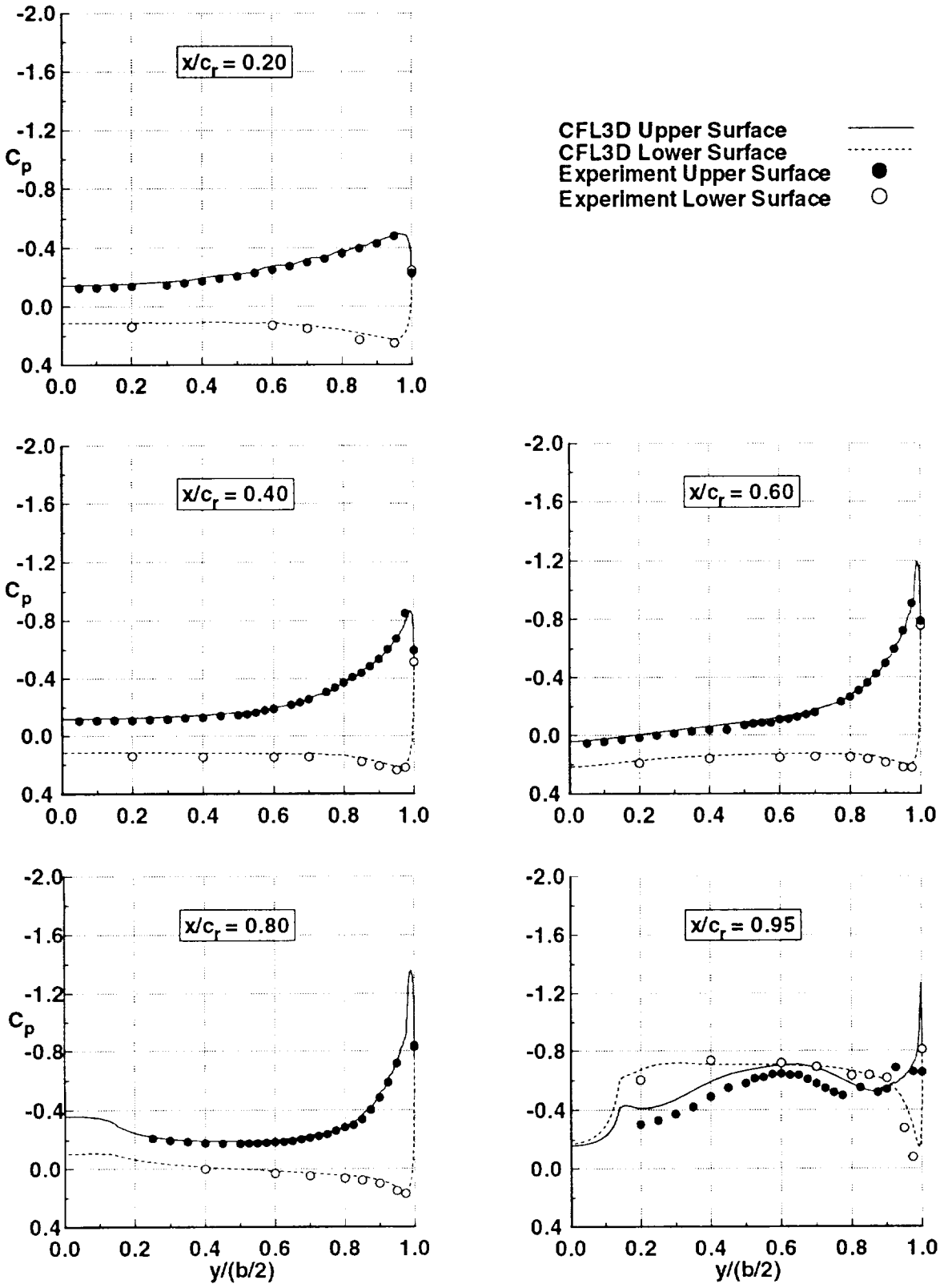

Figure 17.a. Round leading-edge radius pressure coefficients, Spalart-Allmaras turbulence model, $M_\infty = 0.85$, $\alpha = 6.98^\circ$, $Rn = 48 \times 10^6$.

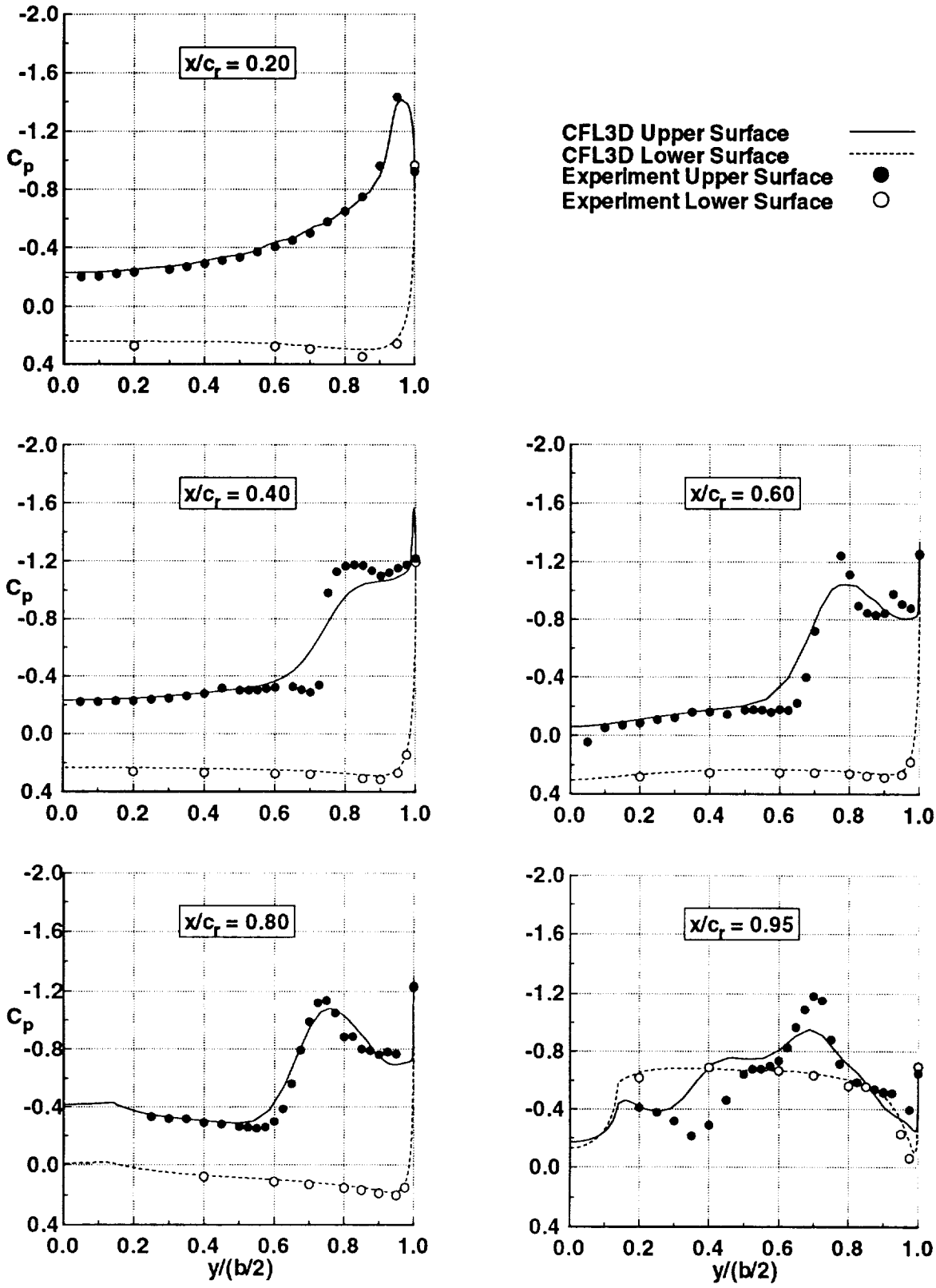

Figure 17.b. Round leading-edge radius pressure coefficients, Spalart-Allmaras turbulence model, $M_\infty = 0.85$, $\alpha = 12.24^\circ$, $Rn = 48 \times 10^6$.

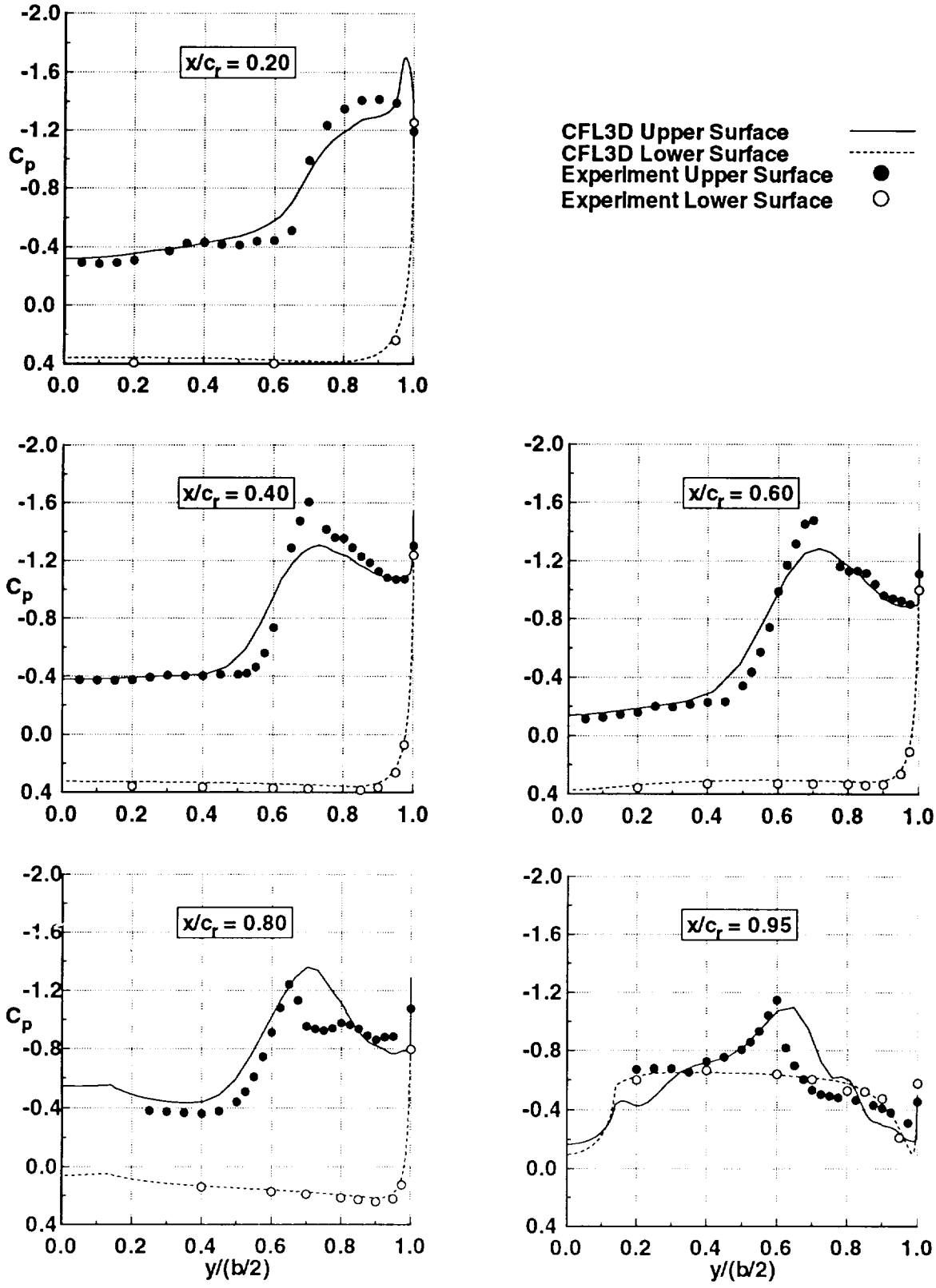

Figure 17.c. Round leading-edge radius pressure coefficients, $M_\infty = 0.85$, $\alpha = 16.44^\circ$, $Rn = 48 \times 10^6$.

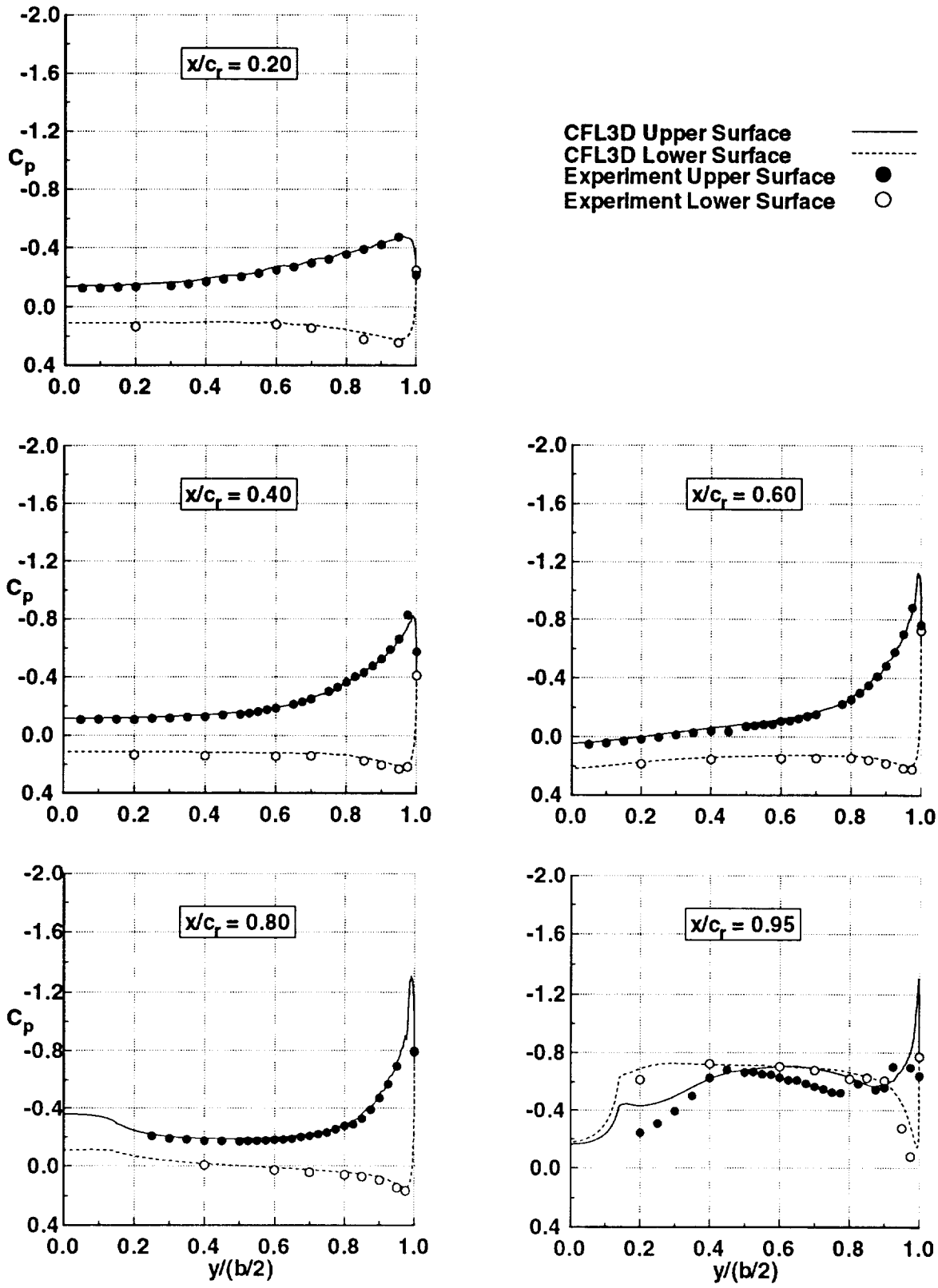

Figure 18.a. Round leading-edge radius pressure coefficients, Spalart-Allmaras turbulence model, $M_\infty = 0.85$, $\alpha = 6.78^\circ$, $Rn = 84 \times 10^6$.

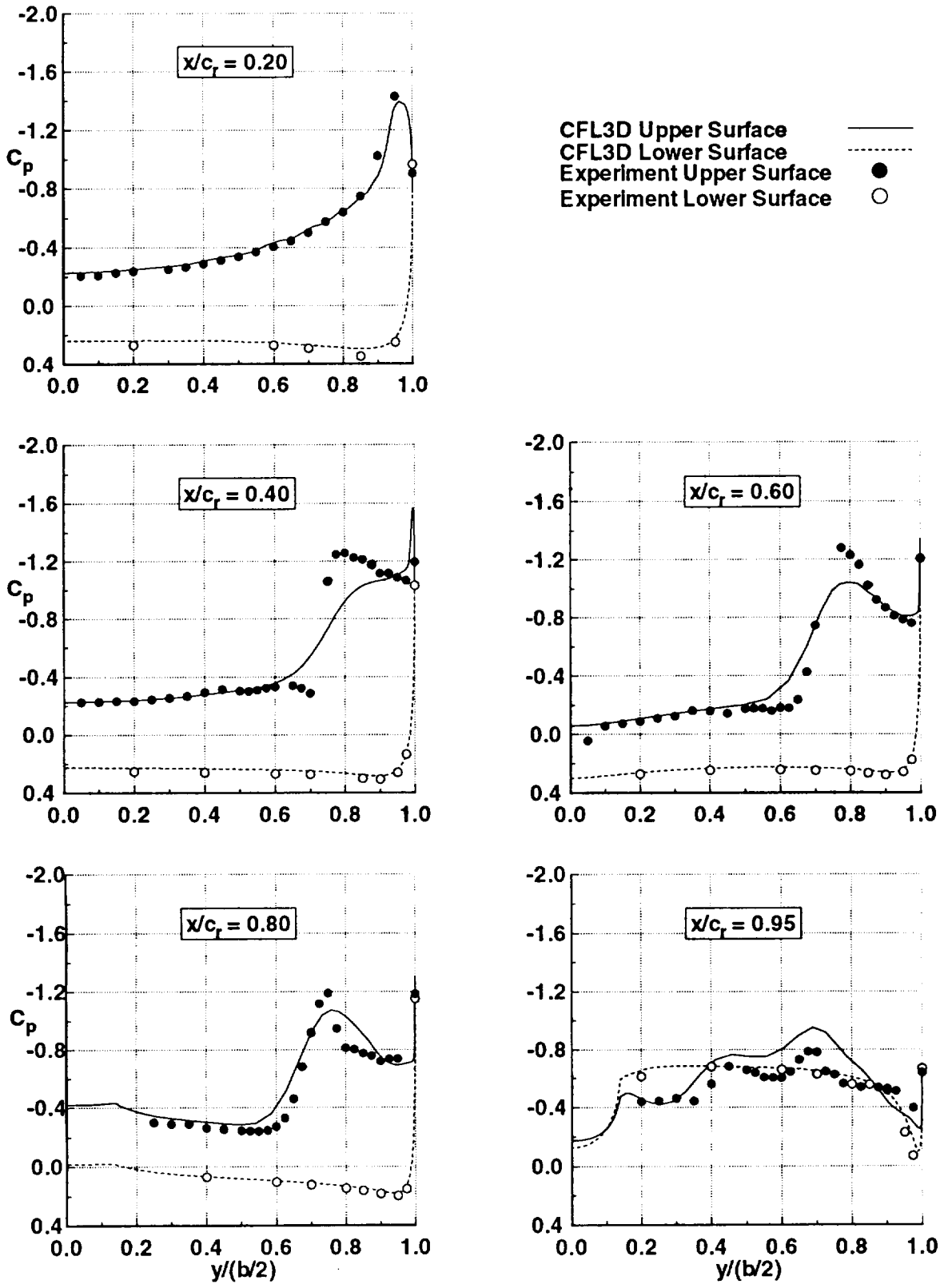

Figure 18.b. Round leading-edge radius pressure coefficients, Spalart-Allmaras turbulence model, $M_\infty = 0.85$, $\alpha = 12.09^\circ$, $Rn = 84 \times 10^6$.

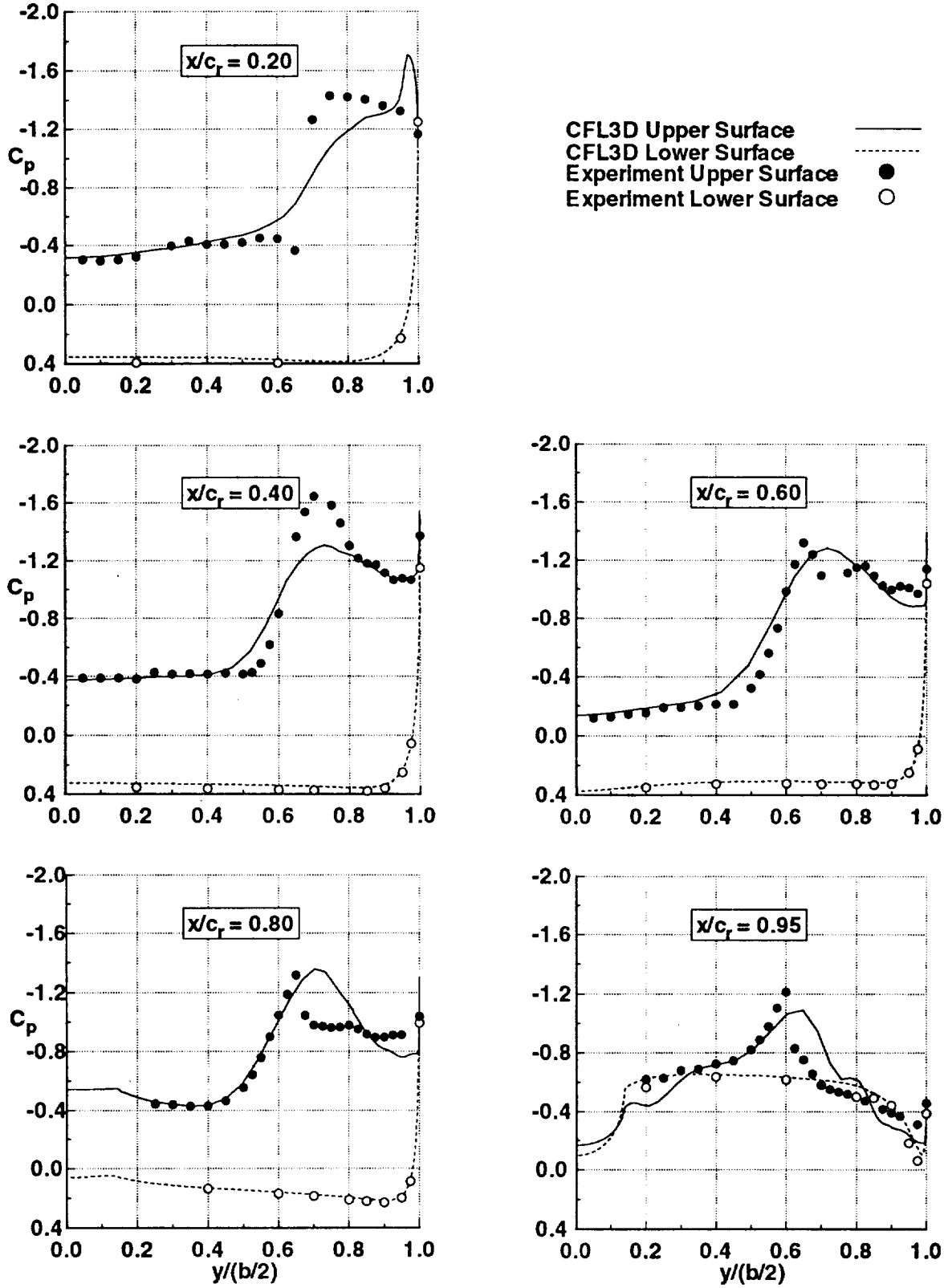

Figure 18.c. Round leading-edge radius pressure coefficients, Spalart-Allmaras turbulence model, $M_\infty = 0.85$, $\alpha = 16.38^\circ$, $Rn = 84 \times 10^6$.

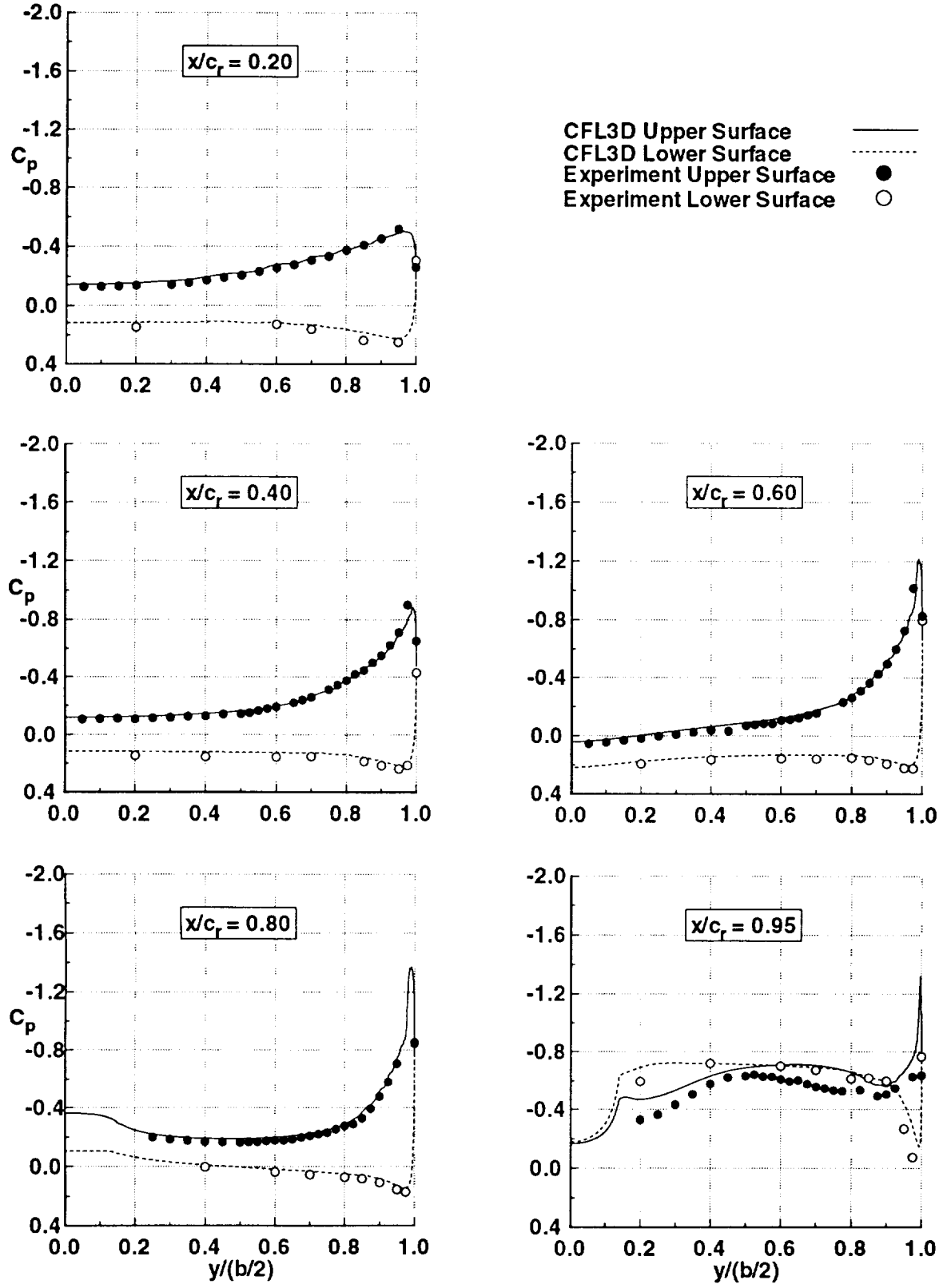

Figure 19.a. Round leading-edge radius pressure coefficients, Spalart-Allmaras turbulence model, $M_\infty = 0.85$, $\alpha = 7.03^\circ$, Rn = 120×10^6.

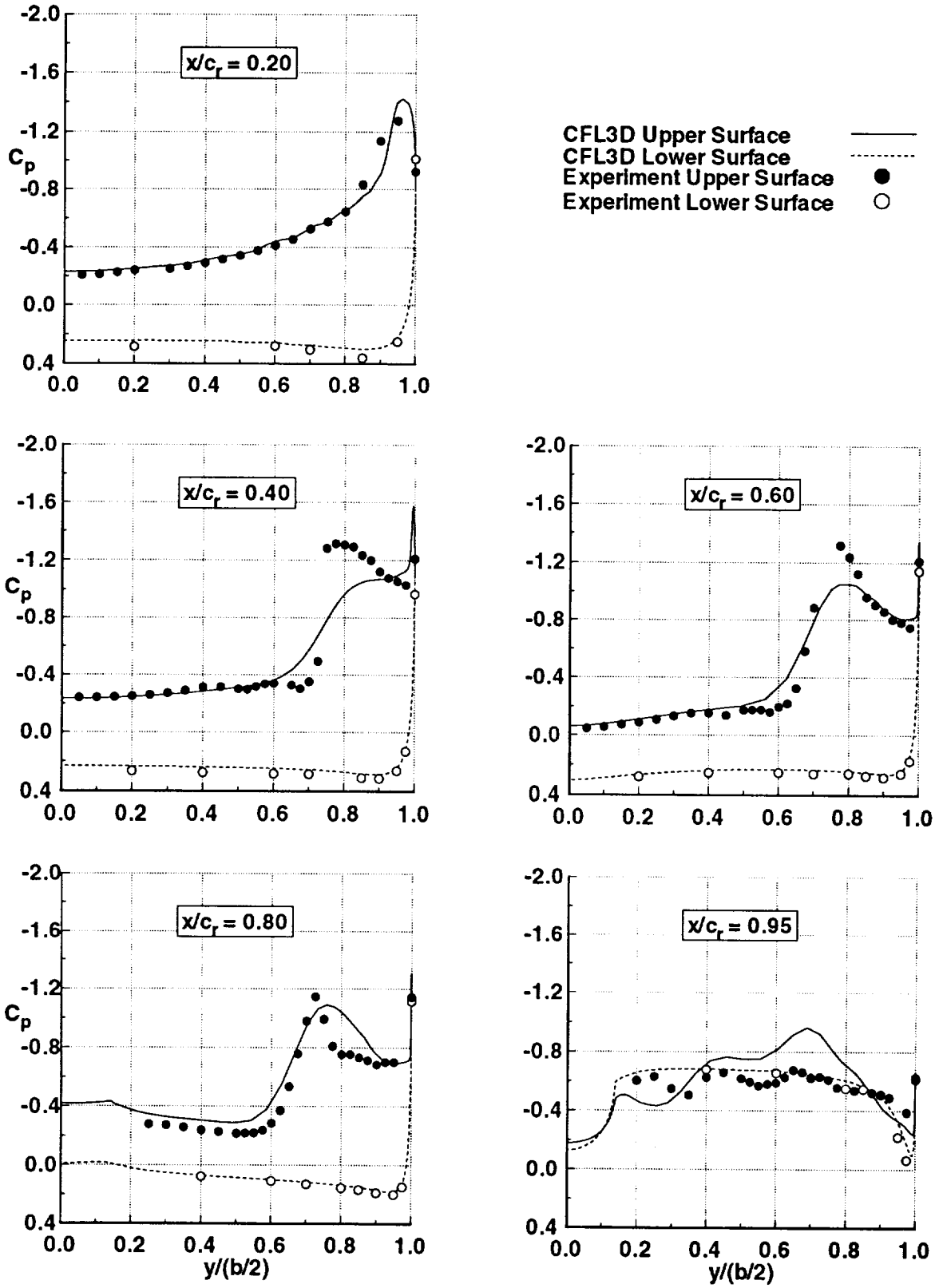

Figure 19.b. Round leading-edge radius pressure coefficients, Spalart-Allmaras turbulence model, $M_\infty = 0.85$, $\alpha = 12.29^\circ$, Rn = 120×10^6.

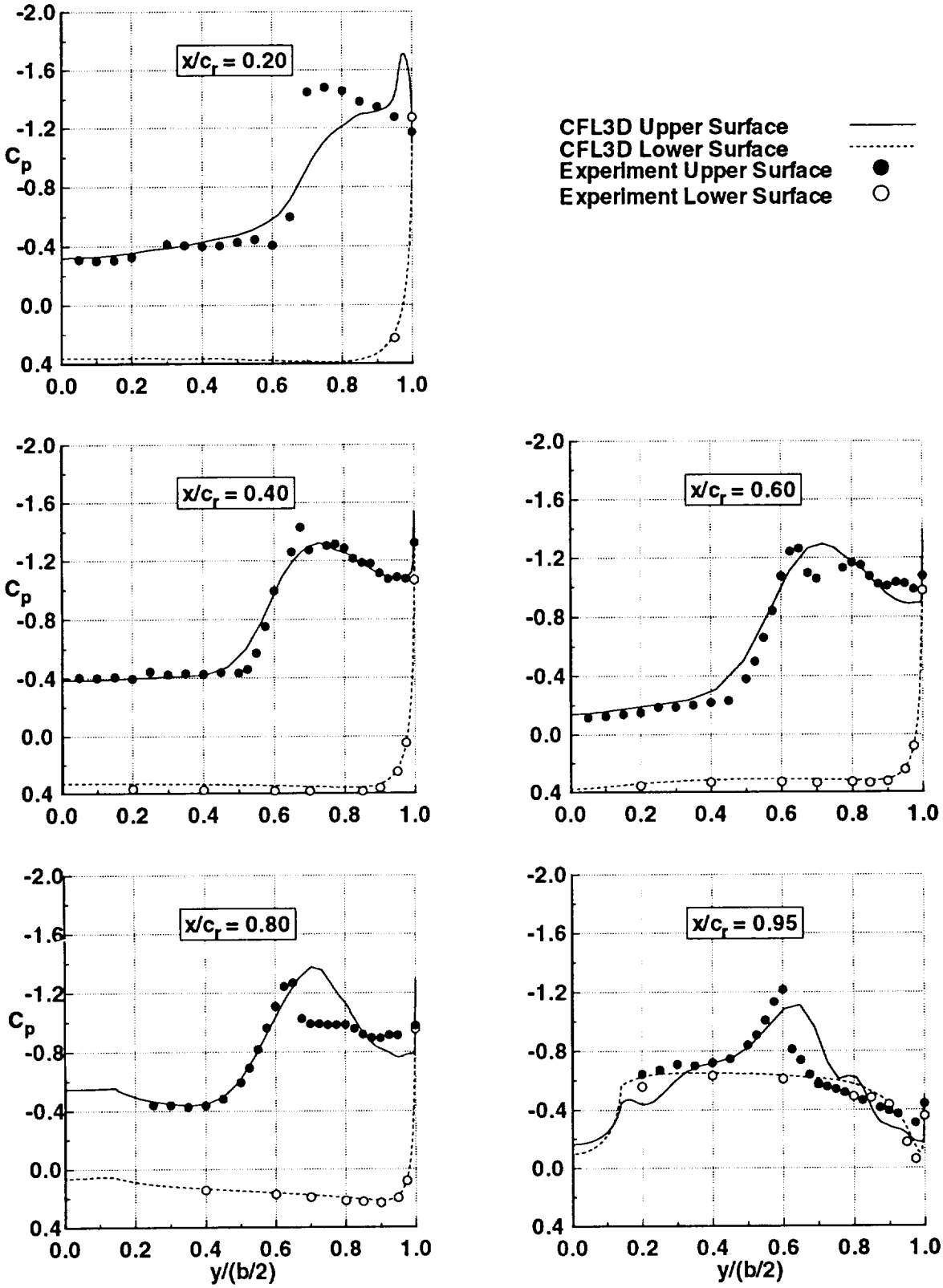

Figure 19.c. Round leading-edge radius pressure coefficients, Spalart-Allmaras turbulence model, $M_\infty = 0.85$, $\alpha = 16.59^\circ$, Rn = 120×10^6.

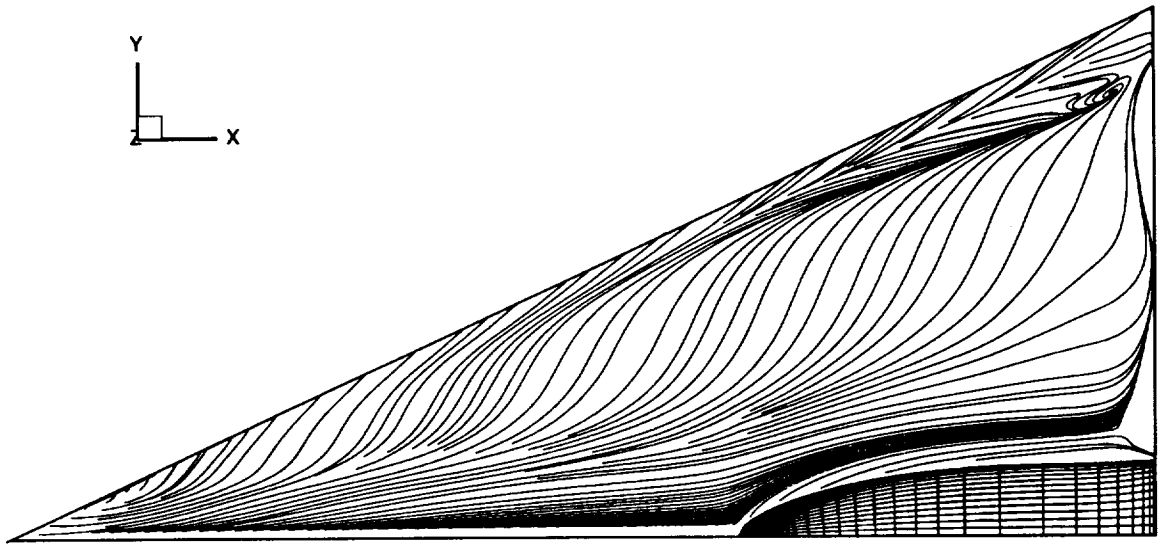

Figure 20.a. Computational surface streamlines, Spalart-Allmaras turbulence model, medium leading-edge radius, $M_\infty = 0.85$, $\alpha = 16.37^\circ$, $Rn = 6\times10^6$.

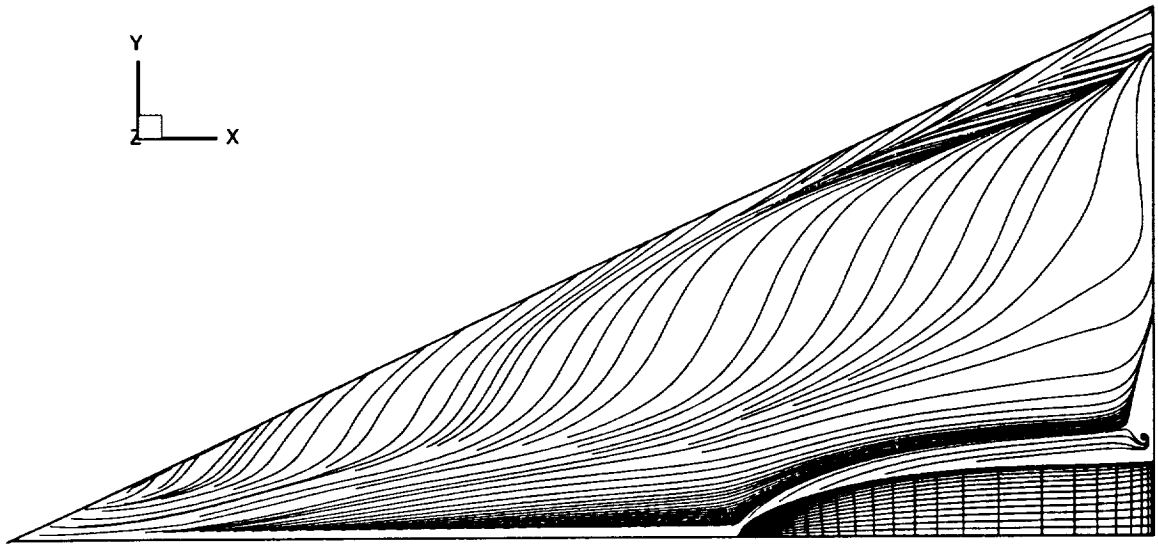

Figure 20.b. Computational surface streamlines, Spalart-Allmaras turbulence model, medium leading-edge radius, $M_\infty = 0.85$, $\alpha = 16.25^\circ$, $Rn = 48\times10^6$.

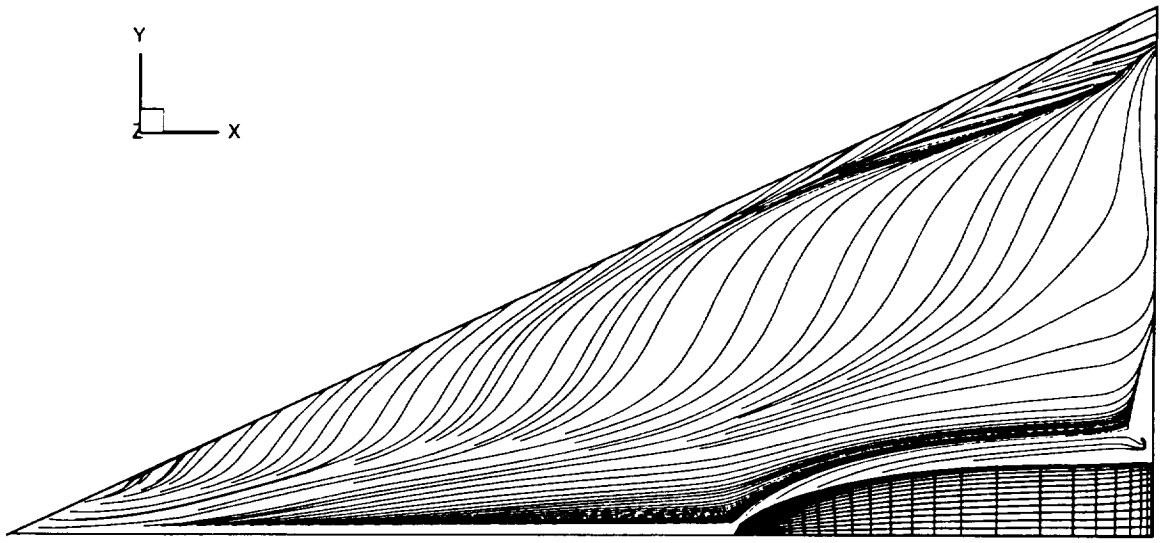

Figure 20.c. Computational surface streamlines, Spalart-Allmaras turbulence model, medium leading-edge radius, $M_\infty = 0.85$, $\alpha = 16.59^\circ$, $Rn = 84 \times 10^6$.

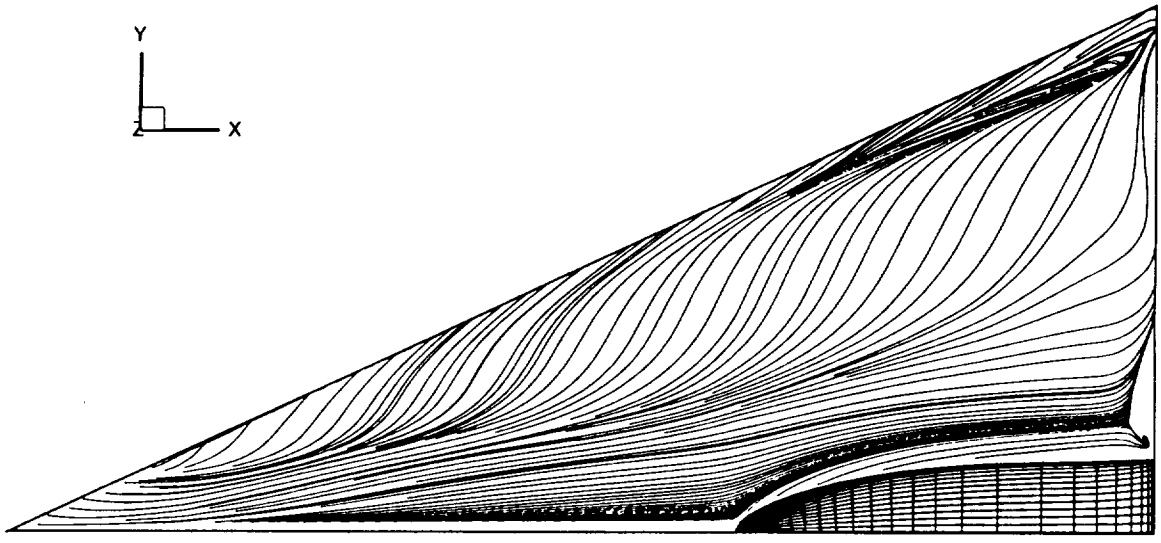

Figure 20.d. Computational surface streamlines, Spalart-Allmaras turbulence model, medium leading-edge radius, $M_\infty = 0.85$, $\alpha = 14.63^\circ$, $Rn = 120 \times 10^6$.

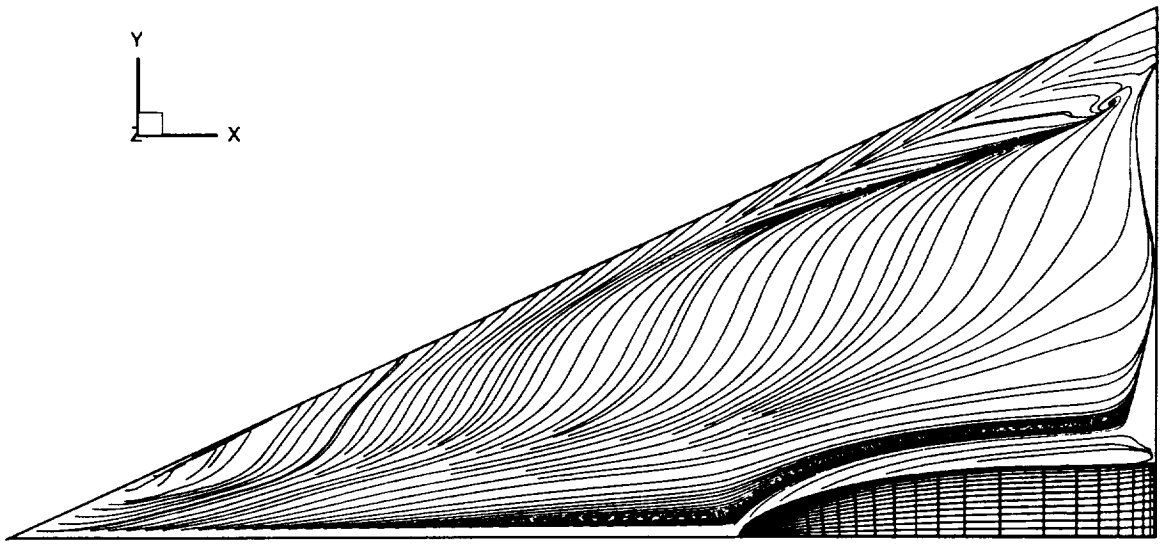

Figure 21.a. Computational surface streamlines, Spalart-Allmaras turbulence model, round leading-edge radius, $M_\infty = 0.85$, $\alpha = 16.37^\circ$, $Rn = 6\times10^6$.

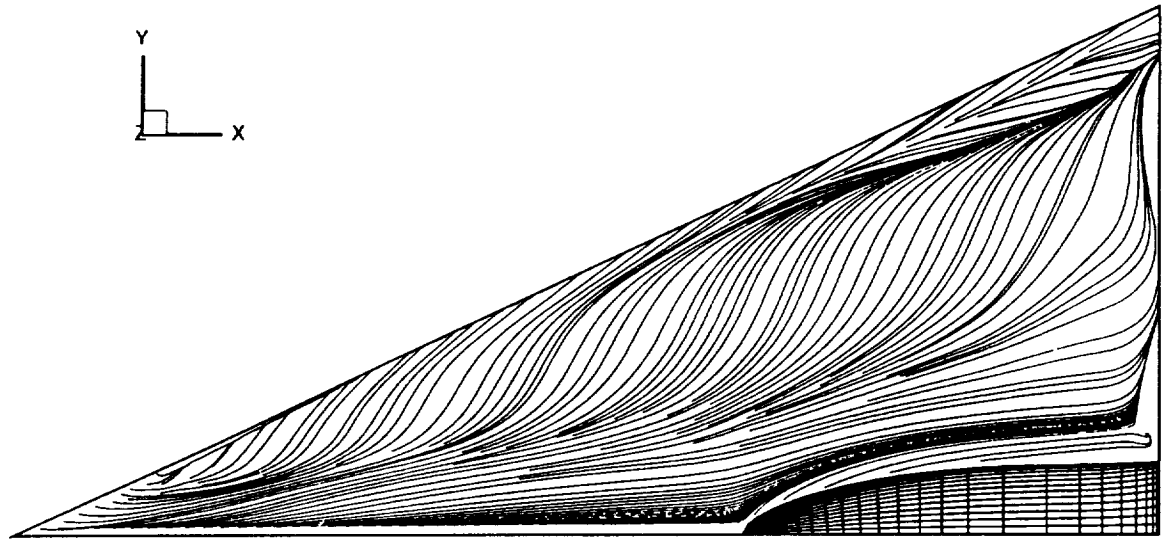

Figure 21.b. Computational surface streamlines, Spalart-Allmaras turbulence model, round leading-edge radius, $M_\infty = 0.85$, $\alpha = 16.44^\circ$, $Rn = 48\times10^6$.

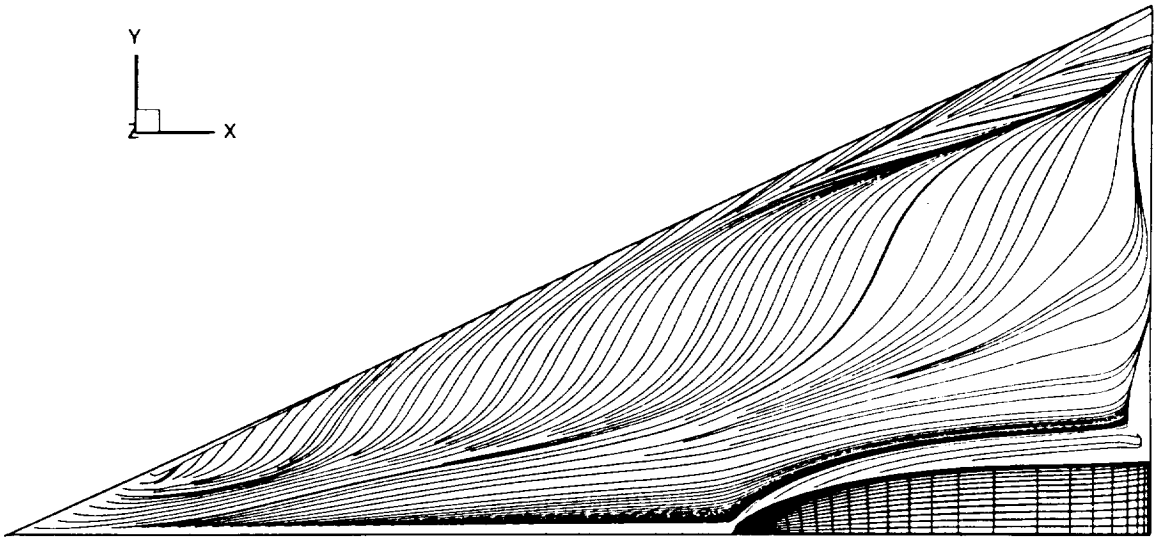

Figure 21.c. Computational surface streamlines, Spalart-Allmaras turbulence model, round leading-edge radius, $M_\infty = 0.85$, $\alpha = 16.38^\circ$, $Rn = 84 \times 10^6$.

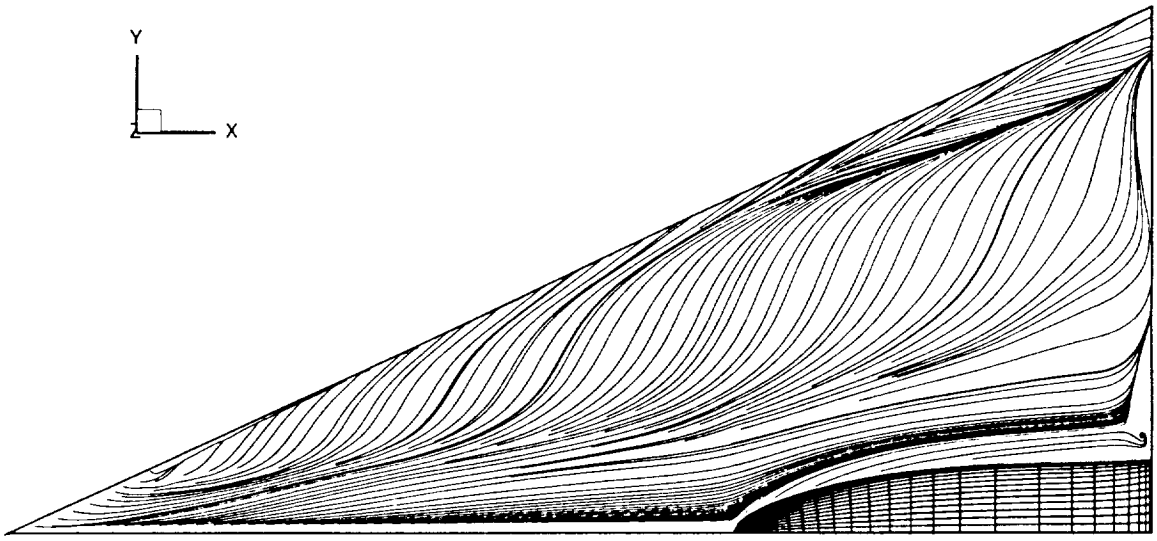

Figure 21.d. Computational surface streamlines, Spalart-Allmaras turbulence model, round leading-edge radius, $M_\infty = 0.85$, $\alpha = 16.59^\circ$, $Rn = 120 \times 10^6$.

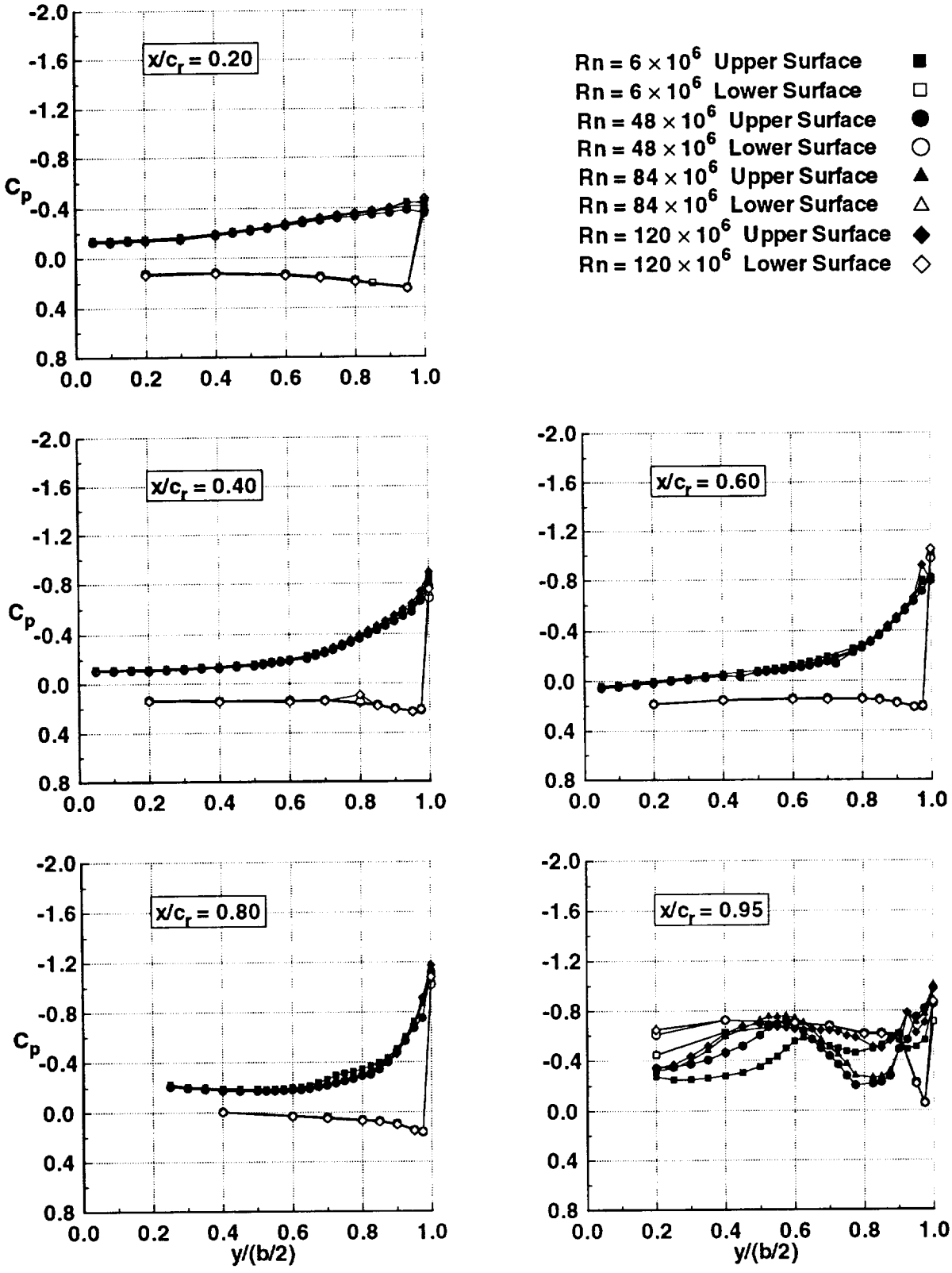

Figure 22.a. Reynolds number effect on pressure coefficients, medium leading-edge radius, $M_\infty = 0.85$, $\alpha = 7^\circ$, experiment.

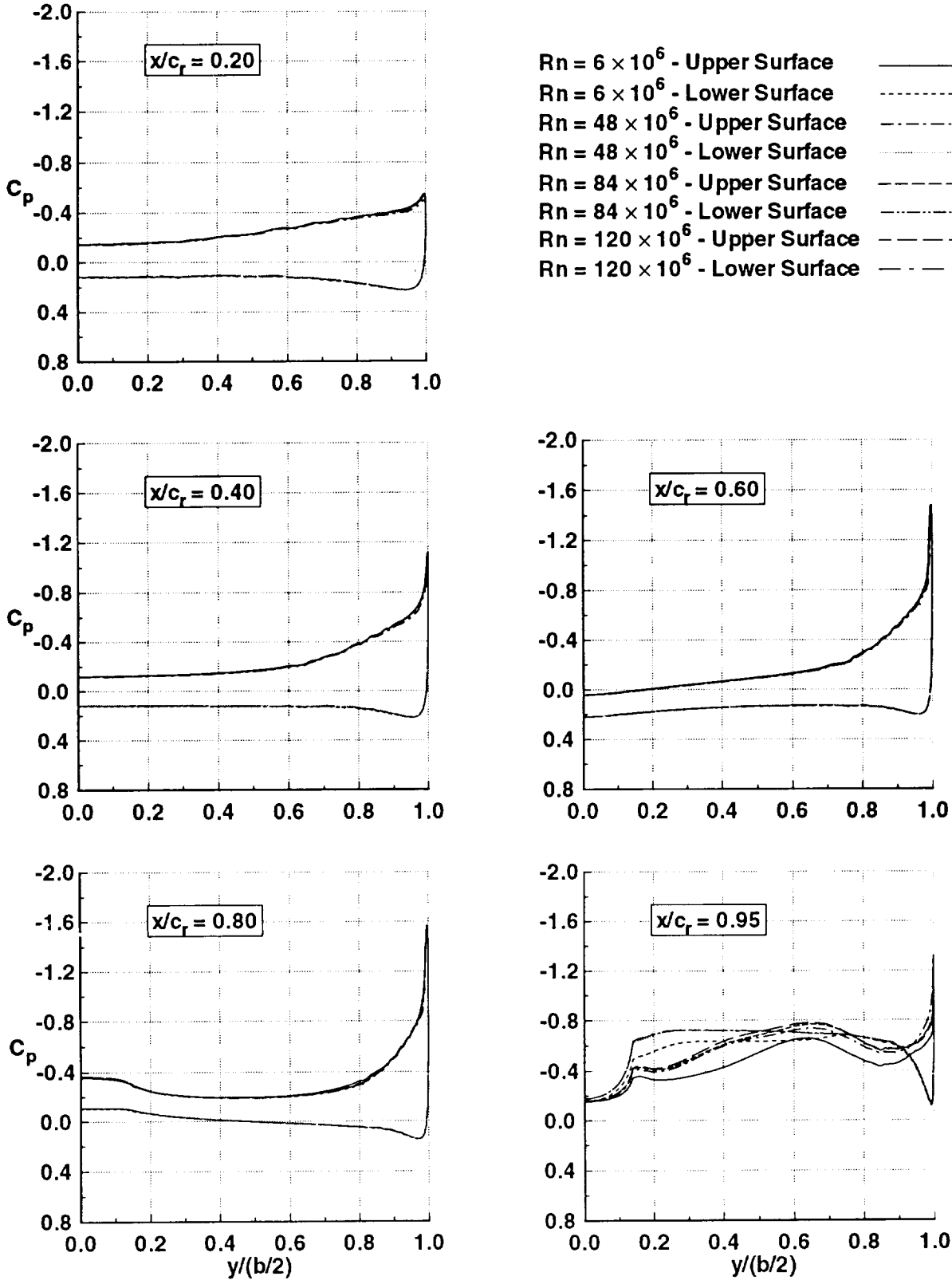

Figure 22.b. Predicted Reynolds number effect on pressure coefficients, medium leading-edge radius, $M_\infty = 0.85$, $\alpha = 7^\circ$, CFL3D, Spalart-Allmaras turbulence model.

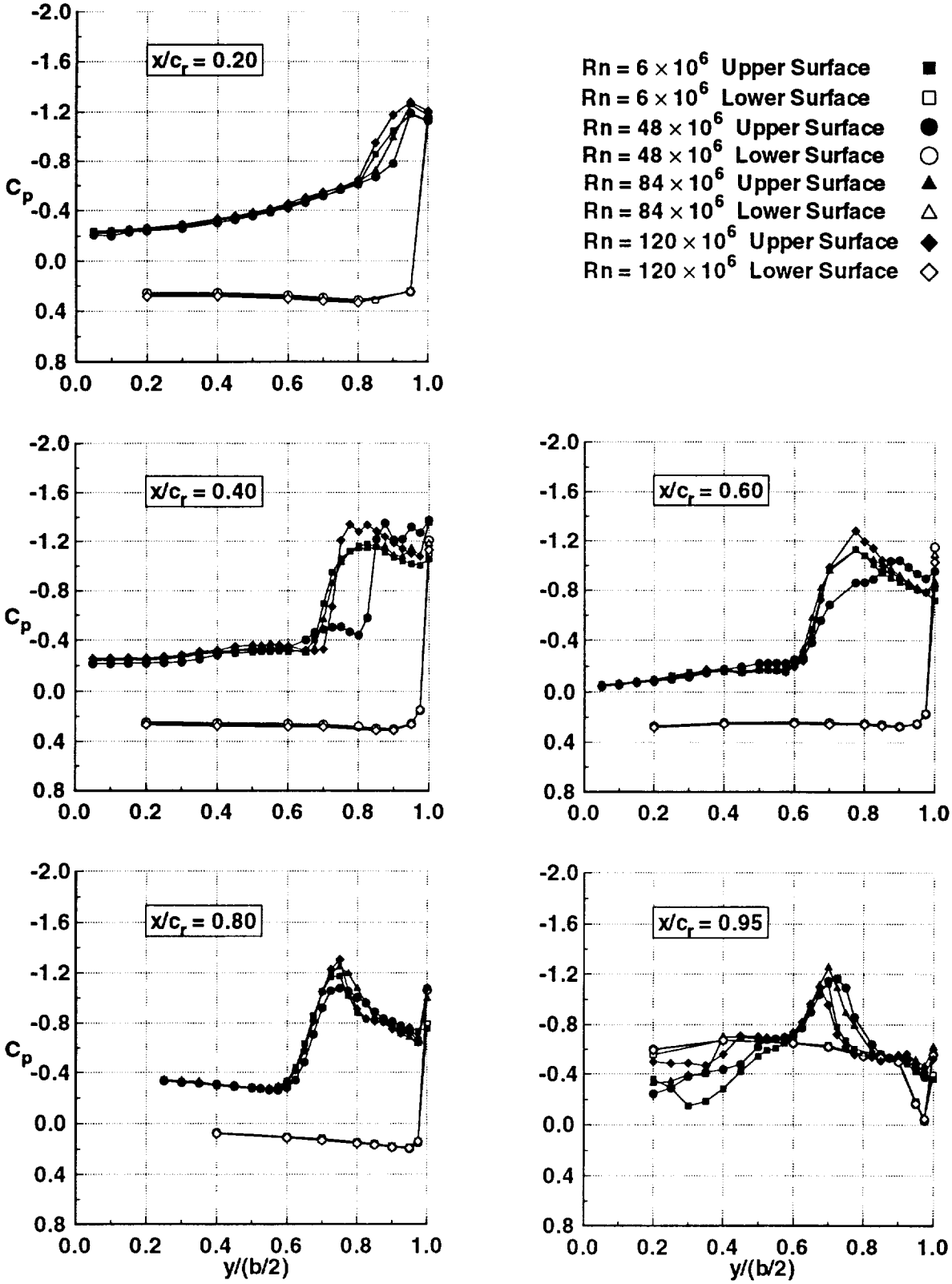

Figure 22.c. Reynolds number effect on pressure coefficients, medium leading-edge radius, $M_\infty = 0.85$, $\alpha = 12^\circ$, experiment.

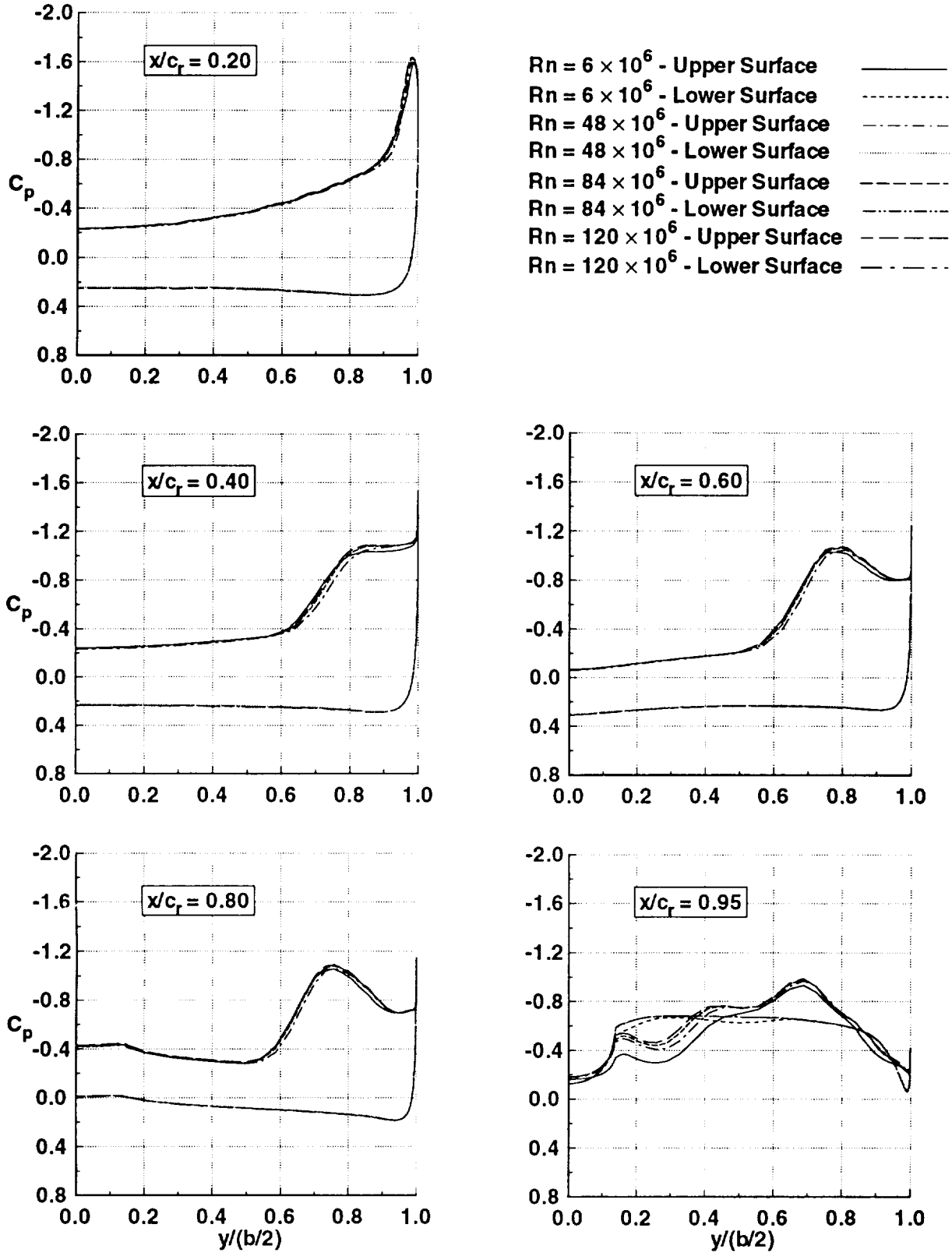

Figure 22.d. Predicted Reynolds number effect on pressure coefficients, medium leading-edge radius, $M_\infty = 0.85$, $\alpha = 12^\circ$, CFL3D, Spalart-Allmaras turbulence model.

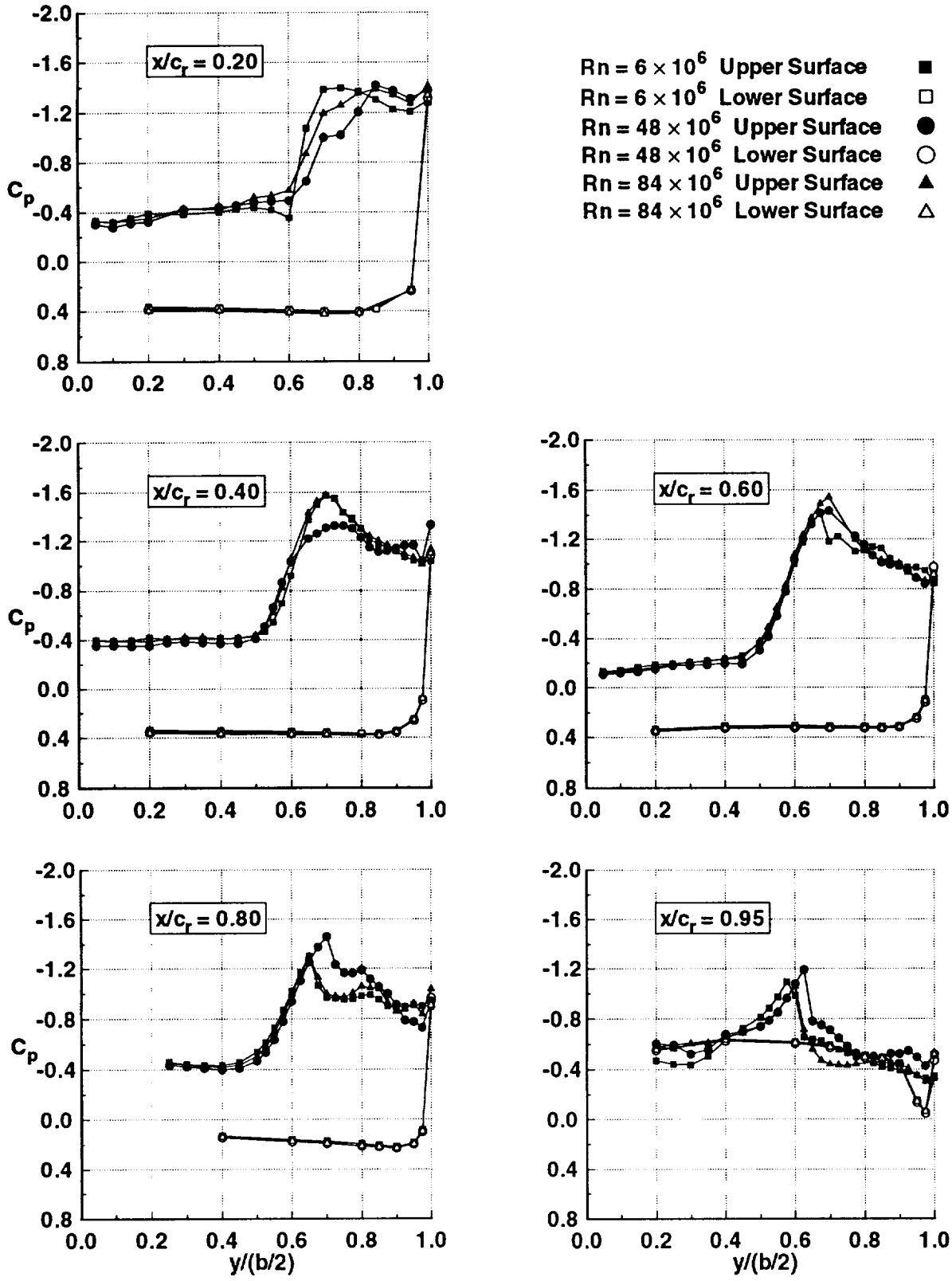

Figure 22.e. Reynolds number effect on pressure coefficients, medium leading-edge radius, $M_\infty = 0.85$, $\alpha = 16^\circ$, experiment.

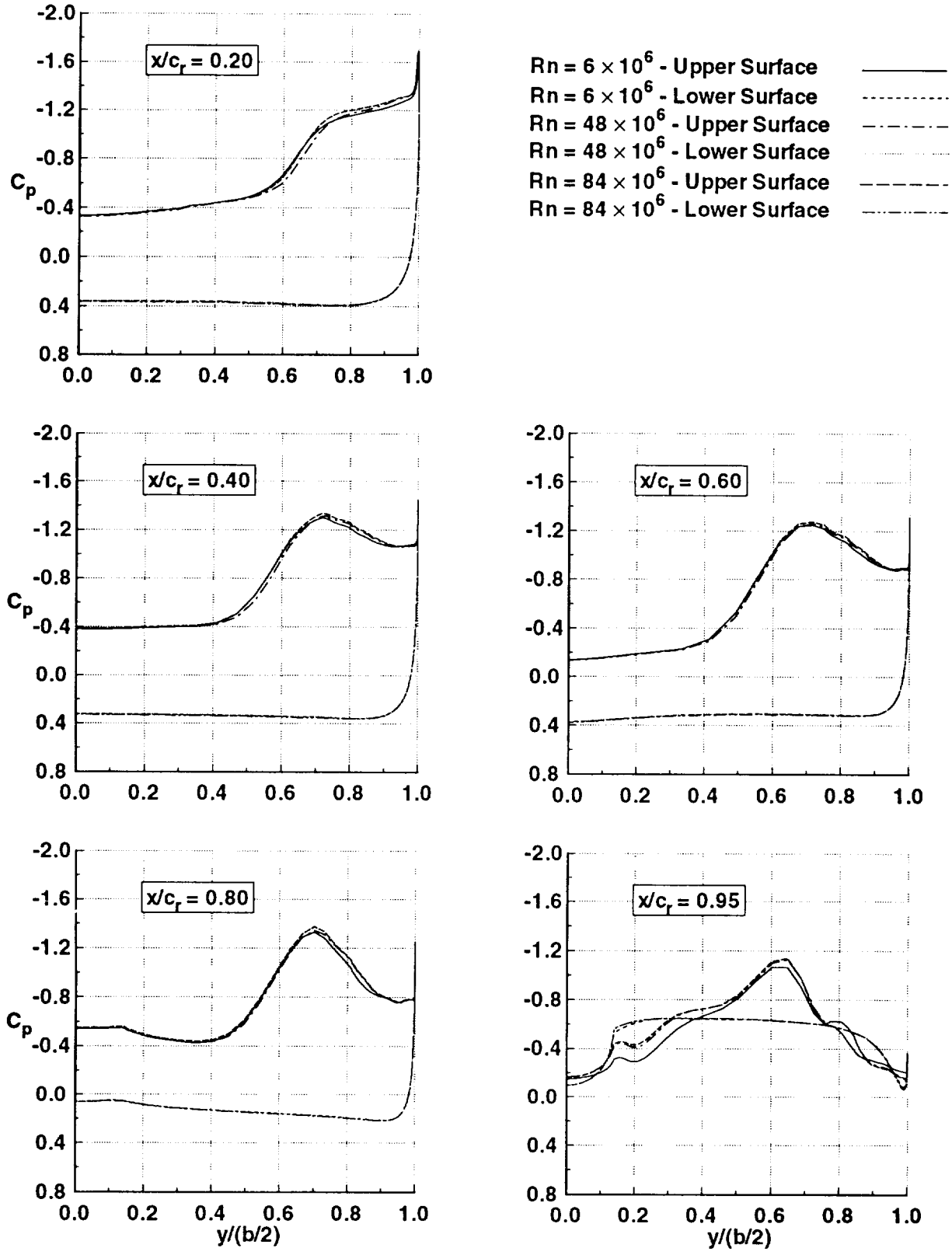

Figure 22.f. Predicted Reynolds number effect on pressure coefficients, medium leading-edge radius, $M_\infty = 0.85$, $\alpha = 16^\circ$, CFL3D, Spalart-Allmaras turbulence model.

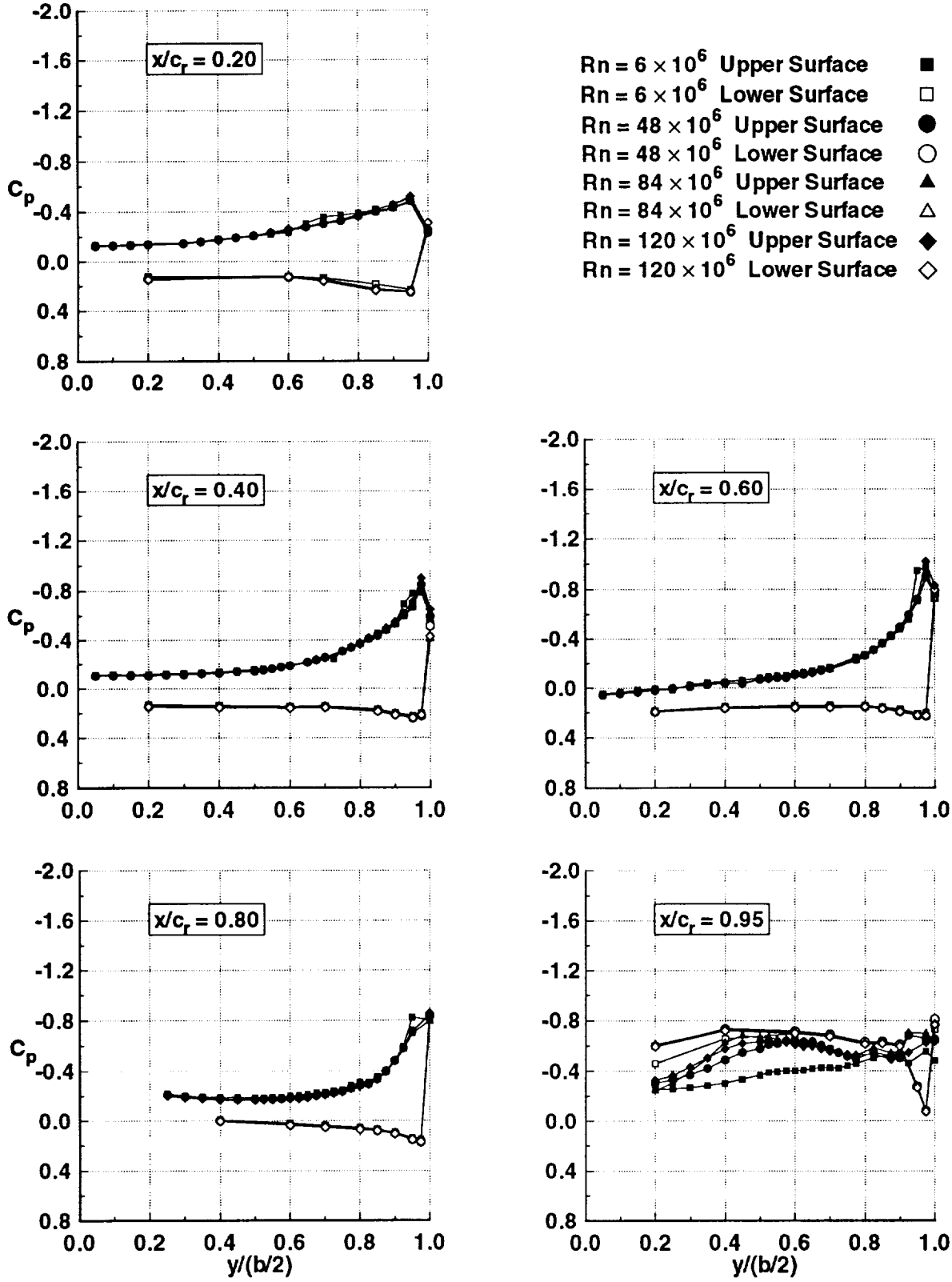

Figure 23.a. Reynolds number effect on pressure coefficients,round leading-edge radius, $M_\infty = 0.85$, $\alpha = 7^\circ$, experiment.

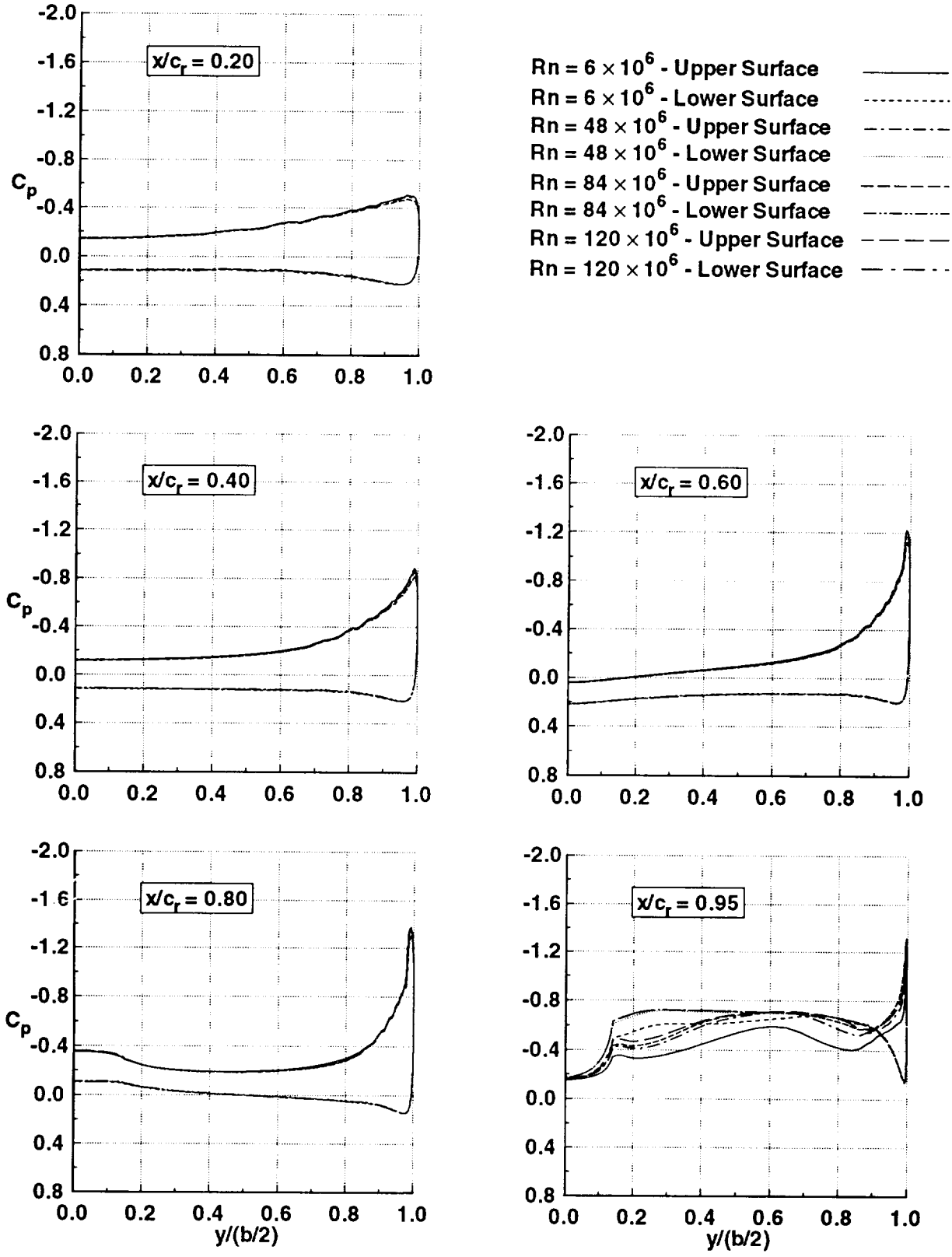

Figure 23.b. Predicted Reynolds number effect on pressure coefficients, round leading-edge radius, $M_\infty = 0.85$, $\alpha = 7^\circ$, CFL3D, Spalart-Allmaras turbulence model.

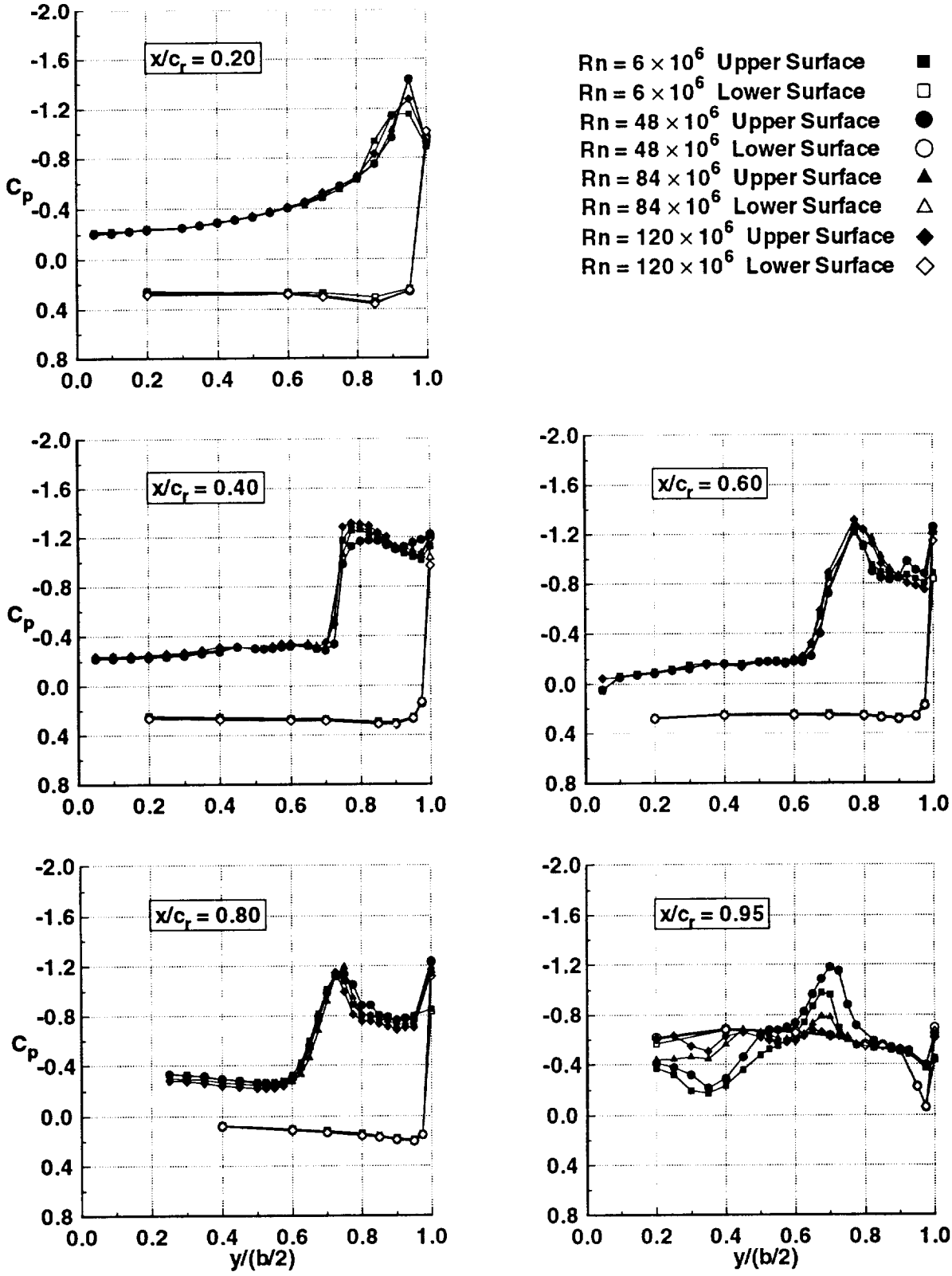

Figure 23.c. Reynolds number effect on pressure coefficients, round leading-edge radius, $M_\infty = 0.85$, $\alpha = 12^\circ$, experiment.

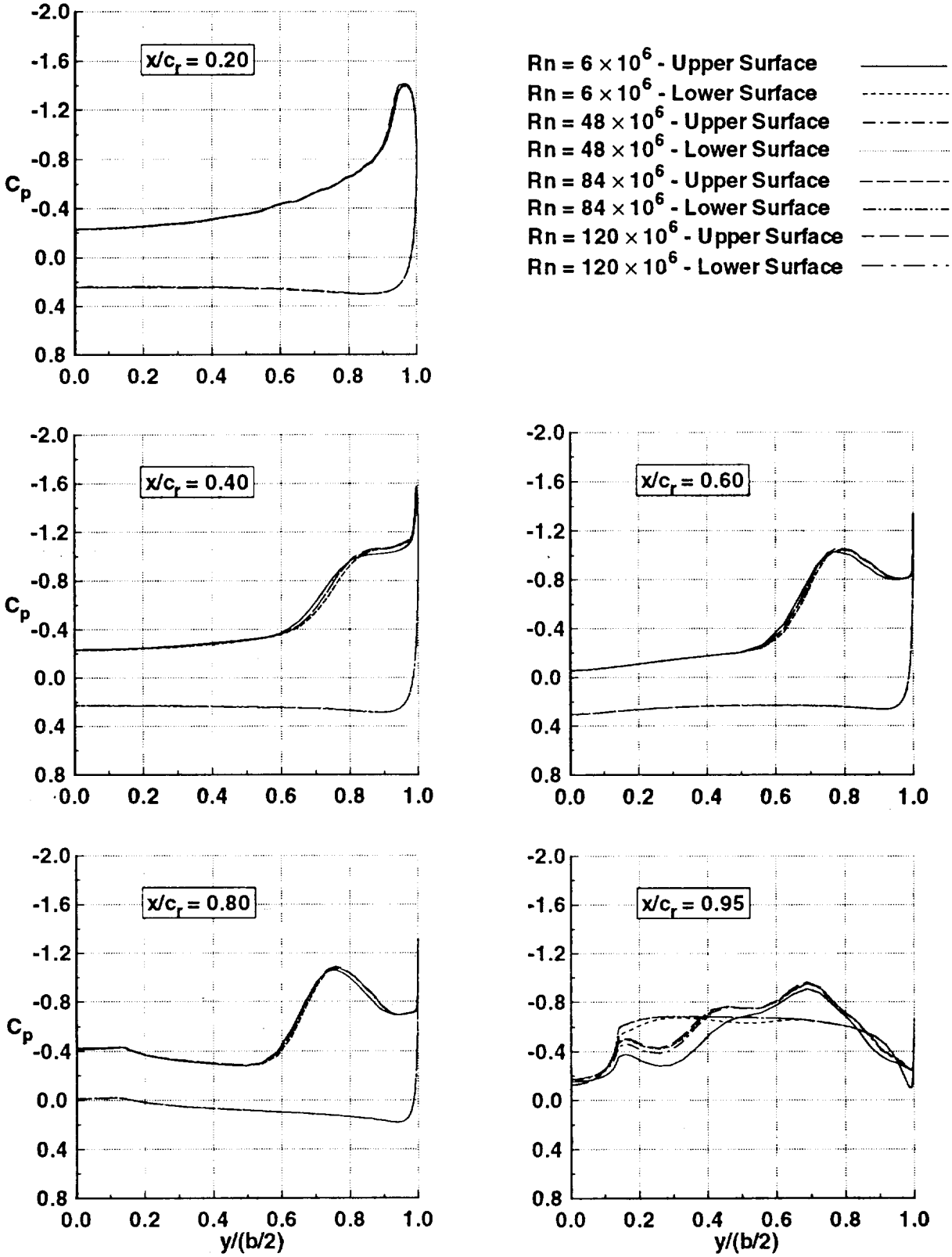

Figure 23.d. Predicted Reynolds number effect on pressure coefficients, round leading-edge radius, $M_\infty = 0.85$, $\alpha = 12^\circ$, CFL3D, Spalart-Allmaras turbulence model.

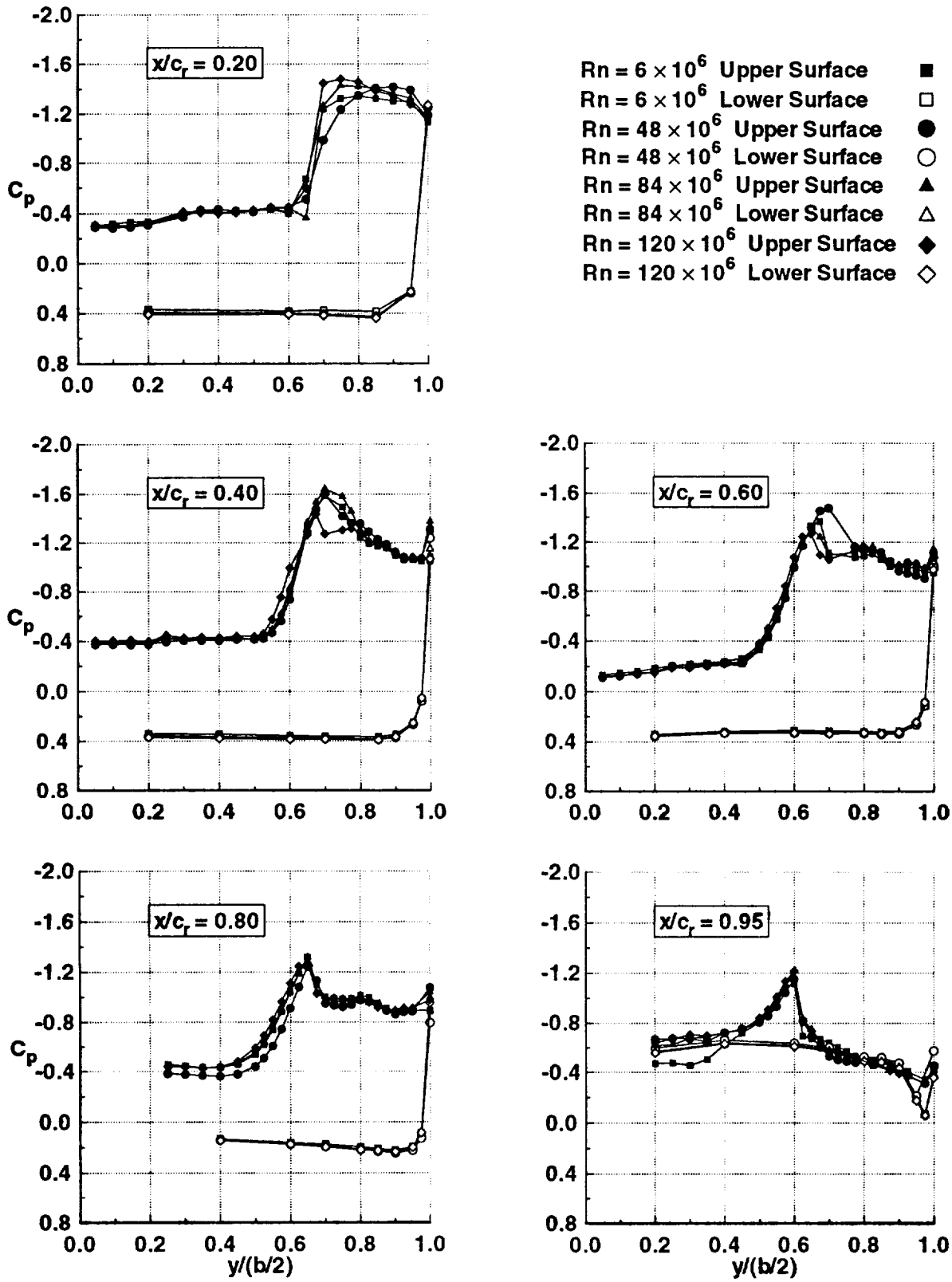

Figure 23.e. Reynolds number effect on pressure coefficients, round leading-edge radius, $M_\infty = 0.85$, $\alpha = 16^\circ$, experiment.

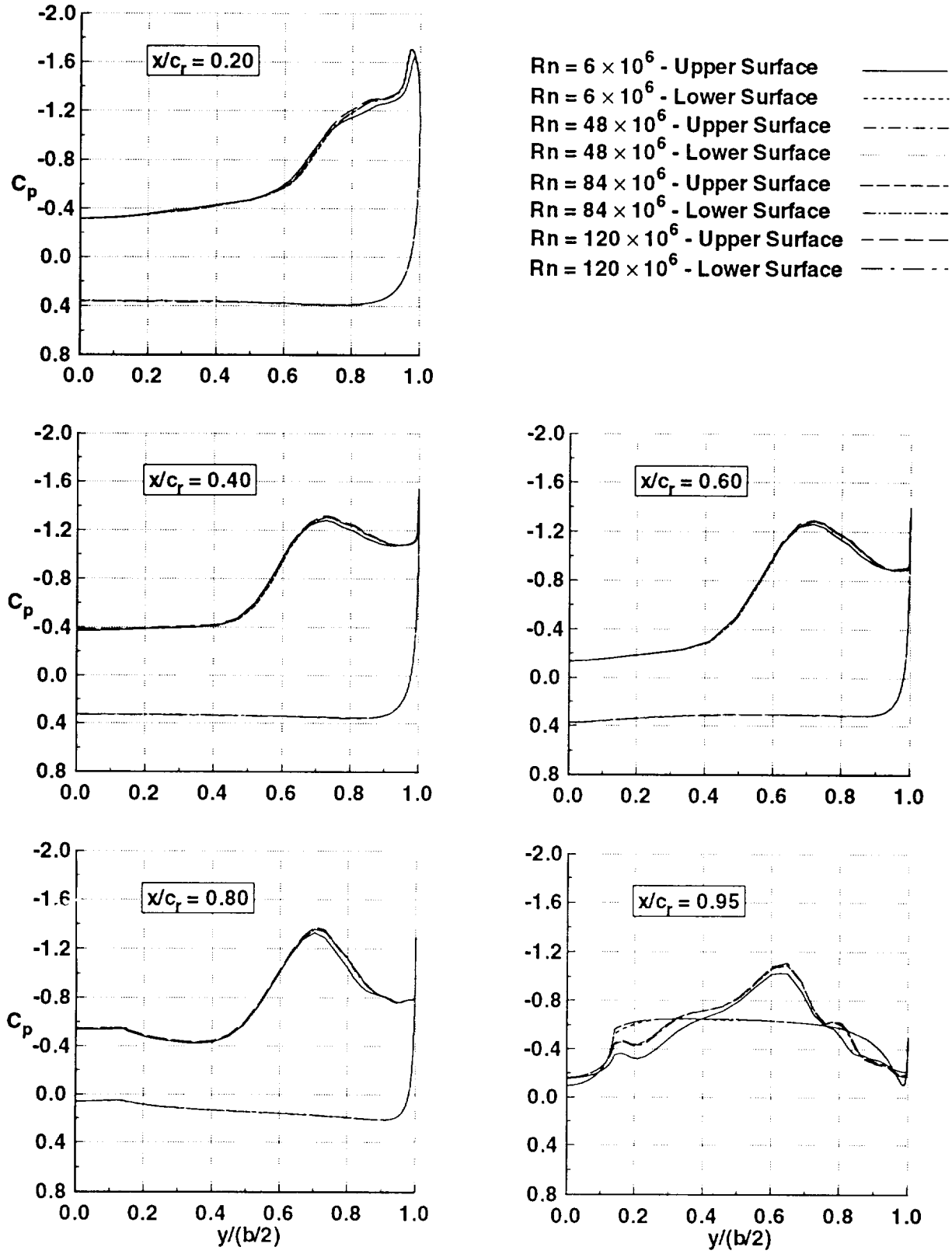

Figure 23.f. Predicted Reynolds number effect on pressure coefficients, round leading-edge radius, $M_\infty = 0.85$, $\alpha = 16^\circ$, CFL3D, Spalart-Allmaras turbulence model.

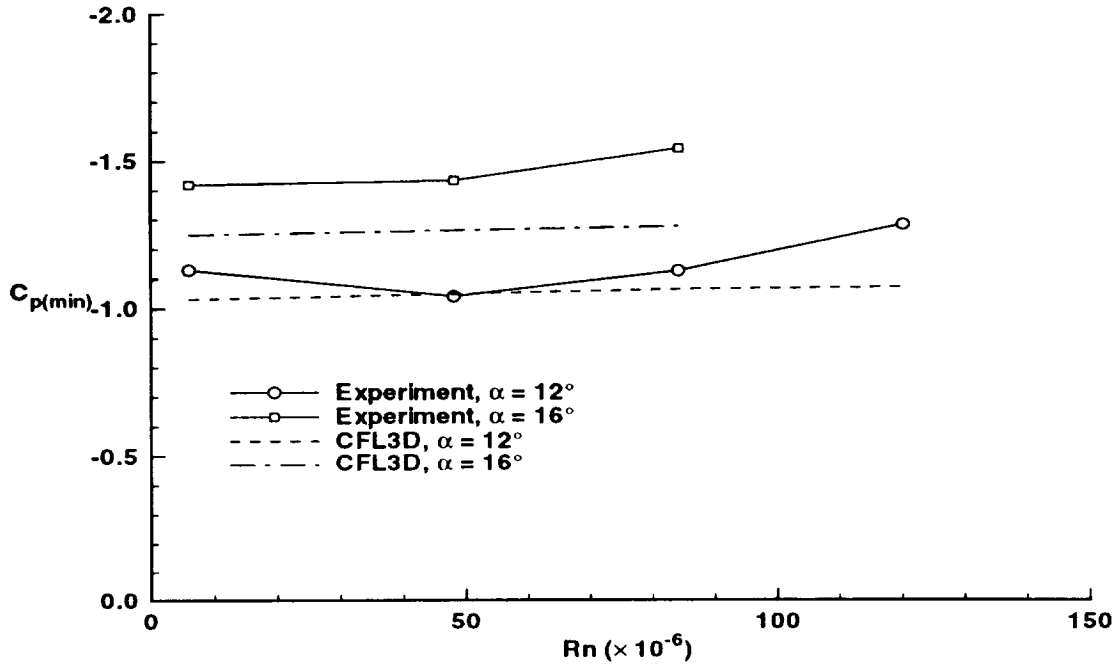

Figure 24. Reynolds Number effect on minimum suction pressure for medium leading-edge radius geometry, $M_\infty = 0.85$, $x/c_r = 0.60$.

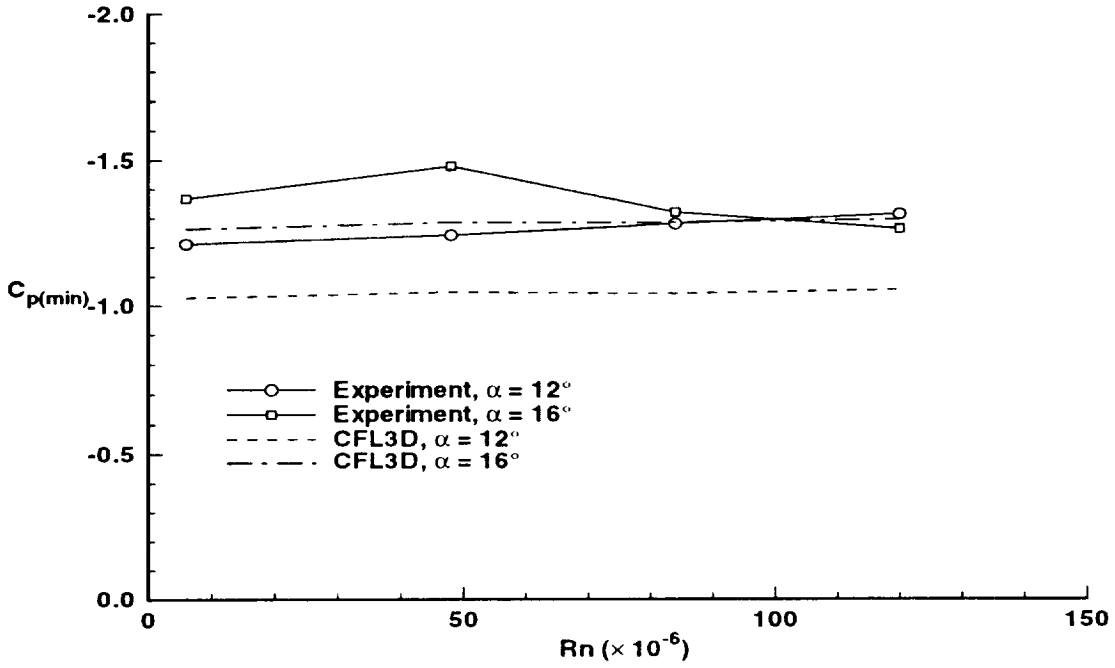

Figure 25. Reynolds Number effect on minimum suction pressure for the round leading-edge radius geometry, $M_\infty = 0.85$, $x/c_r = 0.60$.

Block	Original Grid			Refined Grid		
	i_{max}	j_{max}	k_{max}	i_{max}	j_{max}	k_{max}
1	49	13	65	49	13	65
2	49	49	65	49	73	65
3	49	13	65	33	13	65
4	49	65	65	49	65	65
5	25	49	65	25	49	65
6	49	33	65	49	33	65
7	49	25	65	49	25	65
8	49	25	65	33	25	65
9	49	33	65	33	33	65

Table 1: Computational grid dimensions.

Leading-Edge Radius	Reynolds Number ($x10^{-6}$)	angle-of-attack	y^+_{max}	y^+_{avg}	Standard Deviation
Medium	6	7.15°	1.60	0.27	0.12
Medium	6	12.3°	1.60	0.29	0.17
Medium	6	16.37°	1.60	0.29	0.17
Medium	48	6.80°	7.90	1.93	0.92
Medium	48	12.03°	8.02	1.95	0.98
Medium	48	16.25°	7.76	1.92	0.92
Medium	84	6.99°	6.57	2.98	1.01
Medium	84	12.03°	6.63	2.98	1.03
Medium	84	16.25°	7.85	3.07	1.17
Medium	120	7.03°	10.70	4.18	1.52
Medium	120	12.44°	10.66	4.19	1.58
Medium	120	14.63°	10.55	4.19	1.55
Round	6	7.14°	2.72	0.27	0.13
Round	6	12.28°	2.53	0.27	0.13
Round	6	16.37°	2.43	0.27	0.13
Round	48	6.98°	7.08	1.79	0.59
Round	48	12.24°	6.66	1.79	0.62
Round	48	16.44°	6.77	1.78	0.61
Round	84	6.78°	10.51	3.00	0.94
Round	84	12.09°	10.45	2.98	0.99
Round	84	16.38°	10.65	2.96	0.97
Round	120	7.03°	13.64	4.09	1.24
Round	120	12.29°	13.61	4.06	1.30
Round	120	16.59°	13.82	4.04	1.28

Table 2: Y-Plus values for computational solutions using the Spalart-Allmaras turbulence model

Leading-Edge Radius	Reynolds Number ($x10^{-6}$)	α_w	α_{core} (ref. 32)	α_{core} (CFL3D)	Λ_{core} (ref. 32)	Λ_{core} (CFL3D)
Medium	6	12.3°	4.07°	3.96°	73.8°	73.81°
Medium	6	16.37°	5.09°	5.10°	73.8°	72.61°
Medium	48	12.03°	4.01°	4.23°	73.8°	74.02°
Medium	48	16.25°	5.06°	5.10°	73.8°	72.60°
Medium	84	12.03°	4.01°	3.96°	73.8°	73.00°
Medium	84	16.25°	5.06°	5.10°	73.8°	72.60°
Medium	120	12.44°	4.11°	3.77°	73.8°	73.12°
Medium	120	14.63°	4.66°	3.90°	73.8°	72.87°
Round	6	12.28°	4.07°	4.05°	73.8°	73.41°
Round	6	16.37°	5.09°	5.00°	73.8°	73.11°
Round	48	12.24°	4.06°	4.42°	73.8°	74.43°
Round	48	16.44°	5.11°	5.00°	73.8°	73.11°
Round	84	12.09°	4.02°	3.30°	73.8°	73.80°
Round	84	16.38°	5.09°	5.00°	73.8°	73.11°
Round	120	12.29°	4.07°	3.17°	73.8°	73.90°
Round	120	16.59°	5.15°	5.00°	73.8°	73.11°

$$\alpha_{core} = \alpha_w - ((0.1 + 0.01 \times \Lambda_{LE}) \alpha_w - 1.0) \text{ , deg.}$$ (Equation 3 from Reference 32)

$$\Lambda_{core} = 33.5 + 0.62\Lambda_{LE} \text{ , deg.}$$ (Equation 2 from Reference 32)

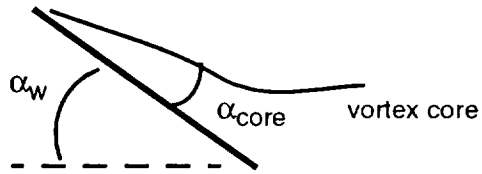

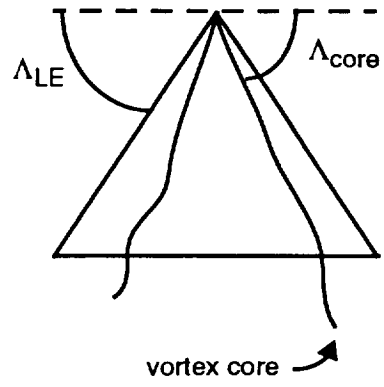

Table 3: Predicted vortex core trace compares well with experiment.

REPORT DOCUMENTATION PAGE

Form Approved
OMB No. 0704-0188

1. AGENCY USE ONLY (*Leave blank*)	2. REPORT DATE	3. REPORT TYPE AND DATES COVERED
	November 1994	Contractor Report

4. TITLE AND SUBTITLE
Transonic Navier-Stokes Calculations About a 65° Delta Wing

5. FUNDING NUMBERS
C NAS1-18585
WU 505-59-54-01

6. AUTHOR(S)
W. Kelly Londenberg

7. PERFORMING ORGANIZATION NAME(S) AND ADDRESS(ES)
ViGYAN, Inc.
30 Research Drive
Hampton, VA 23666

8. PERFORMING ORGANIZATION REPORT NUMBER

9. SPONSORING / MONITORING AGENCY NAME(S) AND ADDRESS(ES)
National Aeronautics and Space Administration
Langley Research Center
Hampton, VA 23681-0001

10. SPONSORING / MONITORING AGENCY REPORT NUMBER
NASA CR-4635

11. SUPPLEMENTARY NOTES
Langley Technical Monitor: Lawrence E. Putnam
Final Report

12a. DISTRIBUTION / AVAILABILITY STATEMENT
Unclassified - Unlimited

Subject Category 02

12b. DISTRIBUTION CODE

13. ABSTRACT (*Maximum 200 words*)

A computational study has been conducted in which the CFL3D Navier-Stokes solver coupled with an algebraic and an one-equation nonequilibrium turbulence model has been used to predict the flow over a 65° delta wing at transonic conditions for Reynolds numbers ranging from 6 x 10^6 to 120 x 10^6 based on mean aerodynamic chord. Solutions obtained indicated that the computational method when used with the one-equation turbulence model predicts results that compare well with experiment for attached flow conditions. Comparisons with experimental pressure at separated conditions show that the computational method, even though primary flow-field features are predicted well, does not predict secondary flow features.

14. SUBJECT TERMS
vortex flow
delta wing
computational fluid dynamics
Navier-Stokes
transonic flow
turbulence models
Reynolds number

15. NUMBER OF PAGES
72

16. PRICE CODE
A04

17. SECURITY CLASSIFICATION OF REPORT	18. SECURITY CLASSIFICATION OF THIS PAGE	19. SECURITY CLASSIFICATION OF ABSTRACT	20. LIMITATION OF ABSTRACT
Unclassified	Unclassified	Unclassified	

National Aeronautics and
Space Administration
Langley Research Center
Mail Code 180
Hampton, VA 23681-00001